# ELECTRON-BEAM-PUMPED

# RARE GAS HALIDE LASERS

by

Claude David Philip Levy, BSc, ARCS

*A thesis submitted in partial fulfilment of the requirements for the degree of Doctor of Philosophy of the University of London and for the Diploma of Imperial College*

August 1980

Blackett Laboratory
Imperial College
London, England

To Frances

ABSTRACT

Electron-beam pumping of excimer lasers is reviewed, as well as the kinetics of the rare gas halides, with particular emphasis on KrF, which is well understood.

The design and construction of electron-beam-pumped KrF and XeCl lasers are described. Laser action was observed at 248 nm and 308 nm respectively. Maximum laser energy, using a co-axial diode, was 1.35 J in a 20 ns (FWHM) XeCl laser pulse, with corresponding peak power of 6 MW $cm^{-2}$ and specific laser energy storage density of 8 J $litre^{-1}$ in the active medium. Maximum energy from a smaller diameter KrF laser was 0.59 J in a 10 ns (FWHM) pulse, corresponding to a peak power of 26 MW $cm^{-2}$ and an energy storage density of 17 J $litre^{-1}$. In both cases, intrinsic laser efficiency was $\sim$ 2%.

A novel type of co-axial e-beam diode was designed and constructed, in which pumping power is not restricted by magnetic self-pinching of the electron-beam. The e-beam characteristics were 500 kV, 36 kA peak voltage and current, pulse duration 30 ns (FWHM).

The ground state dissociation of XeCl was investigated using the frequency-doubled, mode-locked output from a tunable flashlamp-pumped Rhodamine 6G dye laser to probe the XeCl gas mixture after e-beam pumping had ceased. The ground state lifetime of XeCl under typical conditions (96.8% Ne, 3% Xe, 0.2% HCl at 5 bar) was measured to be 19 ($\pm$ 3) ns, and the two body collisional dissociation rate of the XeCl ground state and Xe was $k_{Xe} = 4\ (\pm 3) \times 10^{-12}\ cm^3\ s^{-1}$.

Small signal gain during e-beam excitation was found to reach a maximum of 0.28 $cm^{-1}$ in XeCl.

ACKNOWLEDGEMENTS

I wish to thank Prof D.J. Bradley for his guidance and support, and Dr M.H.R. Hutchinson for many helpful discussions. I would also like to thank Dr J.R. Taylor and Dr P.W. Smith for their advice and encouragement.

I am indebted to Dr K. Sala for his assistance, and in particular to Miss Grace Reksten, my co-worker during the XeCl dissociation experiments, who was responsible for the dye laser and whose determination and optimism never wavered, even at three in the morning.

I am grateful to Mr P.H. Dickinson for help with the fluorine handling, and for ensuring the safety of the procedure.

Thanks are also due to Messrs B. Weekley, R.S. Morrison, C. Cooper, J. Bean and J. Clark for their technical assistance, and to Mr N. Jackson and Miss Louise Symmonds for photographic work. I would like to thank Dr W. Sleat for help with the electronics, and Dr M.J. Lee who supplied the aluminium mirror.

Finally, I am very grateful to Frances Mawer for her moral support and patience over the last three years, and for the great care with which she has typed this thesis.

The author was supported by a bursary provided by Barr & Stroud Ltd., Glasgow, and by a research assistantship from the SRC.

TABLE OF CONTENTS



cont/

TABLE OF CONTENTS (cont) Page number



cont/

TABLE OF CONTENTS (cont) Page number

CHAPTER 1

## INTRODUCTION

The rare gas monohalide gas lasers are efficient sources of high power ultra-violet radiation, and are a type of excimer or exciplex laser which has received a great deal of attention in recent years.

A diatomic excimer is defined[1] as a homonuclear dimer which is bound in an excited state and unbound or dissociative in the ground state. An exciplex is a heteronuclear complex which is bound in the excited state and unbound in the ground state, and is the correct chemical term for the rare gas halides such as KrF or ArF. However, the term excimer, strictly applied only to molecules such as $Xe_2$ or $Hg_2$, is now commonly used to describe any molecular laser having a dissociative ground state.

Fig. 1.1 is a schematic potential energy diagram for a typical excimer or exciplex. It was first pointed out by Houtermans[2] that the bound-free transition, between the excited state and ground state of rare gas or group IIb metal excimers, provided the basis for laser action in the vacuum ultra-violet, via the process

$$(AB)^* \rightarrow \begin{array}{l} AB + h\upsilon \\ \downarrow \\ A + B \end{array}$$

where A and B are two atoms, and * denotes an excited state. A population inversion on such a transition is very easily obtained, since the ground state molecules dissociate in $\sim 10^{-13}$ sec as their potential energy is converted entirely into kinetic energy, and removal of the lower laser level population is very rapid. Quantum efficiency is high,

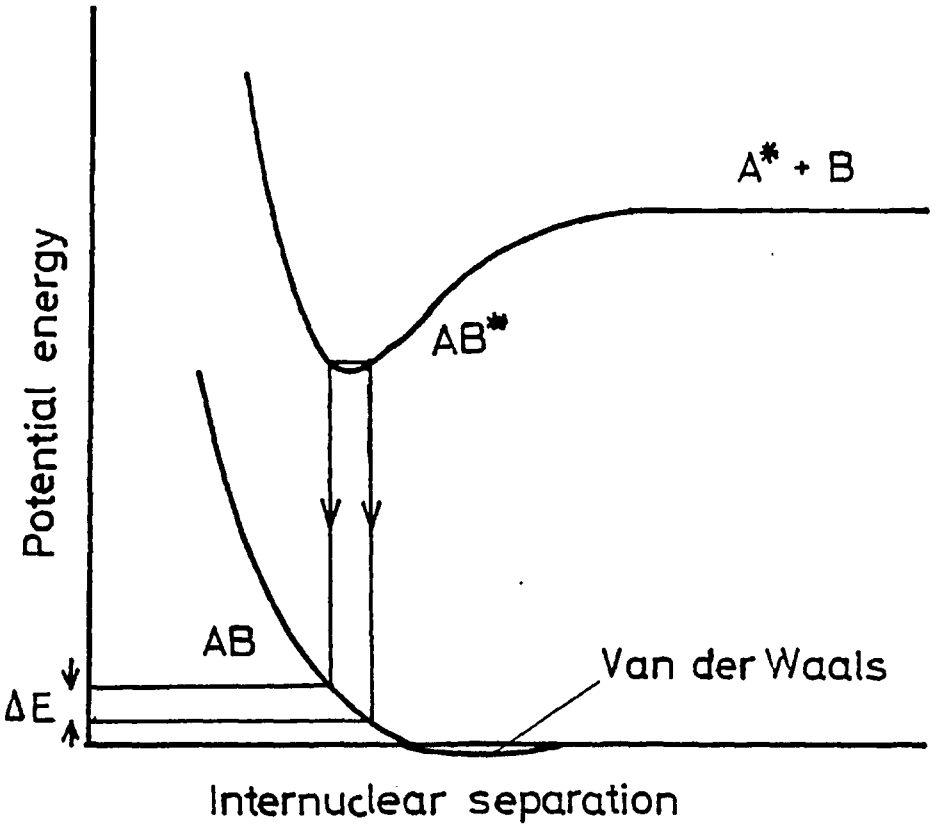


FIGURE 1.1 Schematic potential energy diagram of typical excimer or exciplex

because the transition terminates on the ground state potential. The inversion is very nearly equal to the upper laser level population. An ideal excimer or exciplex emits a true continuum, rather broad ($\Delta\lambda$ = 10-20 nm) in the rare gases due to the steeply repulsive ground state, less so ($\Delta\lambda \sim 2$ nm) in the rare gas halide systems which terminate on a rather flat ground state potential. The rare gas halides XeF and XeCl have slightly bound ground states which are dissociative at room temperature, and display ordinary bound-bound emission spectra showing vibrational structure.

At the time (1960) of Houtermans' suggestion, it was not possible to build an excimer laser, due to the very high threshold inversion. This is of the order

$$\Delta N \sim \frac{8\pi\Delta\lambda}{\lambda^4} \qquad 1.1$$

where $\Delta\lambda$ is the fluorescence bandwidth of the transition, centred at wavelength $\lambda$. For the rare gas excimers, the threshold inversion is $\sim 10^{15}$ $cm^{-3}$, which is much higher than was then attainable. The upper state lifetime of order 10 ns implies a threshold pump rate of $\sim 10^6$ watts $cm^{-3}$.

The first excimer laser, reported by Basov[3], was made possible by the development of relativistic gigawatt electron-beam (e-beam) generators. Basov used such a high intensity e-beam to pump liquid xenon. Soon after this, lasing was reported from e-beam-pumped, high pressure, gas phase xenon ($\lambda$ = 172 nm)[4], krypton ($\lambda$ = 146 nm)[5] and argon ($\lambda$ = 126 nm)[6].

The development of the rare gas halides as laser systems was spurred by the work of Golde and Thrush[7] and Velazco and Setser[8], who observed excimer emission from rare gas halides and oxides while studying the quenching of excited states of atomic argon and xenon by halogen and oxygen donors. The first rare gas halide laser, reported by Searles and Hart[9], operated at 282 nm in the XeBr molecule. Since then, laser oscillation or fluorescence has been observed from a total of ten rare gas halides, at wavelengths ranging from 108 nm for NeF to 353 nm from XeF[9-17]. Table 1.1 lists the rare gas halides in matrix form, indicating which have shown laser action or fluorescence, and their wavelengths.

The rare gas halides are easier to pump than the rare gas excimers, because their narrower bandwidths, longer wavelengths and similar lifetimes result in a larger stimulated emission cross-section ($\sigma_s$ RARE GAS EXCIMER $\sim 10^{-17}$ $cm^2$, $\sigma_s$ RARE GAS HALIDE $\sim 10^{-16}$ $cm^2$). Laser action in the rare gas halides was initially achieved with intense e-beam pumping

TABLE 1.1

| | Ne | Ar | Kr | Xe |
|---|---|---|---|---|
| F | 108(P) | 193 | 248 | 351 |
| Cl | Ionic state | 175(P) | 222(P) | 308 |
| Br | not | (P) | 206(P) | 282(P) |
| I | lowest | state | (P) | 253(P) |

Wavelength (nm) of observed B-X emission from rare gas monohalides. Underlined values indicate laser action observed, (P) indicates predissociation.

of gas mixtures, but since then discharge-pumped systems have lased in the same molecules. Discharge pumping offers the advantage of less complexity and higher repetition rates, but is difficult to scale up in energy due to problems of discharge stability and circuit inductance. E-beams remain the most efficient way to pump large volume, high pressure, high energy systems. The largest pulse energy reported to date is $\sim$ 350 J from e-beam-pumped (600 ns, 40 kA, 7 kJ) KrF[18], compared with $\sim$ 50 J in 300 ns from an e-beam stabilized discharge-pumped system[18]. The highest reported intrinsic efficiency (= laser energy ÷ energy deposited in gas) of 15% was also obtained from e-beam-pumped KrF[19], in a 120 ns pulse.

The great amount of interest in the rare gas halide lasers is due to their high efficiency ($\sim$ 1% overall) and inherent high power in the ultra-violet, which may make possible applications in laser fusion or isotope separation.

In this thesis the design and performance of transverse and co-axial e-beam-pumped, short pulse ($\sim$ 20 ns) high power KrF and XeCl lasers are described. The operation of a novel co-axial e-beam diode, scalable to very high current densities, is also described.

The ground state of XeCl is slightly bound and therefore has a finite dissociation time, which reduces the population inversion. The lifetime of the ground state in a typical laser mixture was measured, in order to assess the importance of ground state bottlenecking in the XeCl laser.

CHAPTER 2

# ELECTRON-BEAM PUMPING OF GAS LASERS

## 2.1 Introduction

Relativistic intense electron-beams provide a convenient pumping source for the rare gas halides, as noted earlier.

A typical laser mixture consists of a buffer gas, another rare gas, and a halogen donor, at a total pressure of several bar. High energy (0.2 - 2 MeV) electrons injected into the gas partly ionize the laser medium, and recombination processes lead either directly or indirectly (through excited state kinetics) to excitation of the upper laser level.

Most e-beam generators consist of an H.T. (10 - 100 kV) D.C. supply, an energy storage bank, a voltage gain device, a pulse forming line, and a vacuum diode which forms the e-beam and injects it into the laser cell. Fig. 2.1 is a block diagram of a typical e-beam generator. The e-beam generator described in this thesis is a Physics International Pulserad 110A (500 keV, 35 kA, 30 ns). The present generation of 100-kiloampere, megawatt range machines has its origins in work done in the early 1960's by J.C. Martin and co-workers at the AWRE at Aldermaston.

In this chapter the mechanism of energy deposition in gas lasers is described, as well as the design and characteristics of e-beam diodes. The detailed operation of the Pulserad 110A, which depends on a Marx generator for energy storage and voltage gain, is also described. Information on the particular e-beam diodes used is left for later, where it is incorporated with a description of the lasers.

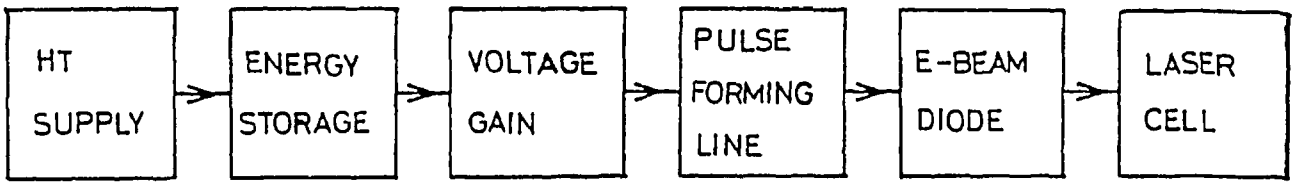


FIGURE 2.1 Block diagram of e-beam generator.

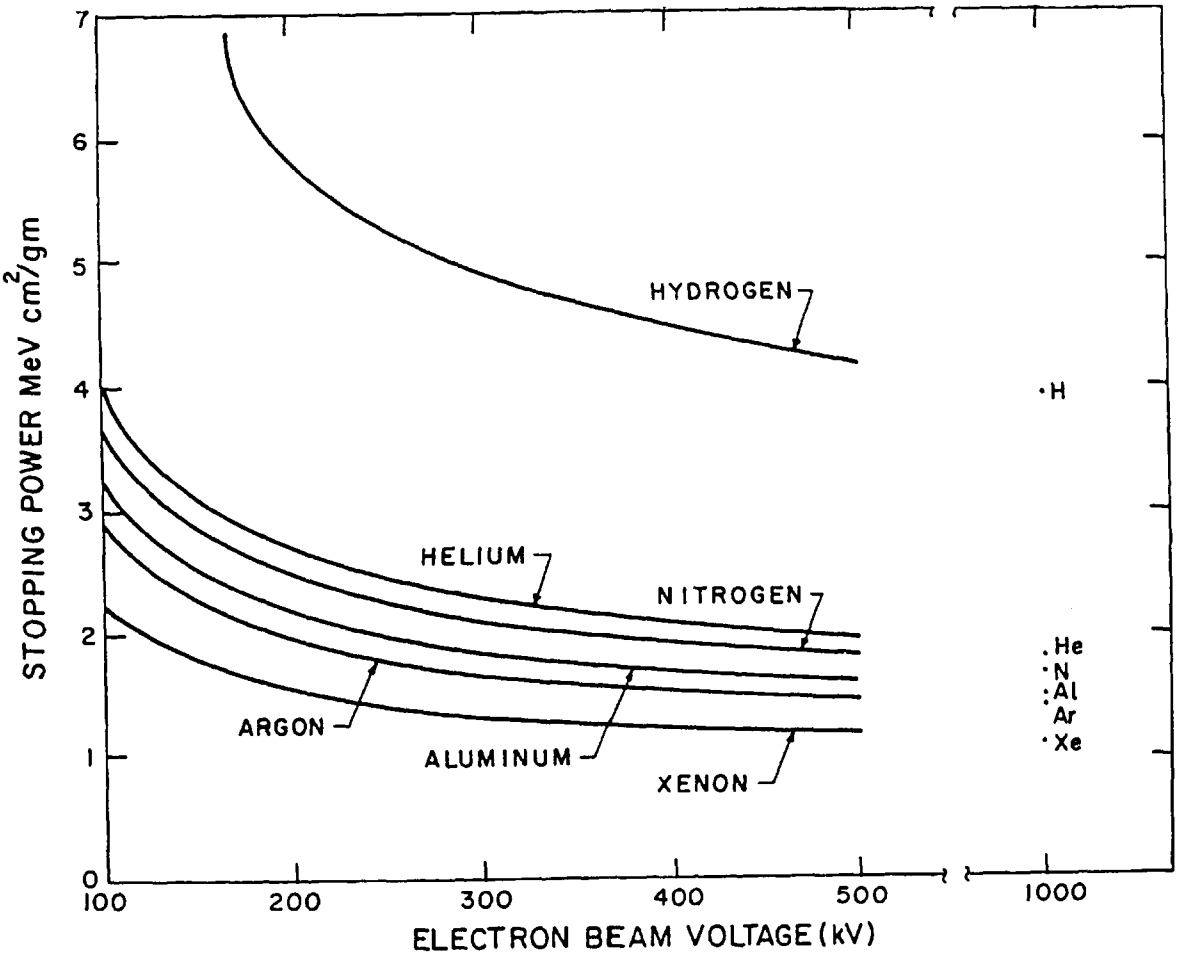


FIGURE 2.2 E-beam stopping power versus electron energy.

## 2.2 E-Beam Energy Deposition in Gases

Ionization in an e-beam-pumped gas medium is a consequence of collisions between high energy primary electrons $e_p$ and an atom or molecule. For example, in argon we have

$$Ar + e_p \rightarrow Ar^+ + e_p + e_s$$

where $e_s$ is a secondary electron. As a primary electron traverses the gas, it continually slows down and scatters off atoms and molecules, giving up energy to the medium. Ionization creates fast secondary electrons with a broad energy spectrum, which further ionize the gas as they slow down. Both secondary and primary electrons will also excite electronically atoms and molecules.

### 2.2.1 Stopping power and range

As the e-beam traverses the gas medium, it loses energy at a rate P (watts $cm^{-3}$) proportional to the e-beam current density j (amps $cm^{-2}$) and the stopping power dE/dx (volts $cm^{-1}$) of the medium

$$P = j\, dE/dx \qquad 2.1$$

The formula for the stopping power normalized to mass density $\rho$, based on the Bethe stopping power theory, is given by[20]

$$-\frac{1}{\rho}\frac{dE}{dx} = \text{const.} \times \frac{1}{\beta^2}\frac{Z}{A}\left\{\log_e \frac{T^2(T+2)}{2(I/E_o)^2} - f(\beta)\right\} \text{ MeV cm}^2 \text{ gm}^{-1} \qquad 2.2$$

where $\beta$ = velocity/c

$$T = \frac{\text{kinetic energy (MeV)}}{T_o} \qquad \text{electron}$$

$T_o$ = rest mass = 0.51 MeV

Z = atomic number

A = atomic weight medium

I = mean excitation energy (MeV)

$f(\beta)$ = relativistic term of order unity

Daugherty[21] has plotted the e-beam stopping powers of several elements, reproduced in Fig. 2.2, using tables prepared by Berger and Seltzer[20]. The normalized stopping power varies only slightly between species (except hydrogen) due to the slow variation of Z/A and the logarithmic dependence on I. It is fairly constant above 0.2 MeV, so that an electron of higher energy ionizes the medium at a uniform average rate, until the electron slows below 0.2 MeV, below which point the stopping power and rate of ionization increases.

The range of an electron in a gas without externally applied electric or magnetic fields can be estimated by use of the continuous slowing down approximation (c.s.d.a.). The c.s.d.a. range is defined[20] as

$$R(E) = -\int_0^E \frac{dE}{dE/dx} \qquad 2.3$$

and is the pathlength of an electron of initial kinetic energy E which slows to zero energy in the medium. It should be noted that R(E) does not refer to the penetration depth of an electron into the medium. Because of scattering by atoms the electron experiences many changes of direction, and as a result the macroscopic penetration depth of an e-beam will be less than R(E) by a factor of $\sim$ 2-3[22,120].

### 2.2.2 Distribution of energy in e-beam-pumped gases

The distribution of energy between ions, excited states, and electrons with insufficient energy to produce electronic excitation can be estimated by consideration of the energy balance equation for a primary

electron of initial energy E[23],

$$E = N_i\bar{E}_i + N_{ex}\bar{E}_{ex} + N_i\bar{E}_e \qquad 2.4$$

where $N_i$ and $N_{ex}$ are the numbers of singly charged ions and excited atoms produced in the medium, respectively, with average energy expenditure $\bar{E}_i$ and $\bar{E}_{ex}$. $\bar{E}_e$ is the average energy of the remaining sub-excitation energy electrons. The mean energy loss per ion-electron pair formed

$$W = E/N_i \qquad 2.5$$

is related to $\bar{E}_i$, $\bar{E}_{ex}$ and $\bar{E}_e$ by the relation

$$\frac{W}{I} = \frac{\bar{E}_i}{I} + \frac{N_{ex}}{N_i}\frac{\bar{E}_{ex}}{I} + \frac{\bar{E}_e}{I} \qquad 2.6$$

where I is the ionization potential. (W/I) has been measured for all the rare gases, and is approximately constant at 1.7 to 1.8.

In the case of helium, all the values in the energy balance equation 2.6 have been experimentally determined, and both sides of the equation agree to within 1%. Evidence for the other rare gases is incomplete, but because of their structural similarity, corresponding numbers will be approximately the same. $\bar{E}_i/I$ exceeds unity due to the possibility of ionization of an inner shell electron[24] or multiple ionization. $\bar{E}_{ex}/I$ can be estimated successfully, because in the rare gases all the excited states lie close to the ionization limit, within $\sim$ 4eV. $N_{ex}/N_i$ is estimated by taking the corresponding ratio of collisional cross-sections averaged over the energy distribution of the electrons. $\bar{E}_e/I$ is the mean energy per ion pair left in sub-excitation electrons, and in a pure rare gas is dissipated as heat. Values pertinent to argon are: W/I = 1.68, $\bar{E}_i/I$= 1.1, $N_{ex}/N_i \sim 0.4$, $\bar{E}_{ex}/I \sim 0.8$[23,24]. This implies that $\bar{E}_e$ = 4.1 eV,

from equation 2.6. Therefore according to equation 2.4, of the total energy absorbed by e-beam-pumped pure argon, 65% goes to ionization, 19% to excitation, and 16% to heating of the gas. Similar values are obtained for the other rare gases, e.g. 62% : 20% : 18% respectively for helium. In a rare gas halide laser, most of the energy will be absorbed by the majority buffer gas.

Both ions and excited atoms are precursors to excimer formation, so a useful number is the average energy W* required to form either an ion-electron pair or an excited atom, where

$$W^* = E/(N_i + N_{ex}) \qquad 2.7$$

For argon, W* = 20 ev/precursor. If it is assumed that every argon ion or excited state produced in an Ar-diluent KrF laser leads to a KrF laser photon ($h\upsilon$ = 5.0 ev), the maximum possible intrinsic efficiency in an e-beam-pumped system is

$$h\upsilon/W^* = 25\% \qquad 2.8$$

The quantum efficiency is

$$\eta_Q = h\upsilon/E^* \qquad 2.9$$

where E* is the energy of the lowest energy precursor. In the case of KrF this corresponds to the lowest excited state of Kr, for which E* = 9.9 eV, and hence $\eta_Q$ = 50%. It is possible to excite Kr directly in a discharge-pumped system, so the maximum possible intrinsic efficiency equals the quantum efficiency in that case.

### 2.2.3 Gain in e-beam-pumped excimer lasers

The gain of a laser is given by

$$\alpha = \sigma_s N^* \qquad 2.10$$

where $N^*$ = population inversion

$\sigma_s$ = stimulated emission cross-section

$$= \frac{1}{8\pi c\tau_s}\frac{\lambda^4}{\Delta\lambda} \qquad 2.11$$

where $c$ = speed of light

$\tau_s$ = spontaneous emission lifetime

$\lambda$ = laser wavelength

$\Delta\lambda$ = transition bandwidth

In an ideal excimer laser, $N^*$ equals the upper laser level population. The rate equation for $N^*$, below saturation, is given by

$$dN^*/dt = SB - N^*/\tau \qquad 2.12$$

where: S is the rate of ionization or excitation of the medium ($cm^{-3}\ s^{-1}$) ($= P/eW^* = (j/eW^*)dE/dx$),

B is the branching ratio of ionic and excited state kinetics leading to upper laser level excitation (e.g. B = 1 if every ion or excited atom contributes to excimer formation),

$\tau$ is the upper laser level lifetime, which may be $< \tau_s$ due to collisional quenching (see next chapter),

e is the electronic charge.

Assuming a laser pulse of duration $\tau_p > \tau$, the maximum inversion will approach

$$N^* \simeq SB\tau \qquad 2.13$$

Therefore the maximum gain is

$$\alpha \cong \frac{\sigma_s \tau j B}{eW^*}\frac{dE}{dx} \qquad 2.14$$

Note that the gain is independent of the e-beam voltage, except for a

weak variation with dE/dx. However, the range of the e-beam increases with electron energy, enabling larger volumes to be pumped.

A typical value of gain required for laboratory pulsed laser systems is 0.1 $cm^{-1}$. Consider a KrF laser operating at 3.5 bar in an argon diluent, pumped by a 500 keV e-beam. Estimated values for the parameters of equation 2.14 are:

$\sigma_s \sim 2 \times 10^{-16}$ $cm^2$

$B \sim 0.2$

$\tau \sim 1$ ns

$dE/dx \sim 3 \times 10^4$ volts $cm^{-1}$ (= 2 x Berger & Seltzer value)

$W^* \sim 20$ ev

According to these numbers, the e-beam current density in the medium required to achieve a gain $\alpha = 0.1$ $cm^{-1}$ is

$j \sim 400$ amps $cm^{-2}$

with corresponding values

$P \sim 12$ MW $cm^{-3}$

$S \sim 4 \times 10^{24}$ $cm^{-3}$ $s^{-1}$

This is consistent with measurements carried out on a transversely pumped KrF laser, described in Chapter 4.

## 2.3 E-Beam Diodes

The e-beam is formed in a vacuum ($\sim 10^{-4}$ torr) diode. A negative voltage pulse (10 ns - 1 μsec, 0.2 - 2 MeV) is applied to a cold cathode, constructed from a graphite block, metallic blades, or a metallic "cheese-grater" consisting of an array of closely spaced spikes. Very high local fields cause a dense plasma to form over the surface of the cathode by

field emission[25], from which electrons are accelerated across the diode gap towards the anode, maintained at ground potential.

The anode consists of a thin (≃ 50 μm) pin-hole free foil, usually made of stainless steel, aluminium, titanium or aluminized dielectric, which allows efficient transmission of the high energy electrons into the laser cell. To withstand the pressure difference between the vacuum diode and the high pressure laser cell, the foil may be supported by a 70-80% open grid-like structure known as a "Hibatchi". Typically 10-100 keV of beam energy is lost in the foil and support structure.

### 2.3.1 Pump geometry

The most commonly used pump configuration is rectangular geometry, in which the rectangular cross-section e-beam is transversely injected into the laser cell, in a direction orthogonal to the optical axis of the laser. Fig. 2.3 is a schematic diagram of such a system. Although relatively simple, it suffers from non-uniformity of energy deposition in the gas. Electron scatter in the anode foil causes the greatest excitation density to occur close to the foil[26,120]. More uniform energy deposition is achieved using double-sided transverse pumping, in which case two e-beams are injected in opposite directions into the laser cell. Fig. 2.4 shows the energy deposition profile for such a system. In this case more than 50% of the e-beam energy can be delivered uniformly to the laser cavity[27].

A simpler method of obtaining uniform energy deposition is radial injection of the e-beam into a cylindrical thin foil anode, co-axial with an outer cylindrical cathode[28]. A co-axial diode is shown schematically in Fig. 2.5. Use of cylindrical geometry allows up to 75-80% of the incident beam energy to be uniformly deposited in the gas laser medium[29].

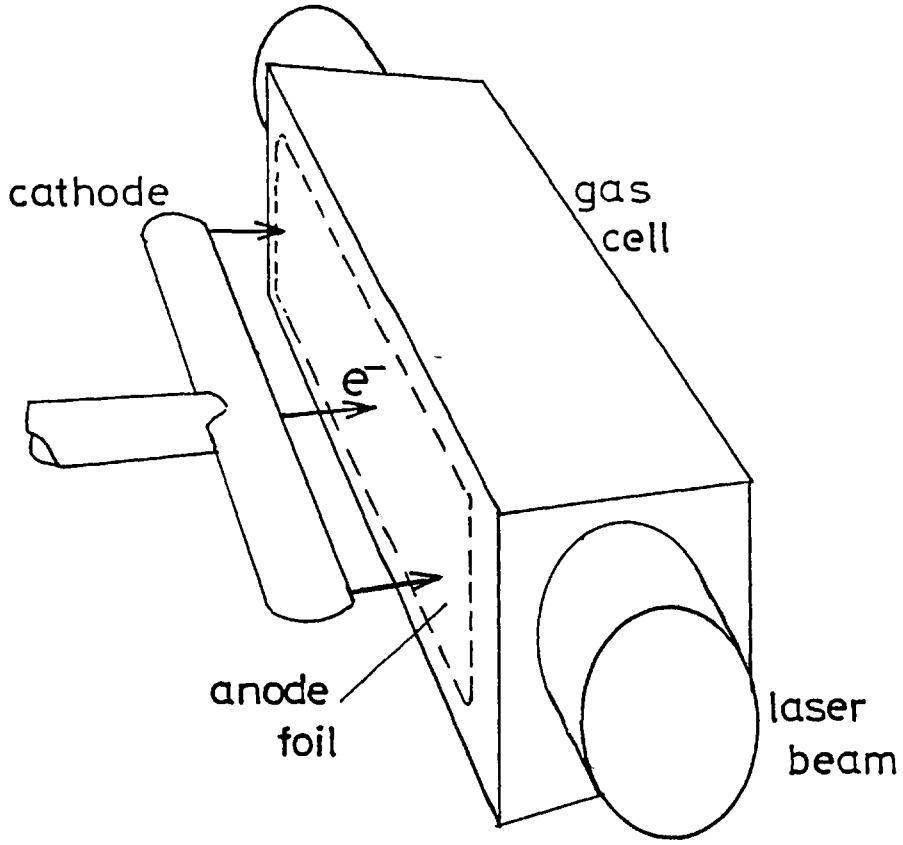


FIGURE 2.3 Schematic diagram of transversely pumped laser.

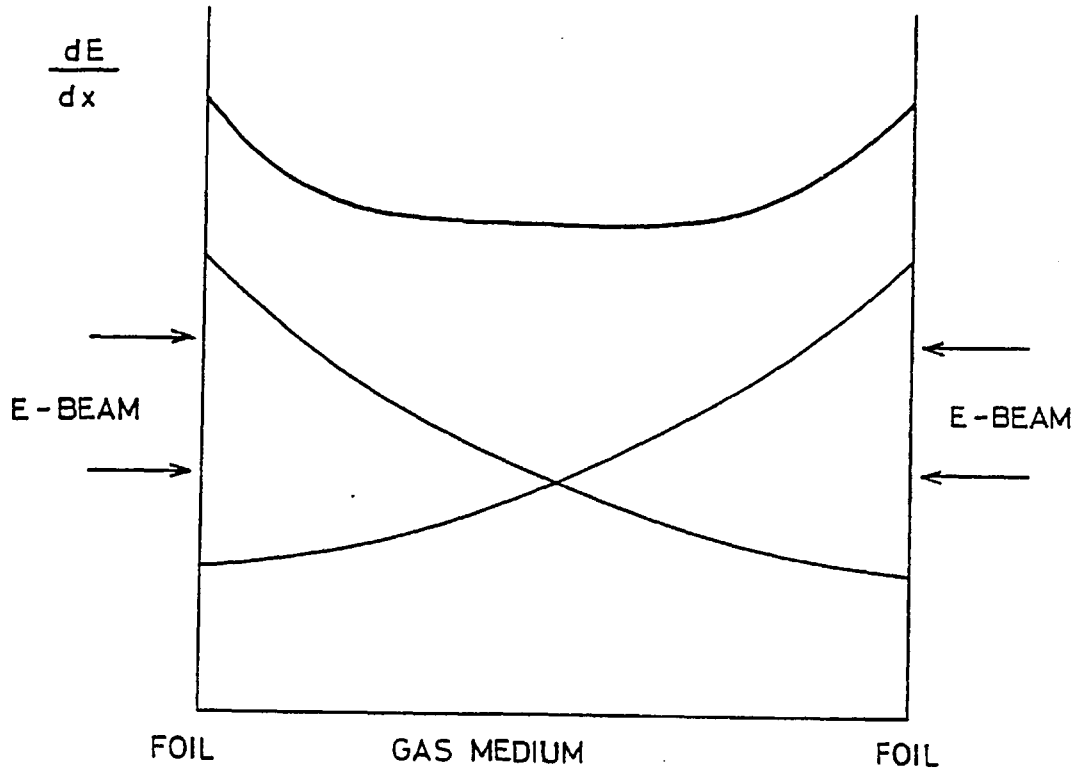


FIGURE 2.4 Energy deposition profile using double-sided transverse pumping.

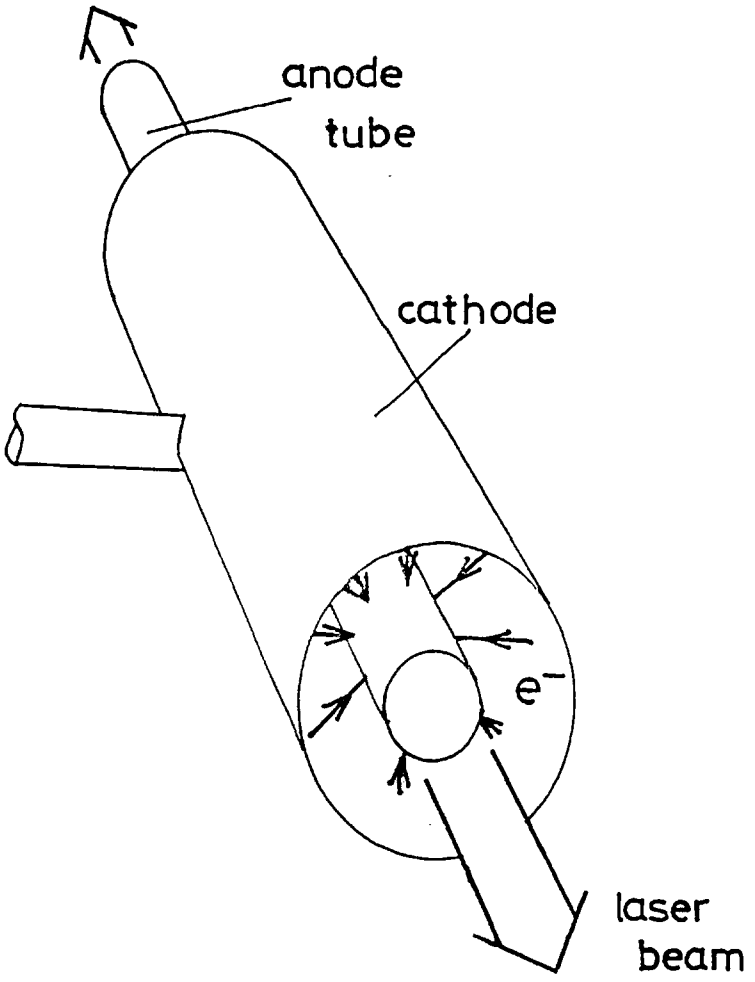


FIGURE 2.5 Schematic diagram of co-axially pumped laser.

Transverse and radial e-beam injection is suited to high pressure (> 1 bar) gas lasers, of the type constructed in the present work. At lower pressures an effective method of pumping is axial injection of the e-beam along the optical axis of the laser[12]. Magnetic steering coils bend the e-beam into one end of the laser cell and dump it into the walls at the other end, preventing damage to the windows by the e-beam. A guide magnetic field along the laser axis reduces side scatter of electrons to the walls.

### 2.3.2 Diode impedance

The high current density j of the order 100 amp $cm^{-2}$, present in a cold cathode field emission diode, is in the space-charge limited regime[30]. The maximum space-charge limited current density in a non-relativistic, biplanar diode is given by the Child-Langmuir law

$$j = \frac{2.3 \times 10^{-6} \, V^{3/2}}{d^2} \text{ amp cm}^{-2} \qquad 2.15$$

where $d$ = anode-cathode separation (cm)

$V$ = applied voltage (volts)

The equivalent expression for a co-axial diode is

$$j = \frac{2.3 \times 10^{-6} \, V^{3/2}}{r_a^{\,2} \, f(\frac{r_a}{r_c})} \text{ amp cm}^{-2} \text{ (at anode)} \qquad 2.16$$

where $r_a$ = anode radius (cm)

$r_c$ = cathode radius (cm)

$f(\frac{r_a}{r_c})$ = a function of order unity for a typical laser diode

The impedance is simply given by $Z = V/I$, where I is the total current, which gives for the biplanar diode

$$Z = \frac{V^{-1/2}\, d^2}{2.3 \times 10^{-6}\, A} \text{ ohms} \qquad 2.17$$

where A = cross-sectional area of beam ($cm^2$).

The pulse duration achievable with a cold cathode diode is limited by diode closure, i.e. collapse of the diode impedance as the cathode plasma expands across the vacuum gap d with a velocity $v_c \sim 2\text{-}3 \times 10^6$ cm $s^{-1}$ [25], decreasing the effective gap. The gap d is typically $\sim$ 1-2 cm, determined by the required impedance Z. Closure times are of order 0.5 - 1 μsec, but the impedance will drop 50% in one quarter of this time, because of the $d^2$ dependence.

### 2.3.3 Beam pinch

A phenomenon which limits total e-beam current I is beam pinch, caused by the self-magnetic field of the e-beam or return current to ground. An electron accelerating towards the anode is deflected through an angle θ by the magnetic field B. The self-magnetic field is usually strongest at the edges of the beam, so that at high I the beam pinches in towards the centre of the diode, resulting in non-uniform energy deposition in the laser cell and severe heating and possible rupture of the anode foil. Fig. 2.6 shows beam pinch in a co-axial diode, where return current I/2 flows axially through each end of the anode to ground. The magnetic field at the edges of the beam at the anode is given by Ampere's law as

$$B = \frac{\mu_o I}{4\pi r_a} \quad \text{(tesla)} \qquad 2.18$$

where $\mu_o$ = permeability of free space = $4\pi \times 10^{-7}$ H $m^{-1}$

$r_a$ = anode radius (m)

Schlitt and Bradley[31] have derived approximate expressions for the angle of pinch of a relativistic e-beam in both transverse and co-axial

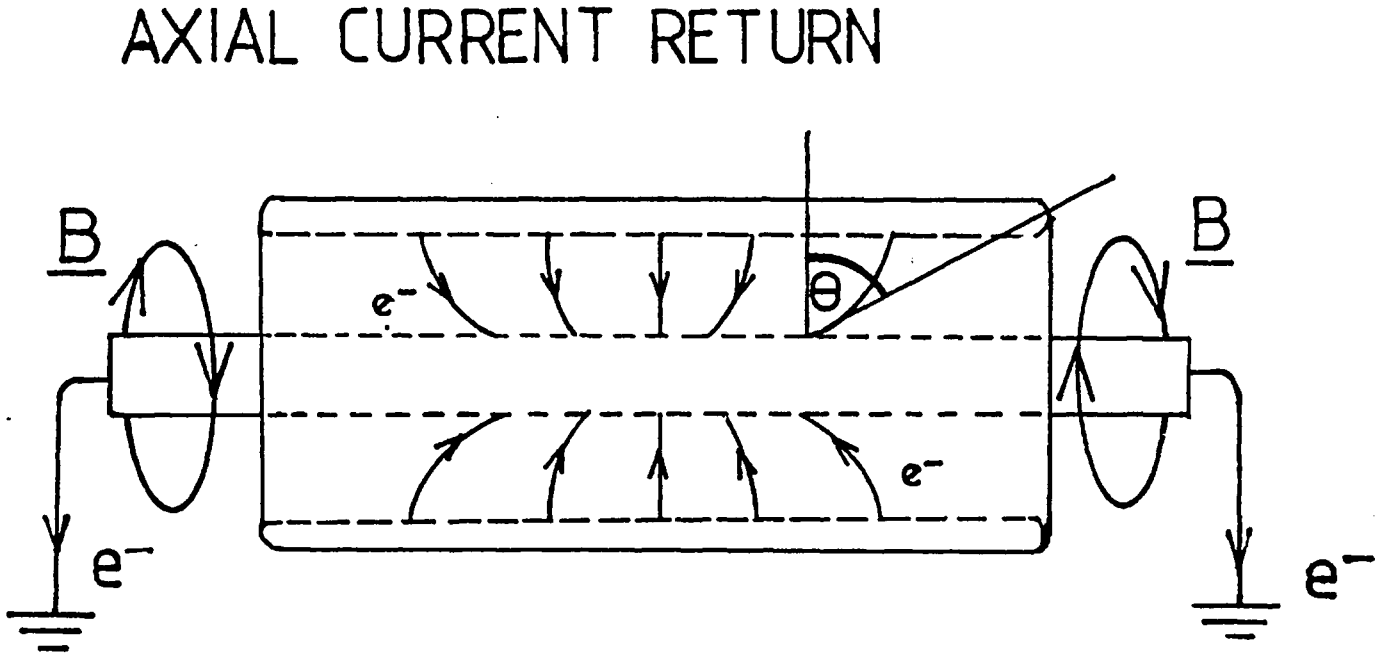


FIGURE 2.6 Beam pinch in a co-axial diode.

diodes. The maximum deflection of an electron at the anode at the beam edge is approximately

$$\theta = \sin^{-1} (d/r_L) \quad \text{(transverse)} \tag{2.19}$$

$$\theta = \sin^{-1} \left( \frac{r_a}{r_L} \ln \frac{r_c}{r_a} \right) \quad \text{(co-axial)} \tag{2.20}$$

where $r_c$ = cathode radius (m)

$d$ = anode-cathode gap (m)

$r_L = (\gamma\beta/B) \times 1.7 \times 10^{-3}$

$B$ = magnetic field at anode

$\gamma = (1 - \beta^2)^{-\frac{1}{2}}$

$\beta = v/c$

$v$ = electron speed

$c$ = speed of light

For the co-axial case, B is given by equation 2.18. Substitution of B by 2.18 in equation 2.20 gives a cut-off current $I_c$, defined as the value of I which results in $\theta = 90^o$, of

$$I_c = \frac{17\beta\gamma}{\ln(r_c/r_a)} \text{ kA} \tag{2.21}$$

Numbers applicable to a co-axial diode, described later, are

$r_a$ = 1.9 cm

$r_c$ = 4.2 cm

$V$ = 500 keV ($\beta = 0.86$, $\gamma = 2$)

implying $I_c$ = 37 kA.

Actual peak current = 35 kA, so the diode operates close to cut-off for a short time.

In general, beam pinch occurs at lower current levels in co-axial, as opposed to transverse diodes, due to the stronger magnetic field set

up by the return current in the former case. However, scaling studies have shown[29] that co-axial diode e-beam operation in the region of I = 180 kA and V = 1 MV can be achieved, using a large diameter (20 cms) anode and annular blade cathodes.

Another way to achieve very high current levels is to divide the diode into magnetically isolated modules, each carrying less than the critical current $I_c$. Fig. 2.7 shows two possible diode modularization geometries. Modularization imposes no upper limit on e-beam current: I total = nI, where I is the current to each module and n is the number of modules. Disadvantages are complexity and increasing length of the laser with pumping power.

A type of diode constructed in the present work, shown schematically in Fig. 2.8, utilizes a simple geometry which allows the current to be increased with no limitation due to beam pinch[32,33]. A longitudinal slot in the cathode allows return current to flow radially out of the diode along a conducting plane to earth, instead of along the ordinary axial path to ground.

The effect of this is to reduce the magnitude of B for a given current I, and to change its direction favourably. Any electron emitted in the gap region between the cathode and the conducting radial return plane will tend to be deflected towards the cylindrical anode, hence increasing coupling of the e-beam to the laser gas medium and providing more uniform excitation. Equation 2.19 is used to estimate the deflection of an electron initially moving along the normal to the radial return plane, where d in this case is the distance between the cathode and the plane.

We require the magnetic field B at a point P near the cylindrical anode, a distance R above the radial return plane (see Fig. 2.9).

Assume $L^2 >> R^2$, $W^2 >> R^2$, infinitely thin plane. The field $\underline{dB}$ at P due to a semi-infinite current strip $\underline{dI}$ is

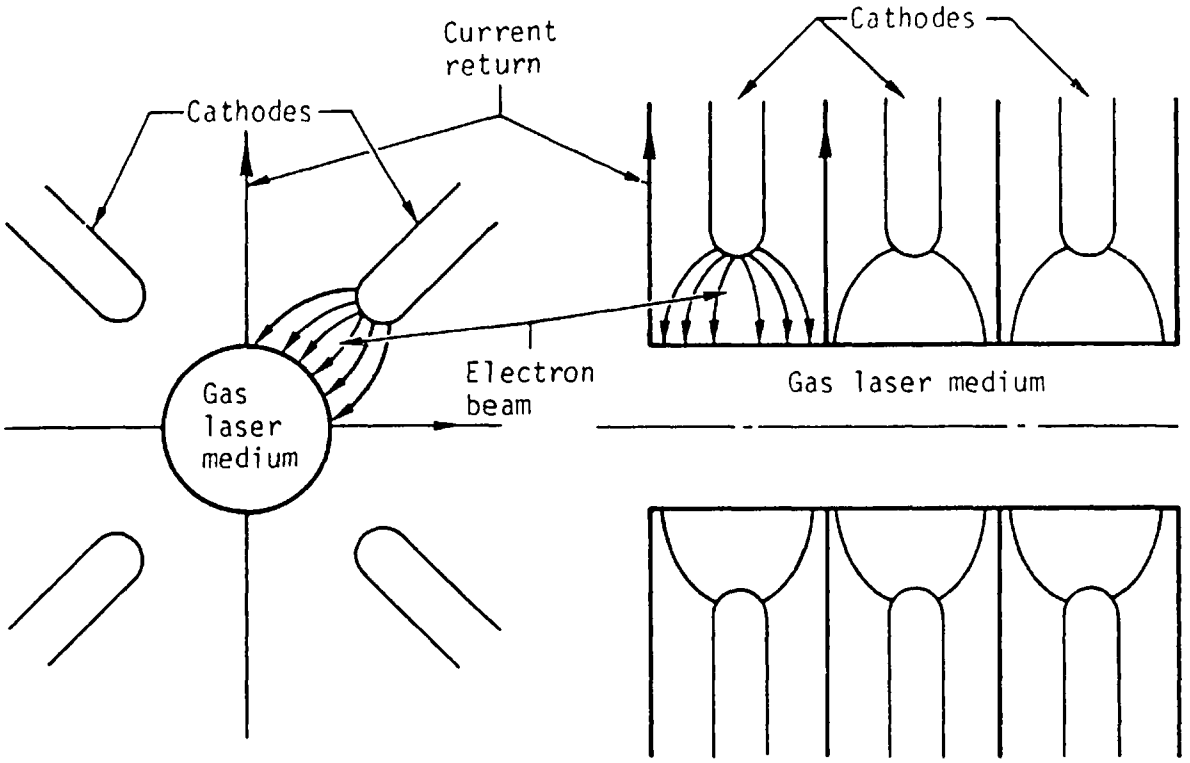


FIGURE 2.7 Diode modularization geometries (from reference 27).

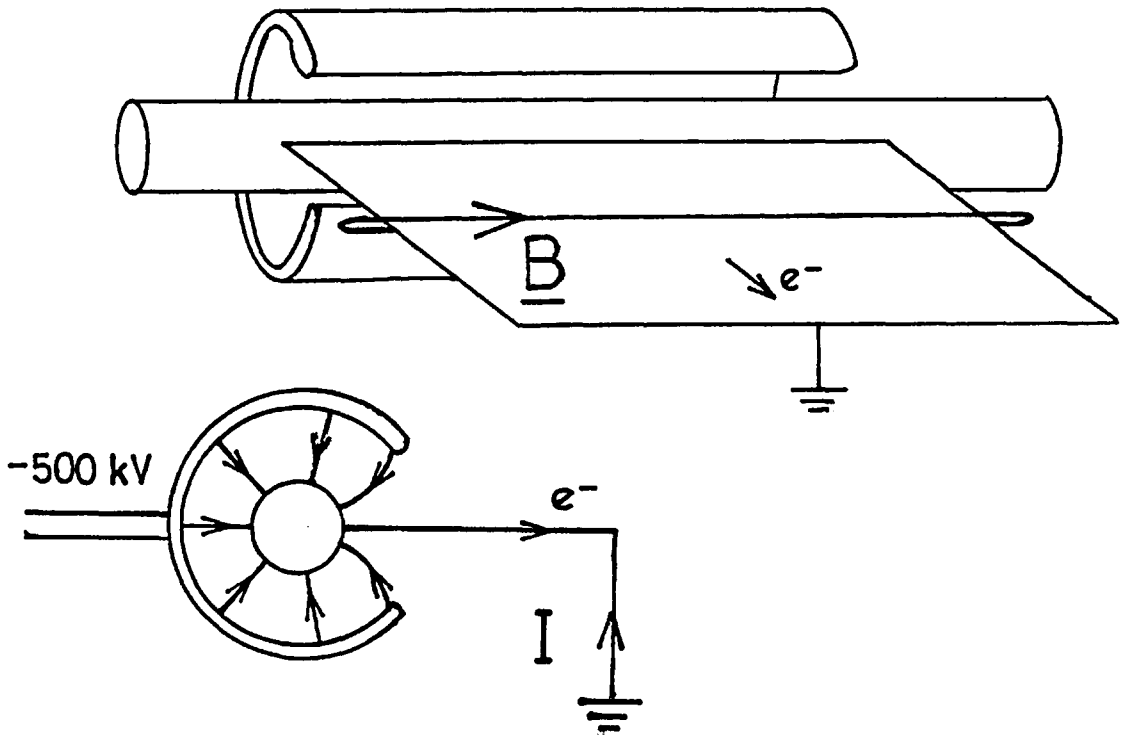


FIGURE 2.8 Diode using radial current return geometry.

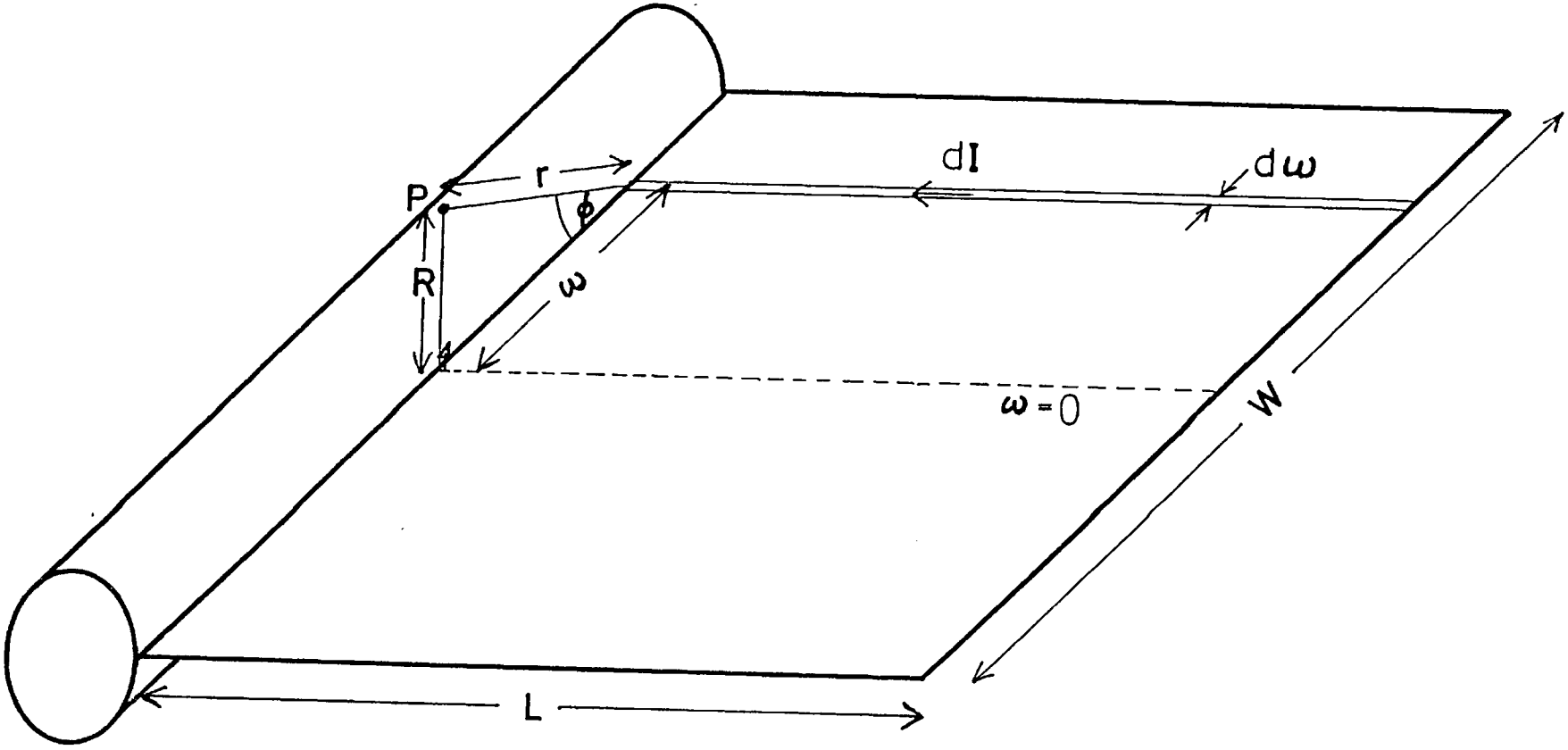


FIGURE 2.9 Geometry of magnetic field calculation.

$$\underline{dB} = \frac{\mu_o dI}{4\pi r} \qquad 2.22$$

By symmetry $\underline{B}$ is parallel to anode cylinder axis, and component dB in that direction is

$$dB = \frac{\mu_o \sin\phi \, dI}{4\pi r} \qquad 2.23$$

where $\sin\phi = R/r$, $r^2 = R^2 + w^2$. Therefore

$$dB = \frac{\mu_o R \, dI}{4\pi(R^2 + w^2)} \qquad 2.24$$

If total current = I, current density i = I/W amp $m^{-1}$, dI = idW. Therefore

$$dB = \frac{\mu_o RI \, dw}{4\pi W(R^2 + w^2)}$$

$$B = \frac{\mu_o RI}{4\pi W} \int_{-W/2}^{W/2} \frac{dw}{R^2 + w^2}$$

$$= \frac{\mu_o I}{2\pi W} \tan^{-1} \frac{W}{2R}$$

$$\simeq \frac{\mu_o i}{4} \qquad 2.25$$

Substitution of 2.25 into 2.19 gives a deflection angle

$$\theta = \sin^{-1} (id/5400 \, \gamma\beta) \qquad 2.26$$

Therefore the cut-off condition ($\theta = 90^o$) is given by

$$id = 5400 \, \gamma\beta \text{ amps} \qquad 2.27$$

Therefore there is no limitation due to pinch on current density i if d is decreased proportionately, and therefore no corresponding limit on

e-beam pump power. Note that cut-off to the plane corresponds to complete coupling into the cylindrical anode.

A diode using radial return geometry is described in detail in Chapter 5.

## 2.4 Marx Generator

The Pulserad 110A uses a Marx generator to store energy and develop high voltages. The Marx is an assembly of high voltage capacitors, pressurized spark gap switches, and resistors. Its mode of operation is the sudden conversion of a bank of capacitors charged in parallel to a series configuration. Fig. 2.10 is a schematic of a 4 stage Marx. During the charging cycle, each capacitor is charged to a voltage $V_c$ by the H.T. D.C. supply (10-100 kV). To erect the Marx, the first spark gap is triggered by a voltage ($\sim$ 50 kV) applied to a third electrode which causes the gas ($SF_6$ or $N_2$) to break down and become conducting, with a resistance of $\sim$ 1 ohm. The first two stages are thus effectively in series (since R >> switch resistance) and develop a voltage $2V_c$ across them. This is enough to cause self-breakdown in the second spark gap, and so the process continues until all the stages are in series, with a total output voltage $V_o = 4V_c$ in this example. To reduce jitter to a few tens of nanoseconds, all the spark gaps can be triggered.

Fig. 2.11 is the circuit of the Marx generator in the Pulserad 110A. It has 10 stages, each with a capacity of 0.05 $\mu$F. Each of the stages actually comprises two 0.1 $\mu$F capacitors contained in one case and connected in series between the terminals. The midpoint connection of the two capacitors is connected to the case and hence to ground. At full charge, each capacitor is charged to $\pm$ 50 kV with respect to ground, to give a total voltage $V_c$ = 100 kV across the spark gap. Assuming

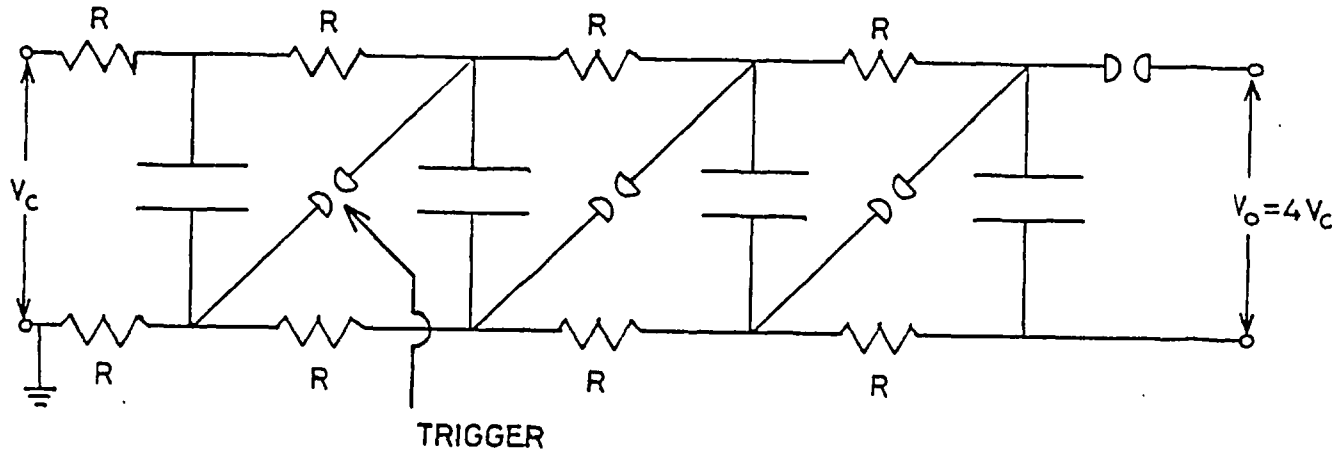


FIGURE 2.10 Schematic diagram of 4-stage Marx Bank.

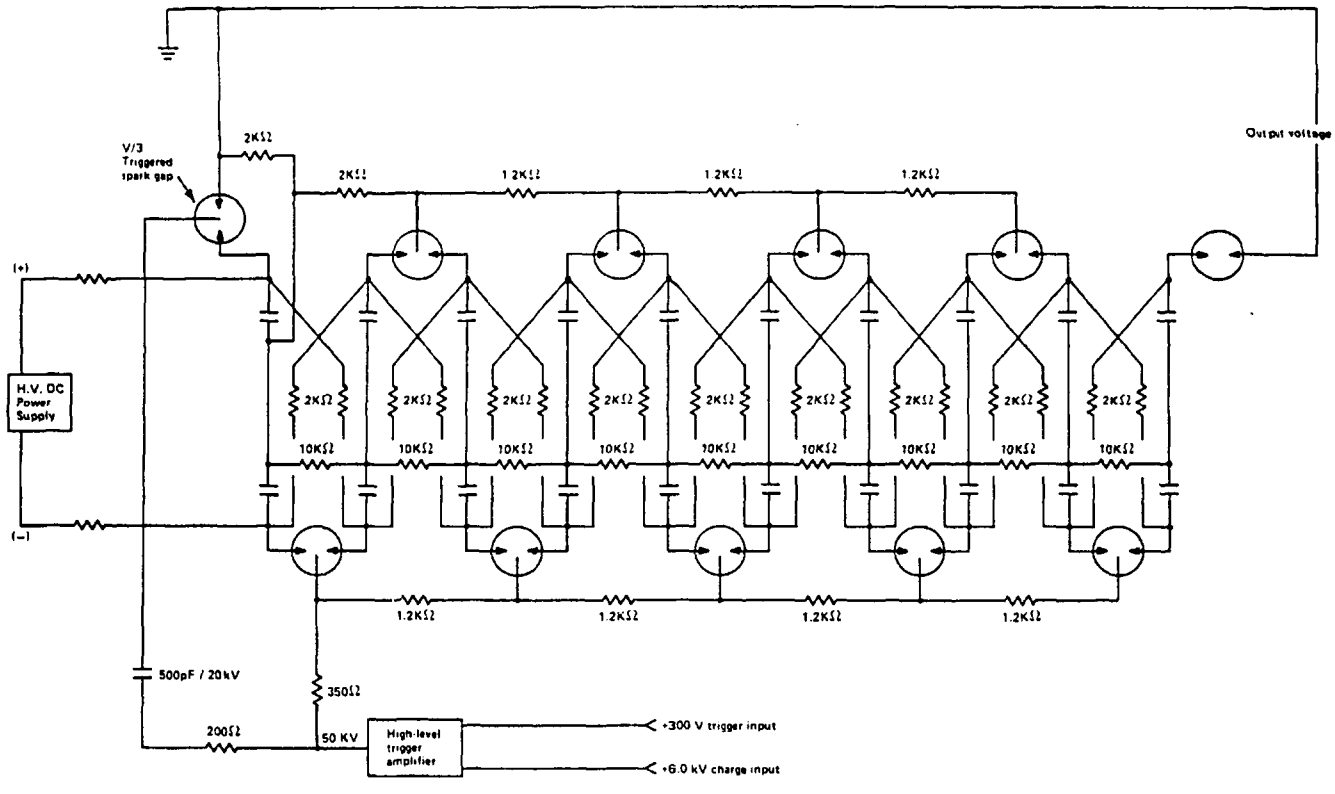


FIGURE 2.11 Pulserad 110A Marx generator circuit

negligible losses in the resistors in the time of interest, the output voltage of the generator is

$$V_o = 10\ V_c = 1\ MV$$

The resistors are made of $CuSO_4$ solution contained in PVC tubing, with copper end connections.

The spark gap switches are pressurized with dry sulphur hexafluoride ($SF_6$). The pressure is adjusted so that they operate at $\sim$ 75% of self-breakdown voltage, e.g. at 43 p.s.i.g. at 100 kV.

The entire Marx assembly is insulated by transformer oil, and contained within a large cylindrical casing.

The output capacity $C_M$ of the Marx is 5 nF, series resistance $R_M \sim$ 10 ohms, and total series inductance $L_M \sim$ 5 μH. Total stored energy at maximum charge is 2.5 kJ.

## 2.5 Co-Axial Pulse Forming Line

The output voltage $V_o$ of the relatively high inductance Marx generator can be applied directly to the electron gun, if long pulse operation is required and the slow rise time can be tolerated. Rise and fall times are approximately $L_M/R$ and $RC_M$ respectively, where R is the total series resistance of Marx and e-beam diode. For laser applications, such pulses are frequently not acceptable, since the low energy electrons produced during the rise time deposit most of their energy in the anode foil, causing excessive foil heating and inefficient energy transmission. For this reason a pulse forming line (PFL) is usually used, to produce a shorter, more square pulse in the diode.

The basic PFL circuit of the Pulserad 110A is shown in Fig. 2.12. The PFL in this case is a co-axial transmission line of length $\ell$ = 2 m,

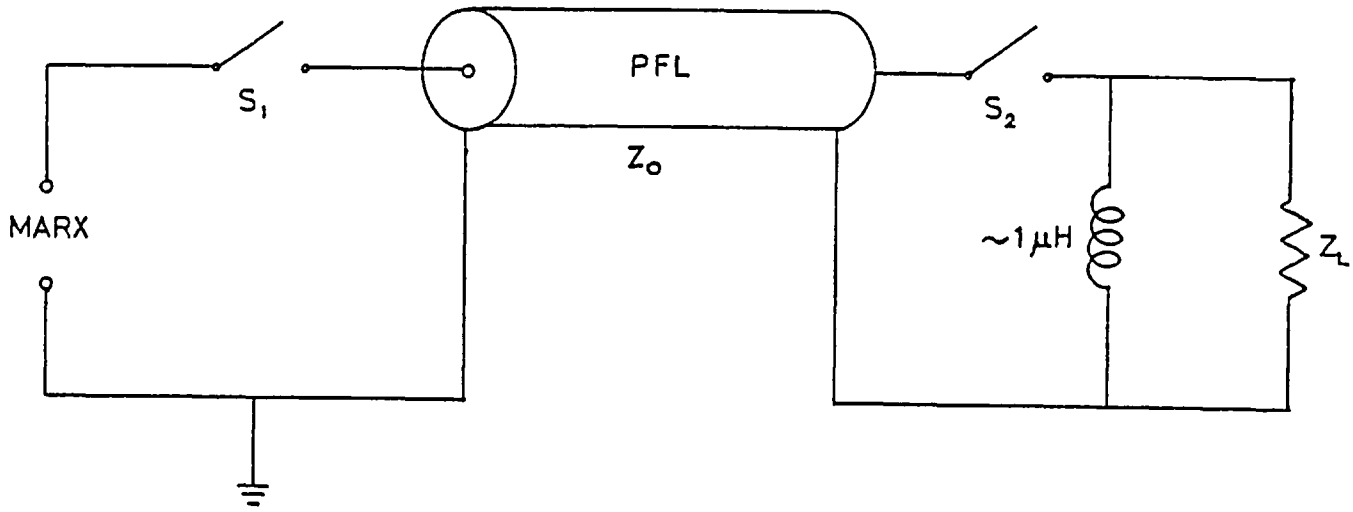


FIGURE 2.12 Basic PFL circuit of Pulserad 110A.

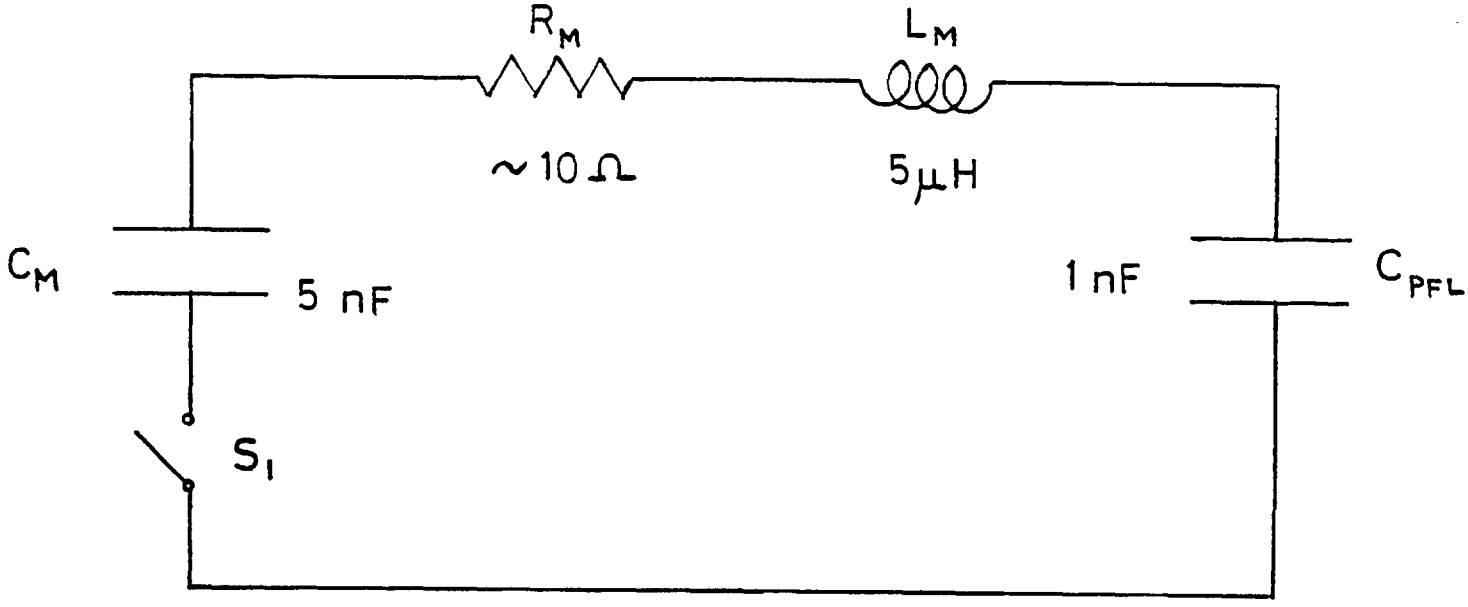


FIGURE 2.13 Equivalent charging circuit between Marx and PFL.

inner diameter $r_1$ = 45 cm, outer diameter $r_2$ = 59 cm, immersed in transformer oil of dielectric constant $\varepsilon$ = 5.

Therefore:

$$C_{PFL} = \frac{2\pi\varepsilon\varepsilon_o \ell}{\ell n(r_2/r_1)} \simeq 1nF \qquad 2.27$$

$$L_{PFL} = \frac{\mu_o \ell}{2\pi} \ell n(r_2/r_1) \simeq 0.1\ \mu H \qquad 2.28$$

$$Z_o = (L_{PFL}/C_{PFL})^{\frac{1}{2}} \simeq 10 \text{ ohms} \qquad 2.29$$

where $C_{PFL}$, $L_{PFL}$ and $Z_o$ are the capacity, inductance and impedance, respectively, of the PFL.

When the last spark gap $S_1$ in the Marx generator breaks down, the PFL is pulse-charged relatively slowly and acts as a capacitor. The equivalent charge circuit is shown in Fig. 2.13.

The differential equation governing the charge on the PFL $Q_{PFL}(t)$ at time t is

$$\ddot{Q}_{PFL} + (R_M/L_M)\dot{Q}_{PFL} + (1/L_M C)Q_{PFL} + V_o/L_M = 0 \qquad 2.30$$

where $C = C_M C_{PFL}/C_M + C_{PFL}$. Boundary conditions are $Q_{PFL}(0) = \dot{Q}_{PFL}(0) = 0$.

The system is underdamped, with a solution for the voltage on the PFL

$$V_{PFL}(t) = \frac{C_M V_o}{C_M + C_{PFL}} \left[1 - e^{-\alpha t}\left(1 + (\tfrac{\alpha}{\omega})^2\right)^{\frac{1}{2}} \cos(\omega t + \theta)\right] \qquad 2.31$$

where $\alpha = R_M/2L_M$, $\omega = \left(\frac{1}{L_M C} - \frac{R_M^2}{4L_M^2}\right)^{\frac{1}{2}}$, $\theta = \tan^{-1}\left(\frac{-\alpha}{\omega}\right)$.

Inspection of 2.31 shows that if $\alpha << \omega$ and $C_M >> C_{PFL}$, $V_{PFL}$ can approach twice the initial output voltage $V_o$ of the Marx, at the end of

the first half-cycle of charge. Fig. 2.14 sketches the waveform of 2.31. Putting the known values into 2.31 gives an actual maximum pulse-charge ratio $V_{PFL}/V_o$ of 1.5 at a time t = 200 ns.

In practice, for stability the PFL is switched into the diode via $S_2$ (see Fig. 2.12) before $V_{PFL}$ reaches a maximum, which reduces the pulse-charge ratio somewhat, and the ratio is further reduced by stray circuit resistance and capacitance.

$S_2$ is an $SF_6$ pressurized spark gap, adjusted to close in the range 90-95% of the peak voltage $V_{PFL}$. Typical gas pressure was 83 p.s.i.g. for full power operation of the Pulserad. When $S_2$ closes, the PFL acts as a transmission line and rapidly discharges into the low inductance, resistive diode load $Z_L$ (see Fig. 2.12). (The high inductance in parallel with the load provides a path to ground for the remaining Marx charge at later times.)

Maximum power is dissipated in the load if it is matched with the PFL ($Z_L = Z_o$), and the diode was therefore designed to have an impedance near 10 ohms. Fig. 2.15 shows voltage $V_L$ and current $I_L$ pulses in a purely resistive load $R_L$, during discharge of a lossless transmission line initially charged to $V_T$, in matched and unmatched systems[34]. Note that the load voltage is half the charge voltage for the matched case. The transit time $\delta$ is determined by the velocity of propagation of electromagnetic radiation in the transmission line and is given by

$$\delta = \varepsilon^{\frac{1}{2}} \ell/c \qquad 2.32$$

where the symbols are as previously defined. For $\varepsilon = 5$, $\ell = 2$ m, we have $\delta = 15$ ns. In reality, perfectly square pulses are not seen, due to switch and gun impedance and the variation of $Z_L$ with applied voltage. Fig. 2.16 shows actual current waveforms in a transversely pumped diode.

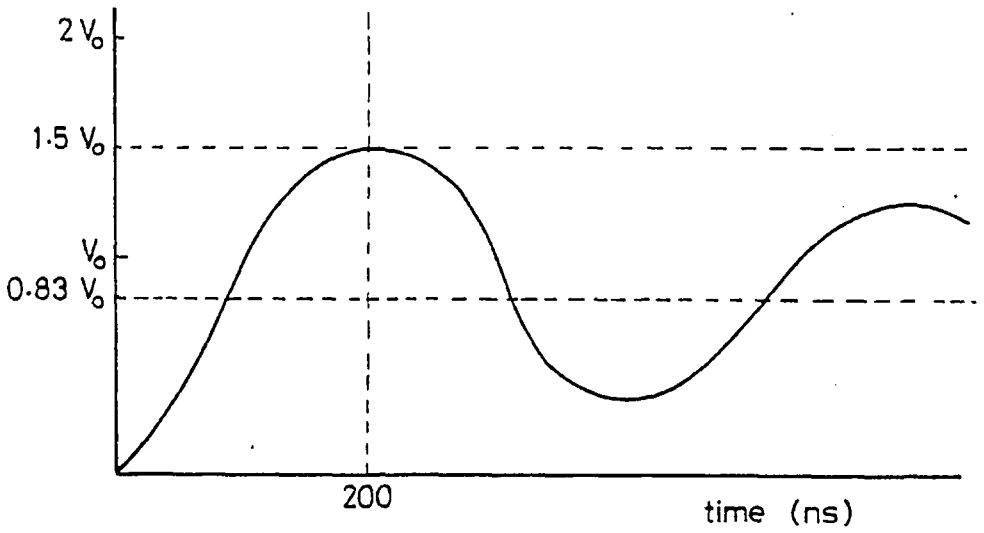


FIGURE 2.14 Charging waveform of PFL.

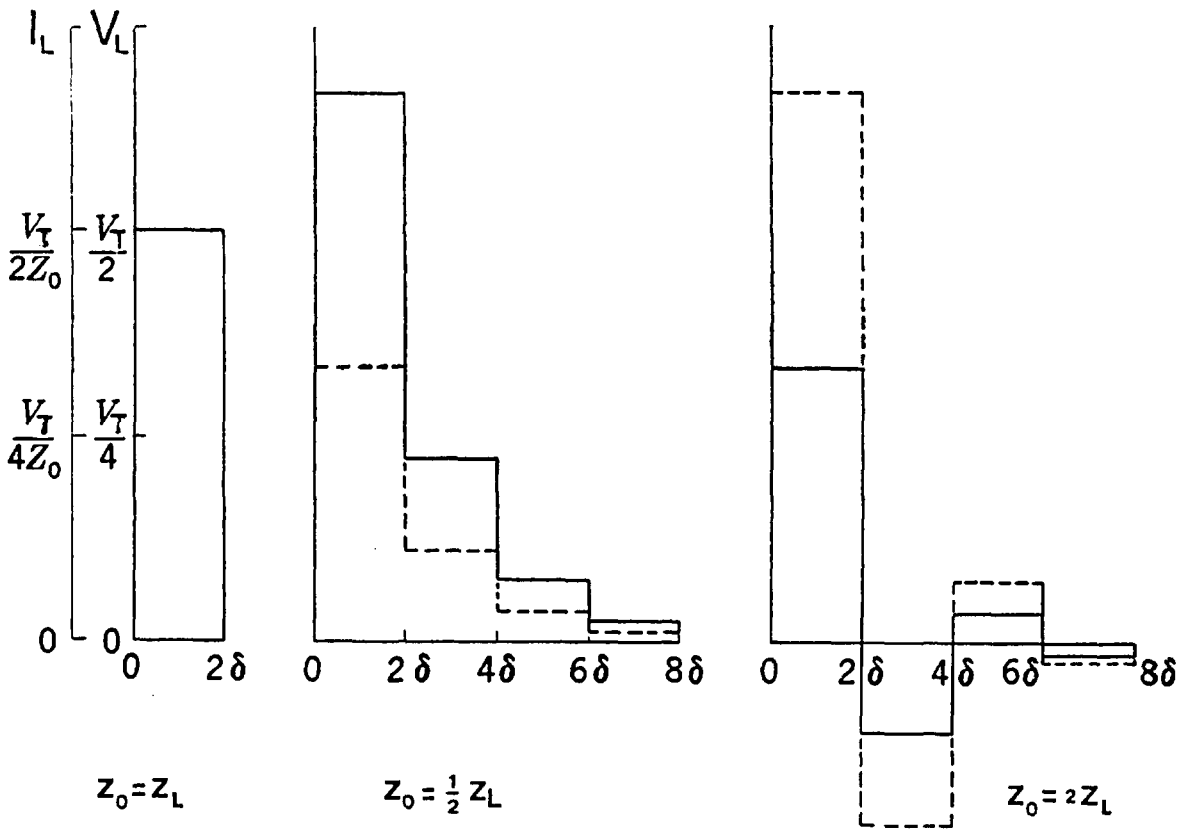


FIGURE 2.15 Voltage $V_L$ and current $I_L$ pulses in a purely resistive load $R_L$, during discharge of a lossless transmission line initially charged to $V_T$. Solid line is voltage, broken line is current.

FIGURE 2.16 Current waveforms in transverse diode, 27 kA/div, 20 ns/div.

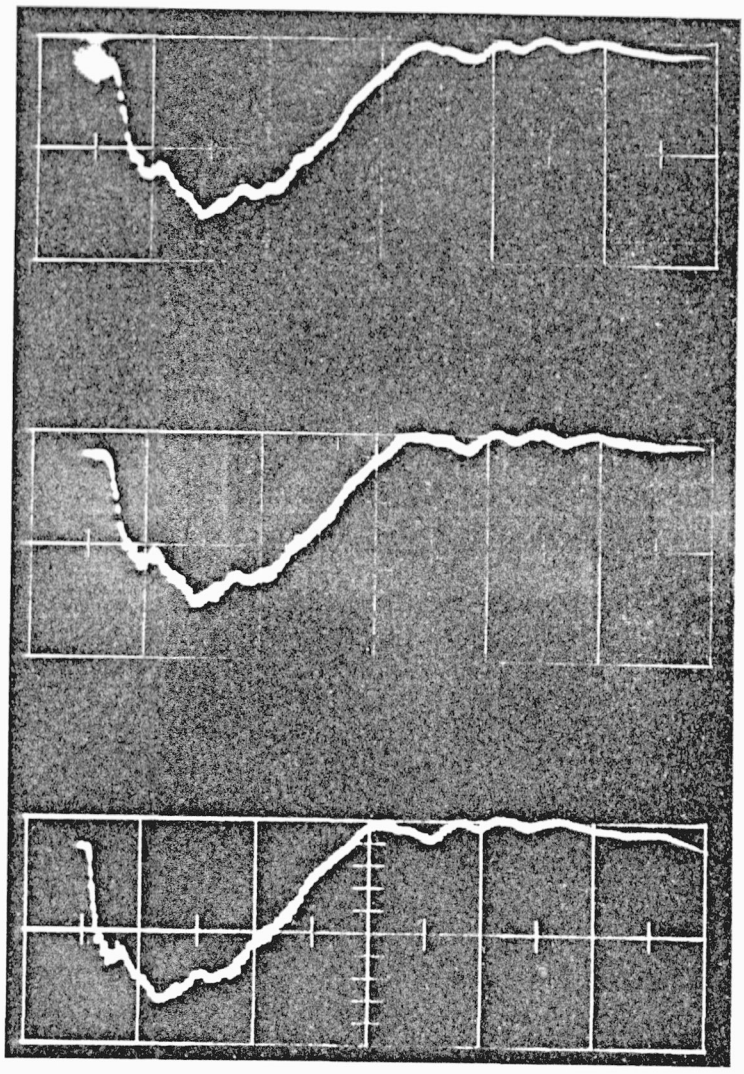

## 2.6 Blumlein

For the sake of completeness, we mention here a PFL circuit in widespread use, called a Blumlein after its inventor, in which there is no voltage loss in a matched load. Fig. 2.17 shows the basic circuit in its folded form. The Marx generator pulse charges the central plate relatively slowly, until at peak charging voltage V the spark gap S breaks down. For a matched line ($Z_L = 2Z_o$), voltage pulses travelling along the upper and lower transmission lines produce a square voltage pulse in the load of amplitude $V_L = V$, duration $t = 2\delta$, where $\delta$ is the pulse propagation time along the line as defined earlier.

Although flat plate transmission lines can be used in e-beam generators, a co-axial version is also commonly used, consisting of an inner, middle and outer conductor. The co-axial geometry is obtained by rotating Fig. 2.17 about an axis just above the upper line.

Since it is not possible to vary $Z_o$ greatly, due to the logarithmic dependence on dimensions, the Blumlein is best suited to high impedance laser diodes. For example, the Blumlein option supplied with the Pulserad has an output impedance of 43 ohms, compared with the simple transmission line impedance of 10 ohms.

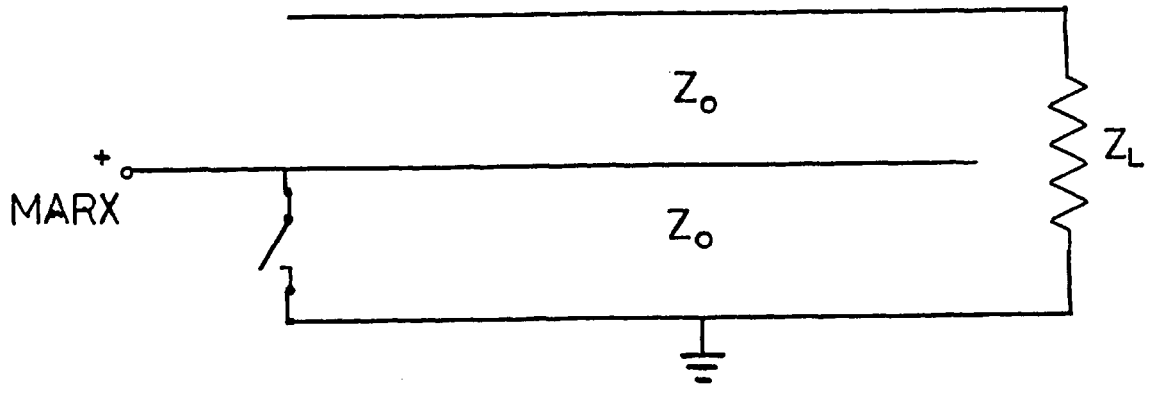


FIGURE 2.17 Folded Blumlein circuit.

CHAPTER 3

# SPECTROSCOPY AND KINETICS OF THE RARE GAS HALIDES

## 3.1 Spectroscopy

Soon after the rare gas halides were first discovered, Ewing and Brau[35] predicted their spectroscopic properties, using the close similarity between excited rare gas atoms and the neighbouring alkali metal in the Periodic Table. The rare gases require a large amount of energy to raise them to the first excited state (8 eV in xenon, 20 eV in helium). The excited s-electron orbits at relatively large distances from the nucleus, and effectively "sees" a nearly closed shell inner core of net charge $^{+}e$ - very similar to the situation in an alkali metal. Fig. 3.1 is a term diagram of the energy levels of krypton and its neighbouring alkali, rubidium. This shows how the similarity between excited krypton ($4p^5 5s^1$) and ground state rubidium extends to the higher energy levels and the binding energy. The analogy explains how excited rare gas atoms can form bound states with halogen atoms, for chemically they act like the highly reactive alkali metals. Predictions of the structure of the rare gas halides can be made using spectroscopic information gained from the extensively studied alkali halides.

Fig. 3.2 shows how the analogy is used to predict the emission wavelengths of the rare gas halides. The lowest excited state RgX* is ionically bound and correlates with the rare gas positive ion $Rg^{+}(^2P)$ and the negative halogen ion $X^{-}(^1S)$ at infinite nuclear separation. The potential energy at infinity equals the ionization potential of the rare gas I.P.(Rg) minus the electron affinity of the

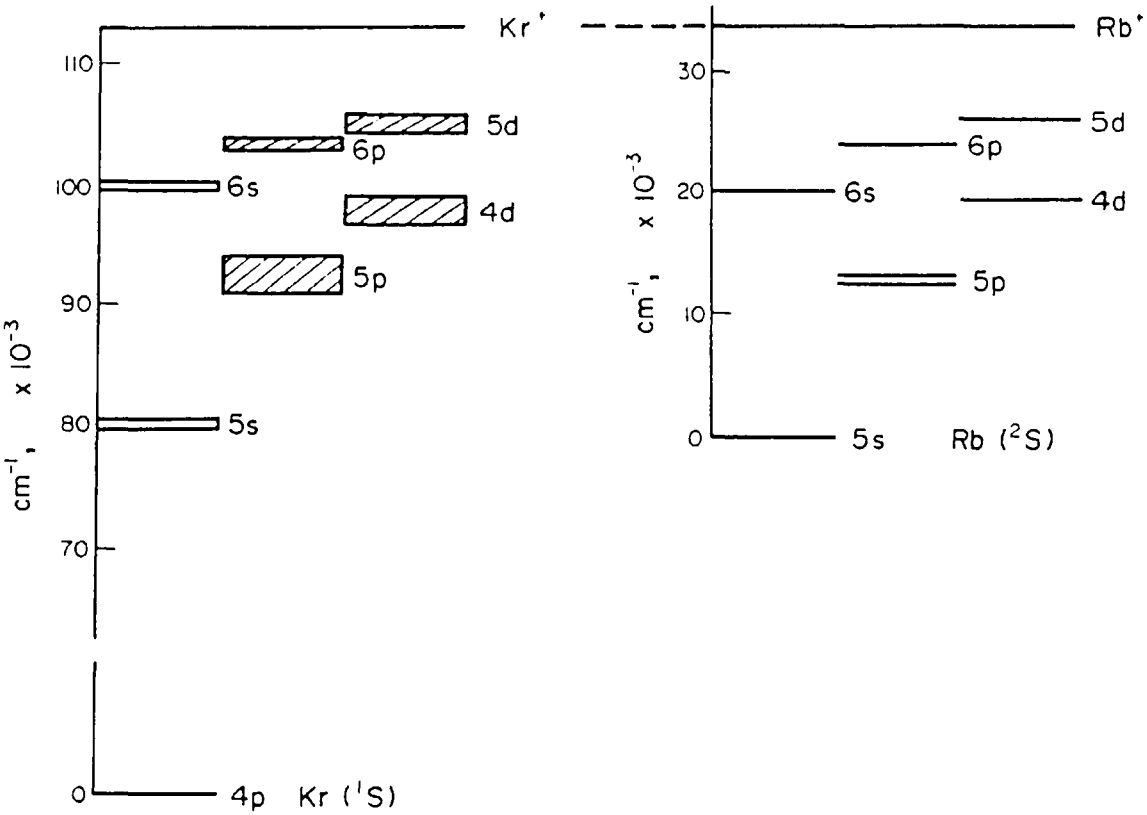


FIGURE 3.1 Comparison of energy levels of krypton and rubidium (from reference *52*).

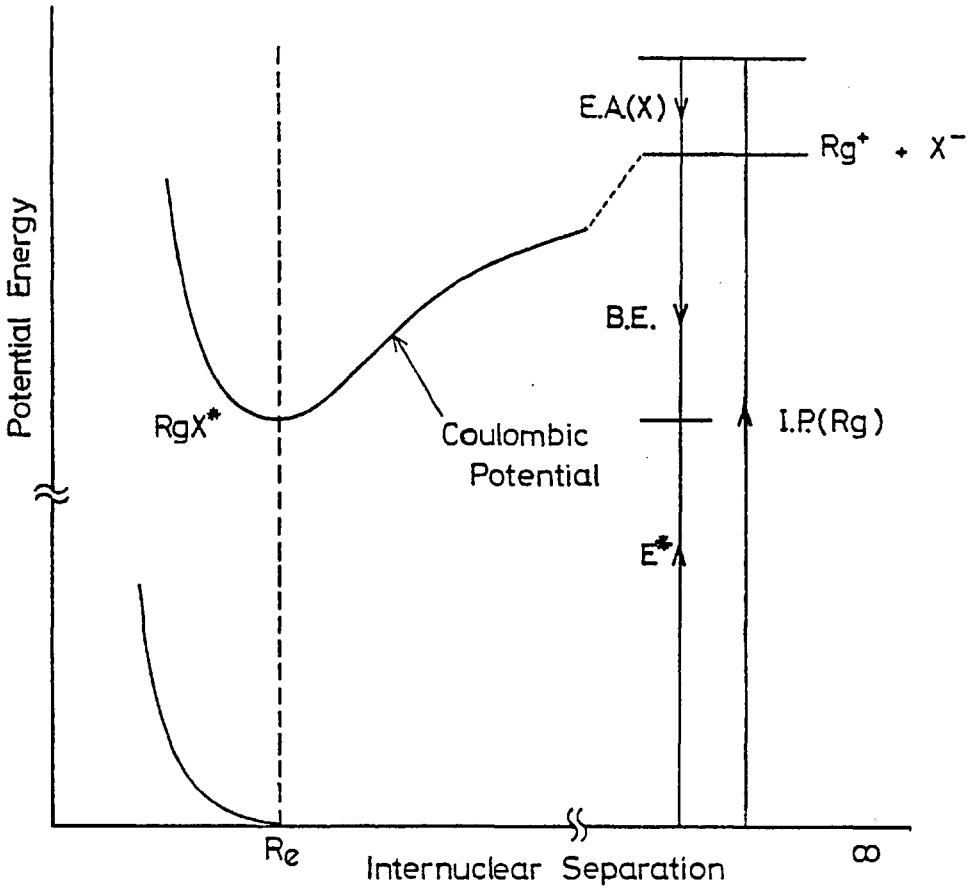


FIGURE 3.2 Generalized potential energy diagram for rare gas halides.

halogen E.A.(X). The potential follows a Coulombic curve, and the minimum is calculated assuming that the equilibrium internuclear separation $R_e$ is the same as that of the analogous alkali halide. The potential well depth is therefore equal to the binding energy of the analogous alkali halide B.E., and the excitation energy E* of the ionic state is given by the expression

$$E^* \simeq \text{I.P.(Rg)} - \text{E.A.(X)} - \text{B.E.} \qquad 3.1$$

The emitted photon energy is approximately E*, since the ground state potential is usually almost flat near $R_e$. Using this model, Brau and Ewing predicted the emission wavelengths to within a few percent, in most cases.

Fig. 3.3 is a potential energy diagram showing the ground and ionic state manifolds of KrF. At close internuclear separation, the ionic state splits into $^2\Sigma$ and $^2\Pi$ molecular states, which would be almost degenerate in the absence of spin-orbit effects[36]. The $^2\Sigma$ state usually lies lowest and is conventionally referred to as the B state. Spin-orbit effects are important in the heavier rare gas ions, e.g. the $Kr^+(^2P)$ ground state is split ($^2P_{1/2}$, $^2P_{3/2}$) by 0.67 eV, $Xe^+(^2P)$ by 1.3 eV, and spin-orbit coupling splits the $^2\Pi$ state into states of $\Omega$ (total axial angular momentum) = $^1/_2$ and $^3/_2$. The $\Omega = {}^1/_2$ state lies higher and correlates with the $^2P_{1/2}$ rare gas ion, and is referred to as the D state. The $\Omega = {}^3/_2$ state correlates with the lower $^2P_{3/2}$ ion, and is referred to as the C state. The B and C states are almost degenerate.

The ground state is covalently bonded, and correlates with the $^1S$ ground state rare gas atom and the $^2P$ halogen atom at infinite nuclear separation. At close internuclear separation, the potential curve splits into a lower $^2\Sigma$ and an upper $^2\Pi$ state, referred to as the X and

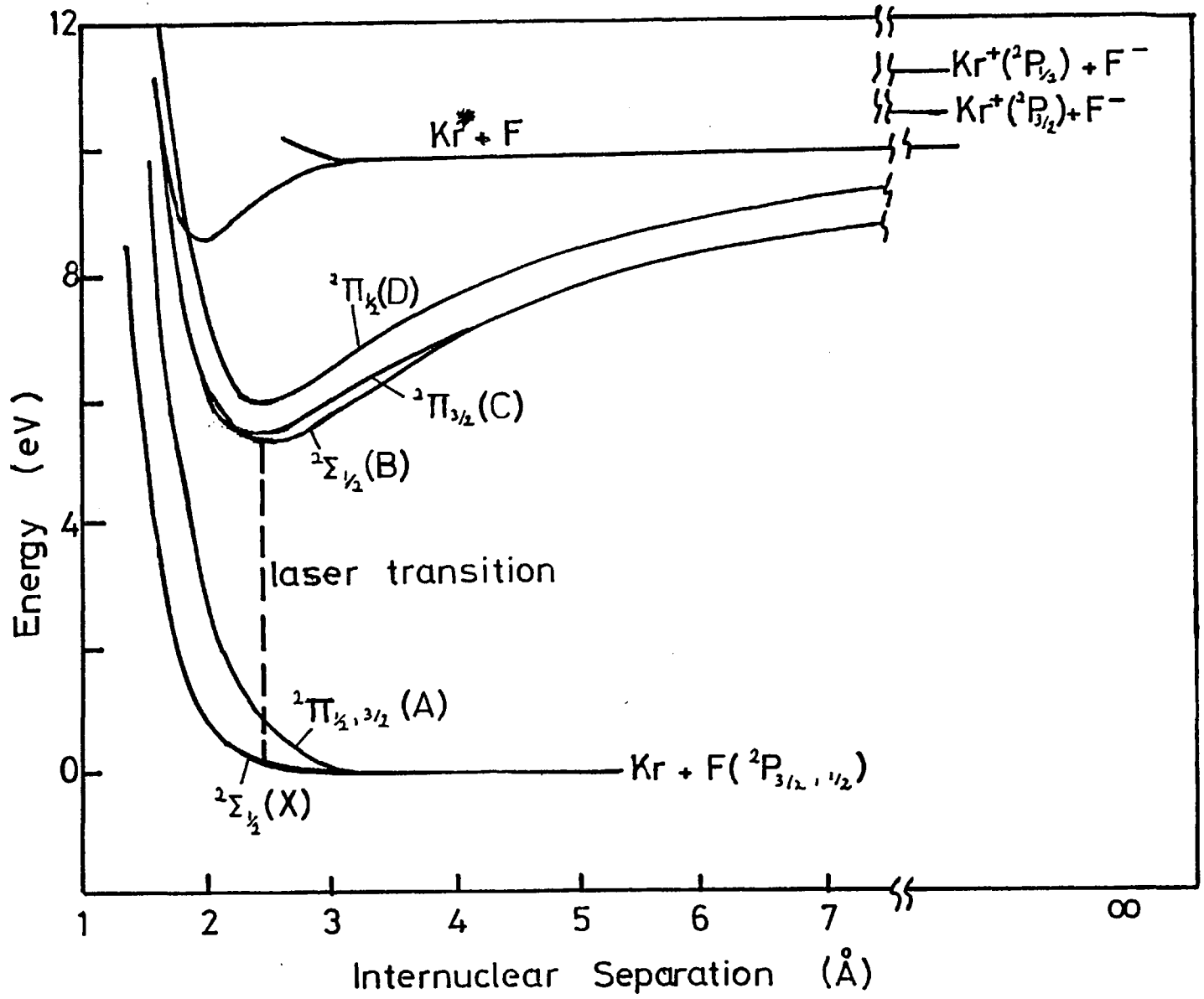


FIGURE 3.3 KrF potential energy diagram (adapted from J.J. Ewing, Physics Today, May 1978).

A states, respectively. Like the ionic state, the $^2\Pi$ state is split by spin-orbit effects (caused by the $^2P$ halogen atom) into $\Omega = {}^1/_2$ and ${}^3/_2$ states. However, except for the heaviest halogens these are almost degenerate ($F(^2P)$ is split by 0.05 eV, $I(^2P)$ by 1.0 eV) and are commonly lumped together as the A state. The X state is nearly flat near $R_e$, except for XeCl and XeF which are bound by 0.035 eV and 0.13 eV[38] respectively. The xenon halides are therefore not true exciplexes, in that they have slightly bound ground states due to the greater polarizability and electronegativity of the xenon atom compared with the other rare gases. The A state is always strongly repulsive. The energy ordering of the states above the ground state usually follows their alphabetical ordering, although this is not the case with XeF, where the C state has been found[39,40] to lie $\sim$ 700 $cm^{-1}$ lower than the B state.

All emission from the ionic manifold corresponds to transitions in which an electron jumps from the negative halogen ion to the positive rare gas ion. Allowed radiative transitions are $B \rightarrow X$, $C \rightarrow A$, and $D \rightarrow X$.

The B-X transition is the strongest and is the basis of laser action, with a Franck-Condon factor of order 0.1. Due to the flatness of the X state, the B-X fluorescence has a narrow bandwidth ($\sim$ 2 nm) for a continuum, and at high pressure shows structure due to the vibrational energy level spacing in the B state[35]. The fluorescence from XeCl and XeF shows vibrational and rotational structure expected on a bound-bound transition[38]. Figs. 3.4 and 3.5 show fluorescence spectra produced by e-beam-pumped KrF and XeF mixtures.

D-X emission is similar to B-X, except that it is blue-shifted by an amount equal to the spin-orbit splitting of the rare gas ion. At high pressure, D-X emission is very weak due to collisional quenching of the D state[35,43], and therefore this transition is not promising as

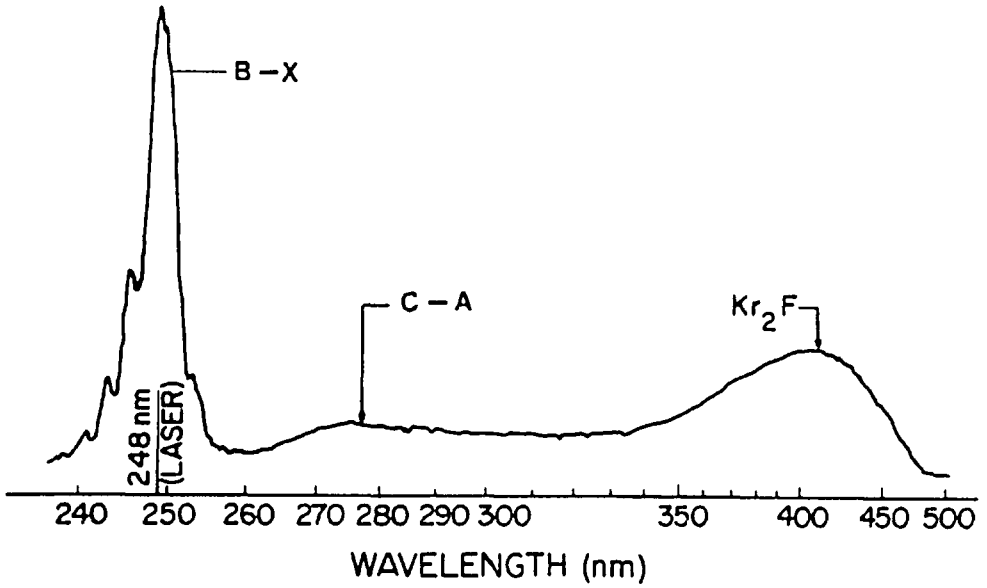


FIGURE 3.4 KrF fluorescence spectrum (from reference *41*).

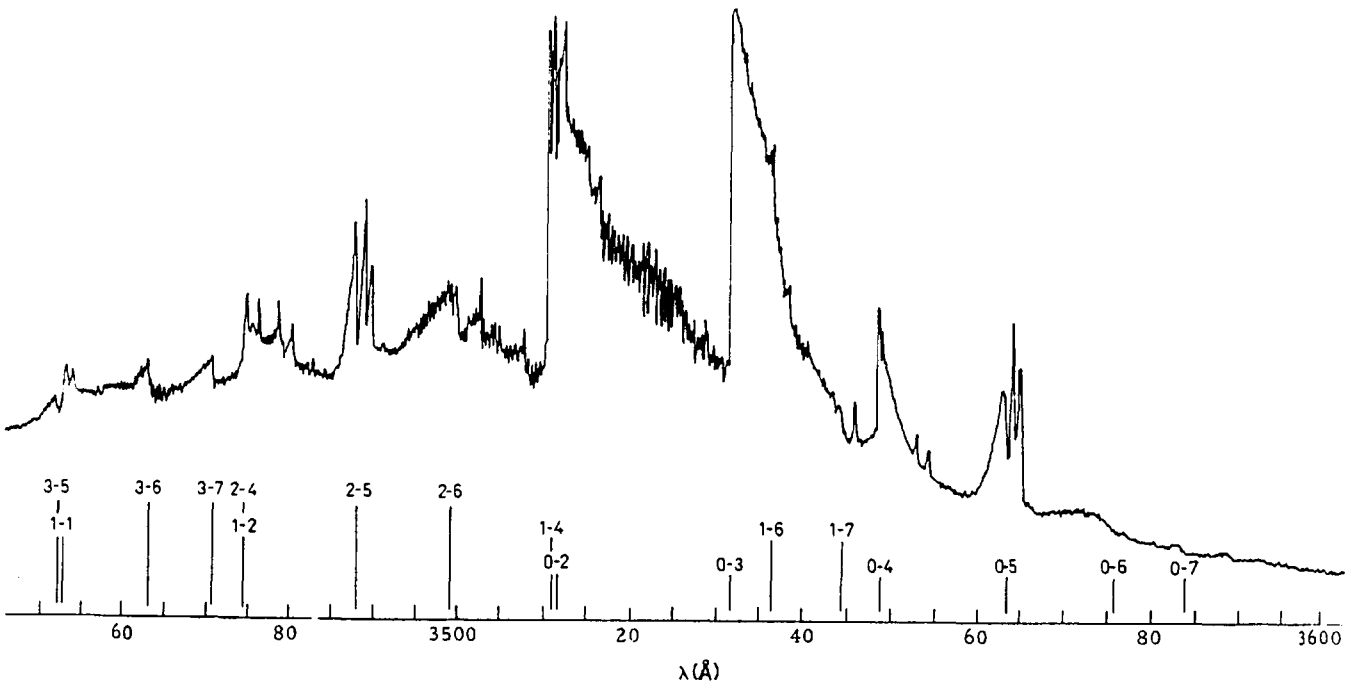


FIGURE 3.5 XeF (B-X) fluorescence spectrum (from reference *38*).

a basis for laser action.

Emission on the C-A bands are very broad ($\sim$ 70 nm in XeF[44]) due to the strongly repulsive nature of the A state, and consequently have much lower stimulated emission cross-sections. Laser oscillation has been achieved, though, in XeF on the C-A transition, by Bischel[45] (by photolytic excitation of XeF ), and Ernst[46] (direct e-beam excitation of Ar, Xe, $NF_3$ mixtures).

Table 3.1 is a compilation of spectroscopic data on the rare gas halides. The B-X transitions generally have stimulated emission cross-sections $\sigma_s$ of $\sim 3 \times 10^{-16}$ cm$^2$ and radiative lifetimes $\tau_s \sim 10$ ns, compared with respective values for the C-A transition of $\sim 5 \times 10^{-18}$ cm$^2$ (for XeF[44]) and $\sim$ 100 ns. Assuming a Gaussian bandshape, the stimulated emission cross-section is given by the expression[47]

$$\sigma_s = \left(\frac{\ell n 2}{\pi}\right)^{\frac{1}{2}} \frac{\lambda^4}{4\pi c \tau_s \Delta\lambda} \qquad 3.2$$

where $\lambda$ = emission wavelength

$\Delta\lambda$ = bandwidth (FWHM)

c = speed of light

and can be calculated if the other variables are known.

Broad band emission at longer wavelengths has been observed at high pressures, from trimers such as $Kr_2F^*$ or $Ar_2F^*$[48,41] (see Fig. 3.4). Their formation is described in Section 3.2.4. Recently gain and laser oscillation have been observed on the blue-green emission continuum of $Xe_2Cl^*$[49,50]. A stimulated emission cross-section of $\sim 8 \times 10^{-18}$ cm$^2$ was derived from the fluorescence spectrum, and gain characteristics were similar to those observed in the XeF (C-A) system.

Not all the B-X transitions are potential laser candidates, and in many rare gas halides fluorescence on this band is not observed at

TABLE 3.1 Spectroscopic data on rare gas halides

| Species (RgX) | λ(B-X) (nm) | τ(B-X) (ns) | $\sigma_s$(B-X) ($10^{-16}cm^2$) | λ(C-A) (nm) | τ(C-A) (ns) | λ($Rg_2X$) (nm) | τ($Rg_2X$) (ns) |
|---|---|---|---|---|---|---|---|
| XeF | 351,353[35,10] | 12[36],19[88], 14[89] | 4.6[96](τ=14) | 470[44] | 98[89],113[36], 93[95] | | |
| XeCl | 308[35,11] | 11[36] | 4.5[35] | 330[36] | 120[36] | 450[48],490[49] | 100[49] |
| XeBr | 282[35,9] | 12[36] | 2.2[72] | 302[36] | 120[36] | | |
| XeI | 253[17] | 12[36],15[121] | 1.4[72] | 263[36] | 110[36] | | |
| KrF | 248[35,11] | 6.7[36],9[90,91], 6.8[92] | 2.4[72](τ=7) | 275[98] | 75[98] | 400[48,70], 415[41] | 181[70],133[93] |
| KrCl | 222[13] | | | | | 325[48] | |
| KrBr | 206[87,16] | | | | | | |
| ArF | 193[12] | 4.2[36] | 2.9[97] | | | 292[48] | 132[93],128[94], 180[99] |
| ArCl | 175[14] | | | | | 246[48] | |
| NeF | 108[15] | 2.6[36] | | | | | |

all. Table 1.1 shows which rare gas halides have been made to lase, together with those that only fluoresce or show no B-X emission. The helium halides have been excluded since in no case do they exhibit B-X fluorescence. The causes of non-lasing or non-emission are predissociation, the presence of covalent excited states lower in energy than the B state, and auto-ionization.

Ideally, the ionic potential crosses all the excited covalent state potentials at large internuclear distances (see Fig. 3.3) so that interaction between them is weak. Predissociation can occur if the covalent potentials cross the ionic curve near its minimum, allowing processes such as

$$RgX^* \rightarrow Rg^* + X$$
$$\rightarrow Rg + X^*$$

to occur, where Rg is a rare gas atom and X is a halogen. If the covalent potentials are relatively flat, these reactions will have slow rate constants, since they are only slightly exothermic and the atoms gain little kinetic energy. In this case, vibrational relaxation to the bottom of the ionic state may be more likely than predissociation at high pressures, allowing population to build up in the upper laser level. This is probably what happens in ArCl, since both laser action[14] and predissociation[51] have been observed, as well as in KrCl and XeBr[52]. Predissociation reduces the efficiency of laser action, since an excited halogen atom X* does not readily react to reform RgX* and may be collisionally quenched or radiate to the ground state in the meantime.

Fig. 3.6 is an approximate potential energy diagram for ArI (adapted from ref. *53*), showing the curve crossings of excited covalent states with the ionic potential minimum. In this case the lowest excited covalent state (correlating with $Ar(^1S) + I^*(6s)$) lies well below the B state potential minimum, and numerous curve crossings

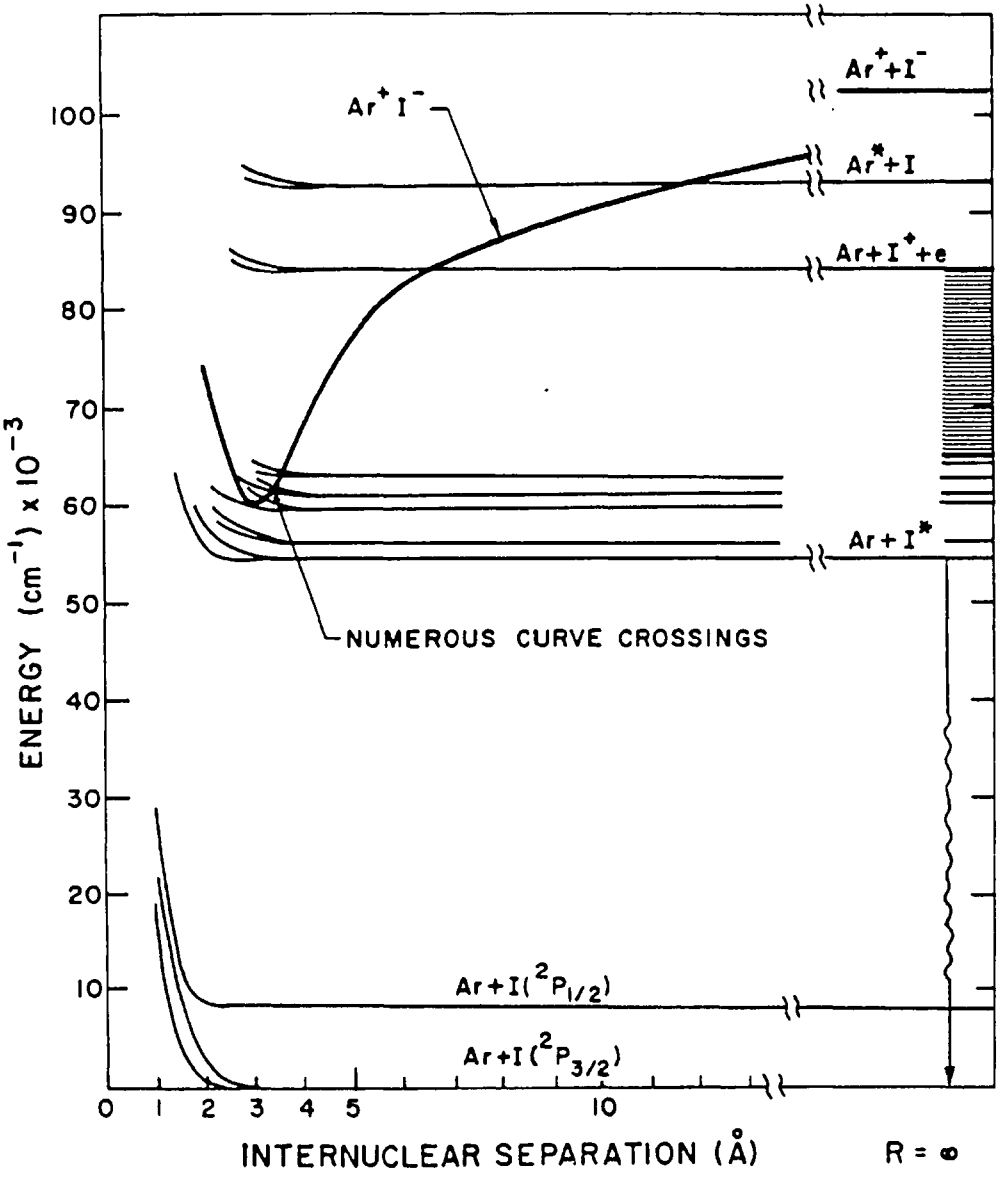


FIGURE 3.6 ArI potential energy diagram.

between the ionic and covalent levels make the formation of excited I* states probable, either from ionic recombination of $Ar^+$ and $I^-$ or reaction of excited Ar* with iodine bearing molecules such as $I_2$. The ionic state is not the lowest upper state in NeCl, NeBr, NeI, ArI, or any of the helium halides. Auto-ionization has also been suggested[52] as a loss mechanism which prevents significant build-up of B state population in these rare gas halides.

Auto-ionization from the ionic state is possible if the ionic potential at infinite inter-nuclear separation is greater than the ionization potential of the halogen, i.e.

$$I.P.(Rg) - E.A.(X) > I.P.(X) \qquad 3.3$$

The rare gas ion acts as a detacher for the negative halogen ion, according to the reaction

$$Rg^+ + X^- \rightarrow Rg + X^+ + e$$

Both auto-ionization, and the existence of excited covalent states lower in energy than the ionic B state, will greatly reduce emission on the B-X transition in the rare gas halides.

## 3.2 Kinetics

### 3.2.1 Introduction

The kinetics of rare gas halide formation depend critically on the method of pumping employed. If electron-beam pumping is used, the dominant formation mechanisms involve ionic species created by the ionizing action of relativistic electrons on rare gas atoms. Discharge-pumped systems are dominated by neutral chemistry between rare gas atoms and other species in excited states. A free electron, with energy less

than the threshold excitation energy E* of the rare gas, cannot excite the rare gas and suffers elastic collisions only, with very little loss of energy. (An exception to this is He, in which elastic losses are important because of its small mass.) As the electron is accelerated in the discharge electric field, it gains energy until E* is reached. It then has a high probability of exciting a rare gas atom in an inelastic collision. This causes the electron energy distribution to drop rapidly near E*, in a non-Maxwellian manner[54].

Typical laser mixtures comprise a buffer rare gas at high (a few bar) partial pressure, a heavier rare gas (1-10%), and a halogen donor ($\sim$ 0.1%). Thus a very large number of reactions are possible. In spite of this substantial progress has been made in understanding and modelling the kinetics of rare gas halides, in particular KrF and XeF. The kinetics of e-beam-pumped KrF lasers using mixtures of Ar, Kr and $F_2$ will be described in Section 3.2.3. KrF is taken as a typical case, but the detailed kinetics of each rare gas halide will differ.

### 3.2.2 Theory of gaseous phase reaction kinetics

Most reactions considered in reaction dynamics are either two body

$$X + Y \xrightarrow{k_a} X' + Y' \qquad (a)$$

or three body

$$X + Y + M \xrightarrow{k_b} XY + M \qquad (b)$$

where X and Y are reacting species and M is a third body. In case (a) the concentration or number density of X ({X}) will show time behaviour given by

$$\frac{d}{dt}\{X\} = -k_a\{X\}\{Y\} \qquad 3.4$$

where $k_a$ is the two body rate constant, usually expressed in units $cm^3\ s^{-1}\ molecule^{-1}$. Similarly, the time behaviour of {X} in case (b) is given by

$$\frac{d}{dt}\{X\} = -k_b\{X\}\{Y\}\{M\} \qquad 3.5$$

where $k_b$ is the three body rate constant ($cm^6\ s^{-1}\ molecule^{-1}$). As the pressure increases, three body reactions will eventually saturate to an effective two body rate. Qualitatively, at high enough pressure a third body, M, always collides with the intermediate short-lived complex XY* before the latter dissociates. The three body process (b) can be divided into two two body steps:

$$X + Y \xrightarrow{k_1} XY^* \qquad (c)$$

$$XY^* + M \xrightarrow{k_2} XY + M \qquad (d)$$

Step (d) is in competition with the unimolecular decomposition of XY*

$$XY^* \xrightarrow{1/\tau_o} X + Y \qquad (e)$$

and therefore increases in likelihood with the lifetime $\tau_o$ of XY*. The intermediate complex is also quenched by collisional dissociation

$$XY^* + M \xrightarrow{k_3} X + Y + M \qquad (f)$$

The three body rate constant $k_b$ can be written

$$k_b = k_1 k_2 \tau \qquad 3.6$$

where $\tau$ is the lifetime of XY* with respect to all losses

$$\frac{1}{\tau} = \frac{1}{\tau_o} + (k_2 + k_3)\{M\} \qquad 3.7$$

At high pressures $(k_2 + k_3)\{M\} \gg \frac{1}{\tau_o}$ and we obtain

$$k_b = k_1 k_2 / (k_2 + k_3)\{M\} \qquad 3.8$$

which is saturated at an effective two body rate

$$k_b = k_1 k_2 / (k_2 + k_3) \qquad 3.9$$

A saturation concentration $\{M\}_{SAT}$ can be defined such that

$$\{M\}_{SAT} = \left[(k_2 + k_3)\tau_o\right]^{-1} \qquad 3.10$$

inversely proportional to the intermediate complex lifetime. Table 3.2 (adapted from ref. *52*) shows rough estimates of saturation pressures for different types of three body reactions. Saturation pressures decrease with species atomicity due to increasing $\tau_o$. Similarly, $\{M\}_{SAT}$ is reduced in ionic complexes relative to neutral species, due to increased $\tau_o$ caused by long range electrical forces. In the rare gas halides, ion-ion reactions such as (*4*) and (*9*) described in Section 3.2.3 are likely to be saturated. For this reason, an effective two body rate is given, which increases with pressure up to the saturation pressure.

A further complication appears at pressures above one bar. As the pressure and number density increase, it becomes increasingly difficult for two ions, attracting at long range, to migrate through the large number of third bodies between them. This causes the two body rate to fall with pressure, after reaching a maximum near one bar. Flannery[55-57] has made detailed calculations of two body rate variation with pressure, for ion-ion recombination reactions important in rare gas halide lasers, over a wide range of pressure.

TABLE 3.2 Saturation pressure of three-body reactions

| Reaction type | Diatomic saturation pressure (bar) | Triatomic saturation pressure (torr) | Polyatomic saturation pressure (torr) |
|---|---|---|---|
| Ion-ion<br>$X^+ + Y^- + M \rightarrow XY^* + M$ | 1-10 | 1-10 | .01-0.1 |
| Ion-neutral<br>$X^+ + Y + M \rightarrow XY^+ + M$ | 10-100 | 10-100 | 0.1-1 |
| Neutral-neutral<br>$X + Y + M \rightarrow XY + M$ | $10^4$-$10^5$ | $10^4$-$10^5$ | $10^2$-$10^3$ |

### 3.2.3 Formation kinetics of e-beam-pumped KrF

In this section, the kinetics of e-beam-pumped KrF lasers are described, taken as an example of a fairly well understood rare gas halide. Many of the reactions described are directly relevant to the performance of ArF lasers as well. Some reference is also made to reactions important in two other efficient lasers, XeCl and XeF. In the present work, mixtures of Ar, Kr and $F_2$ were used in the ratio 500:25:1 at a typical total pressure of 3.7 bar. Rate coefficients k for each reaction are given, where known. Brau[58] has written a comprehensive review of rare gas halide reactions.

Most of the energy of the relativistic primary electrons $e_p$ is absorbed by the majority gas Ar, either by ionization

$$Ar + e_p \rightarrow Ar^+ + e_s + e_p \qquad (1)$$

or excitation ($\sim$ 15%)

$$Ar + e_p \rightarrow Ar^* + e_p \qquad (2)$$

Analogous ionization and excitation of Kr occurs, but is less important due to the small fraction of Kr present. The relatively slow secondary electrons $e_s$ produced by (1) rapidly suffer dissociative attachment to the halogen bearer $F_2$ to create negative halogen ions

$$F_2 + e_s \rightarrow F^- + F \qquad (3)$$

($k \sim 1 \times 10^{-9}$ cm$^3$ s$^{-1}$ [59–62])

The rate constant for (3) is given assuming an average electron energy of a few eV, typical of rare gas halides. Slightly higher attachment rates are expected with $NF_3$, another fluorine bearer[62,63]. Attachment rates with $Cl_2$ are an order of magnitude smaller[64]. The rates are not known accurately because of experimental difficulties, due to the strong

dependence on electron energy near 1 eV. Initially the secondary electrons produced in (1) have energies between zero and 10-20 eV, but due to electron-electron and neutral collisions, they cool very rapidly to an average energy of a few eV. Most of them will not have enough energy to excite the rare gas atoms, so the major fraction of e-beam pumping energy is used to produce $Ar^+$ and $F^-$ ions.

One of the major precursors to KrF* formation is ArF*. ArF* can be created directly by ionic recombination

$$Ar^+ + F^- \ (+ Ar) \rightarrow ArF^* \ (+ Ar) \qquad (4)$$

($k \sim 2 \times 10^{-6}$ cm$^3$ s$^{-1}$ at 3.7 bar [55])

or indirectly by the production of molecular ions

$$Ar^+ + 2Ar \rightarrow Ar_2^+ + Ar \qquad (5)$$

($k = 2 \times 10^{-31}$ cm$^6$ s$^{-1}$ [65])

which react with fluorine ions to create ArF* with a branching ratio of near unity.

$$Ar_2^+ + F^- \ (+ Ar) \rightarrow ArF^* + 2Ar \qquad (6)$$

($k \sim 2 \times 10^{-6}$ cm$^3$ s$^{-1}$ [56])

Reactions (5) and (6) increase in importance, relative to (4), with increasing pressure.

A very fast displacement reaction produces KrF*

$$ArF^* + Kr \rightarrow KrF^* + Ar \qquad (7)$$

($k = 1.5 \times 10^{-9}$ cm$^3$ s$^{-1}$ [66])

Atomic krypton ions are produced by charge exchange with $Ar_2^+$

$$Ar_2^+ + Kr \rightarrow Kr^+ + 2Ar \qquad (8)$$

($k \sim 1 \times 10^{-9}$ cm$^3$ s$^{-1}$ [67])

The krypton ion rapidly recombines with fluorine ions to produce KrF*, in a reaction analogous to (4), with near unity branching ratio

$$Kr^+ + F^- + (Ar) \rightarrow KrF^* (+ Ar) \qquad (9)$$

($k \sim 2.5 \times 10^{-6}$ cm$^3$ s$^{-1}$ at 3.7 bar [57])

The dimer ion $Kr_2^+$ is formed by the following 2-step process:

$$Kr^+ + 2Ar \rightarrow ArKr^+ + Kr + Ar \qquad (10)$$

($k = \sim 1 \times 10^{-31}$ cm$^6$ s$^{-1}$)

$$ArKr^+ + Kr \rightarrow Kr_2^+ + Ar \qquad (11)$$

($k \sim 5 \times 10^{-10}$ cm$^3$ s$^{-1}$ [67])

In a reaction analogous to (6), KrF* is created by ionic recombination of the dimer ion with $F^-$

$$Kr_2^+ + F^- (+ Ar) \rightarrow KrF^* + Kr (+ Ar) \qquad (12)$$

($k \sim 2 \times 10^{-6}$ cm$^{-3}$ s$^{-1}$ at 3.7 bar [57])

KrF* can also be formed directly by ionic recombination of the heteronuclear dimer ion $ArKr^+$

$$ArKr^+ + F^- (+ Ar) \rightarrow KrF^* + 2Ar \qquad (13)$$

($k \sim 2 \times 10^{-6}$ cm$^{-3}$ s$^{-1}$)

Fig. 3.7 is a flow chart showing the ionic formation kinetics of KrF*. Characteristic reaction times are shown for each step, assuming the rate constants given, for the typical laser mixture used in the

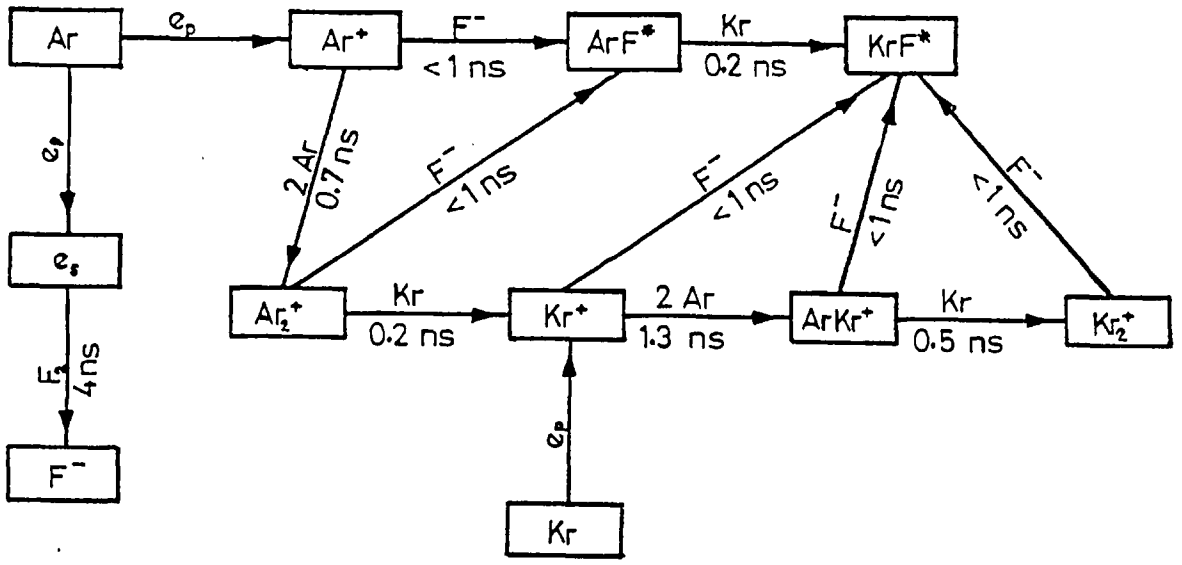


FIGURE 3.7 Ionic formation kinetics of KrF.

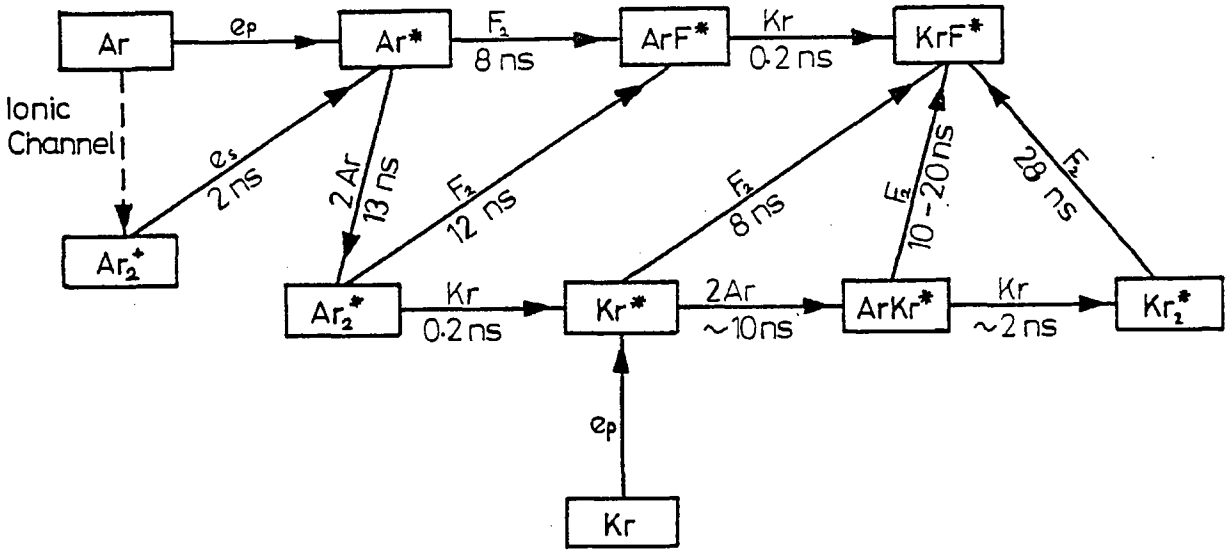


FIGURE 3.8 Neutral formation kinetics of KrF.

present work. As can be seen, KrF* is produced very rapidly through many channels by ionic reaction kinetics.

For completeness, and because they dominate the kinetics of discharge-pumped systems, the most important neutral reactions in e-beam-pumped KrF are described next. In general, the reaction rates are an order of magnitude slower than the ionic ones. Fig. 3.8 is a flow chart showing the neutral formation kinetics scheme in e-beam-pumped KrF.

Excited Ar* is created in reaction (2), and also by dissociative recombination of secondary electron $e_s$ with dimer ions $Ar_2^+$

$$Ar_2^+ + e_s \rightarrow Ar^* + Ar \qquad (14)$$

($k \sim 3 \times 10^{-8}$ cm$^{-3}$ s$^{-1}$ [68])

The analogous reaction with $Kr_2^+$ proceeds with a rate constant of $\sim 1 \times 10^{-7}$ cm$^3$ s$^{-1}$ [68], and at the high ionization rates S attained by short pulse, kiloampere e-beam-pumping, it and (14) constitute a significant source of inefficiency. The total rate of (14) is proportional to $S^2$ since both $\{Ar_2^+\}$ and $\{e_s\}$ are proportional to S. The total rate of the competing dissociative attachment reaction (3) is only proportional to S. Therefore as S increases, a greater proportion of secondary electrons are lost in reaction (14), and the efficiency of $F^-$ production via (3) drops. This in turn reduces the efficiency of ArF* formation via reaction (6).

Excited Ar* reacts with molecular fluorine to produce ArF*

$$Ar^* + F_2 \rightarrow ArF^* + F \qquad (15)$$

($k = 7.5 \times 10^{-10}$ cm$^3$ s$^{-1}$ [43])

or forms argon excimers in the three body reaction

$$Ar^* + 2Ar \rightarrow Ar_2^* + Ar \qquad (16)$$

($k \sim 1 \times 10^{-32}$ cm$^6$ s$^{-1}$)

which can also lead to ArF* production

$$Ar_2^* + F_2 \rightarrow ArF^* + Ar + F \qquad (17)$$

($k = 5 \times 10^{-10}$ cm$^3$ s$^{-1}$ [43]).

The displacement reaction (7) rapidly creates KrF*.

Energy is efficiently transferred to Kr via the reaction

$$Ar_2^* + Kr \rightarrow Kr^* + 2Ar \qquad (18)$$

($k = 1.5 \times 10^{-9}$ cm$^3$ s$^{-1}$ [69])

This type of reaction is fast since a close resonance in energy between the excimer and the excited atom is not required, in contrast to the slow atomic reaction

$$Ar^* + Kr \rightarrow Ar + Kr^* \qquad (19)$$

($k \sim 10^{-12}$-$10^{-11}$ cm$^3$ s$^{-1}$)

where no such necessary resonance exists. In (18), excess energy is removed by dissociation of the argon excimer.

Reaction with $F_2$ produces KrF*.

$$Kr^* + F_2 \rightarrow KrF^* + F \qquad (20)$$

($k = 7.2 \times 10^{-10}$ cm$^3$ s$^{-1}$ [43])

(15) and (20) are both examples of "harpooning" reactions, a term borrowed from analogous reactions observed between ground state alkali atoms and halogen donors, in which the loosely held outer electron of the excited rare gas transfers to the halogen donor at relatively large distances (5-10 Å). The halogen donor polarizes and loses a negatively charged halogen atom, which transfers to the rare gas ion to form an ionically bound rare gas halide. The relatively large rate constant is due

to the long range action of the "harpooning" electron. Branching ratios for rare gas halide production in harpooning reactions between Xe* and $F_2$, $Cl_2$, $Br_2$, $NF_3$, and between Kr* and $F_2$, are unity[43]. (15) has a branching ratio of 0.6.

The krypton excimer $Kr_2$* is produced in the two-step process similar to ionic reactions (10) and (11).

$$Kr^* + 2Ar \rightarrow ArKr^* + Ar \qquad (21)$$

($k \sim 1 \times 10^{-32}$ $cm^6$ $s^{-1}$)

$$ArKr^* + Kr \rightarrow Kr_2^* + Ar \qquad (22)$$

($k \sim 1 \times 10^{-10}$ $cm^3$ $s^{-1}$ [58])

KrF* is produced by reaction of $Kr_2$* or ArKr* with $F_2$

$$ArKr^* + F_2 \rightarrow KrF^* + Ar + F \qquad (23)$$

($k \sim 5 \times 10^{-10}$ $cm^3$ $s^{-1}$)

$$Kr_2^* + F_2 \rightarrow KrF^* + Kr + F \qquad (24)$$

($k = 2.1 \times 10^{-10}$ $cm^3$ $s^{-1}$ [70])

In summary, many different channels exist for the formation of KrF*, with near unity branching ratios. This allows efficient production of KrF*. Similar reaction schemes allow efficient production of XeF* and XeCl*, e.g. recent modelling has shown[111] that dissociative attachment of electrons to HCl in XeCl mixtures follows vibrational excitation of HCl, in the reaction sequence leading to $Cl^-$. The other three rare gas halide lasers - ArCl, KrCl, XeBr - probably have as effective kinetics, but efficiency is impaired by predissociation.

3.2.4 Quenching losses and laser energy extraction

It is to be expected that very fast formation kinetics imply fast loss processes as well. Laser efficiency will be reduced by competing reactions which remove important precursors to KrF*, or by collisional quenching of KrF* before it is stimulated down to the ground state. The most important losses are due to collisional quenching of ArF* and KrF*, whose quenching rates determine to a large extent the optimum gas mixtures. Table 3.3 is a summary of important quenching reactions in e-beam-pumped KrF, with their rate constants and characteristic reaction times in a typical mixture (3.7 bar, Ar:Kr:$F_2$ = 500:25:1). The most important losses are due to quenching by the halogen donor, which occurs at gas kinetic rates, and three-body collisions with rare gas atoms to form triatomic species such as $Kr_2F^*$ and $Ar_2F^*$ or ArKrF*. The latter species undergoes a rapid exchange reaction to produce $Kr_2F^*$

$$ArKrF^* + Kr \rightarrow Kr_2F^* + Ar \qquad (38)$$

ArKrF* has not been directly observed, but has been postulated to account for increased quenching of KrF* fluorescence and formation of $Kr_2F^*$ at high Ar pressure[71]. The importance of reactions (34),(35) is revealed by the observation of $Kr_2F^*$ fluorescence in a broad band ($\sim$ 60 nm) centred at 415 nm[41] (see Fig. 3.4).

At high e-beam pump powers, as in the present work, quenching of ArF* and KrF* (reactions (30) and (31)) by secondary electrons will be major loss processes.

The quenching reactions listed result in a total quenching lifetime $\tau_Q$ for KrF* of only 0.25 ns, much shorter than the spontaneous radiative decay time and therefore resulting in low fluorescence efficiency. Under lasing conditions, however, stimulated emission competes with quenching to extract the stored energy. The radiative lifetime $\tau$ due to stimulated emission is given by the expression

TABLE 3.3 Quenching reactions in KrF gas mixture

| | Reaction | Rate constant ($cm^3 s^{-1}$ or $cm^6 s^{-1}$) | Characteristic reaction time (ns) | Ref. |
|---|---|---|---|---|
| (25) | $ArF^* + F_2 \rightarrow$ products | $1.8 \times 10^{-9}$ | 3.2 | *66* |
| (26) | $KrF^* + F_2 \rightarrow$ products | $(5\text{-}6) \times 10^{-9}$ | $\sim$ 1 | *70,92,41* |
| (27) | $KrF^* + Ar \rightarrow$ products | $1.8 \times 10^{-12}$ | 6.4 | |
| (28) | $ArF^* + Ar \rightarrow$ products | $8.6 \times 10^{-12}$ | 1.3 | *66* |
| (29) | $KrF^* + Kr \rightarrow$ products | $9 \times 10^{-12}$ | 26 | *92* |
| (30) | $KrF^* + e_s \rightarrow$ products | $\sim 2 \times 10^{-7}$ | $\sim$ 0.5 | *74* |
| (31) | $ArF^* + e_s \rightarrow$ products | $\sim 3 \times 10^{-7}$ | $\sim$ 0.3 | *74* |
| (32) | $ArF^* + 2Ar \rightarrow Ar_2F^* + Ar$ | $3.8 \times 10^{-31}$ | 0.3 | *66* |
| (33) | $KrF^* + 2Kr \rightarrow Kr_2F^* + Kr$ | $(0.3\text{-}1) \times 10^{-30}$ | $\sim$ 80 | *70,92,41,100* |
| (34) | $KrF^* + 2Ar \quad ArKrF^* + Ar$ | $(7\text{-}11) \times 10^{-32}$ | $\sim$ 1.5 | *92,100,71* |
| (35) | $KrF^* + Ar + Kr \quad Kr_2F^* + Ar$ | $6.2 \times 10^{-31}$ | 4.3 | *71* |
| (36) | $Ar_2F^* + F_2 \rightarrow$ products | $2.1 \times 10^{-10}$ | 28 | *58* |
| (37) | $Kr_2F^* + F_2 \rightarrow$ products | $2.5 \times 10^{-10}$ | 24 | *58* |

Total quenching lifetime of KrF* = 0.25 ns

" " " " ArF* = 0.13 ns

$$\tau = h\upsilon/\sigma_s I \qquad 3.11$$

where I is the intensity of laser light. For a KrF laser with an output of 10 MW $cm^{-2}$, $\tau \approx 0.4$ ns, implying that in the present work (to which the above figures pertain), $\sim$ 40% of KrF* contributes to laser action.

The efficiency of energy extraction is reduced further by incomplete coupling between the states of the upper ionic manifold and by the finite vibrational relaxation time in the B state. The KrF* population is distributed between the B, C, and D states, but only the B state can contribute directly to laser action.

The efficiency of energy extraction from the upper manifold will depend on the relative populations in each state, and coupling rates between them, either by collisions with "hot" electrons or "cold" atoms and molecules, in reactions such as

$$KrF(B) + Ar \rightleftharpoons KrF(c) + Ar \qquad (39)$$

or

$$KrF(B) + e_s \rightleftharpoons KrF(D) + e_s \qquad (40)$$

Furthermore, the population in each state is formed in vibrationally excited states, which must relax, through V-V,T collisions with atoms or molecules, down to the lowest vibrational level before it can contribute to laser action. The thermal population in the upper levels must also be considered, since the vibrational energy level spacing is estimated to be 320 $cm^{-1}$ [72] ($\sim$ $^3/_2$ kT at room temperature) in the B state. If vibrational relaxation is relatively slow, the B state population will be quenched before it reaches the upper laser level, and once lasing begins, the thermal population in vibrationally excited states will not feed efficiently into the depleted bottom level. Pummer *et al.*[73] have

measured coupling times and the vibrational relaxation time in discharge-pumped KrF lasers operating at 2 bar in He, Kr, $F_2$ mixtures, by looking at sidelight fluorescence from the B, C and D states in the presence or absence of laser action. At that pressure the measured coupling time $\tau_{B-C}$ between the B and C states was $\lesssim$ 1 ns, so they were in thermal equilibrium, and the times $\tau_{B-D}$, $\tau_{C-D}$ were > 20 ns, so population formed in state D was not available for laser action. The D state population generated directly by pumping was $\sim$ 15% of the B state population. Vibrational relaxation within the B state was found to be incomplete, and the estimated relaxation time $\tau_v$ was 4 ± 2 ns. Jacob[74] and co-workers estimate a $\tau_v$ time of $\sim$ 0.3 ns in an e-beam-pumped (11.5 A $cm^{-2}$) KrF laser operated in an Ar, Kr, $F_2$ mixture at 1.5 bar pressure. The faster $\tau_v$ in the e-beam-pumped system may be due to the Ar buffer. Rokni[42] found that vibrational relaxation in the B state of XeF was faster when Ar-rich mixtures were used, instead of Ne. This is attributed to the formation of intermediate ArXeF* in Ar mixtures, while in Ne mixtures NeXeF* is not readily formed due to the relatively weak binding of $NeXe^+$.

The finite rates of vibrational relaxation and B-C coupling will lead to significant quenching losses, especially at high pumping levels (> $10^6$ W $cm^{-3}$) or pressures which reduce the quenching lifetime $\tau_Q$ of KrF* to subnanosecond levels. The inefficiency due to finite vibrational relaxation can be estimated using the factor[42]

$$\eta_v = \frac{\theta\tau_Q/\tau_v}{1+\theta\tau_Q/\tau_v} \qquad 3.12$$

applicable to steady-state conditions, where $\theta$ is the fraction of population in the lowest vibrational level in thermal equilibrium. Rotational relaxation is assumed to be extremely rapid compared to $\tau_Q$[75].

In the present work, assuming that vibrational relaxation is mainly due to collisions with Ar, estimated values are

$\tau_v \sim 0.1$ ns

$\tau_Q \sim 0.25$ ns

$\theta \sim 0.75$

$\eta_v = 66\%$

The total efficiency of energy extraction $\eta_{ext}$ can be expressed in the form

$$\eta_{ext} = \eta \, \eta_v \, \eta_L \qquad 3.13$$

where $\eta$ is the efficiency due to collisional quenching and spontaneous radiative decay of the upper laser level and non-saturable absorption losses in the medium, assuming homogeneous broadening and a repulsive lower level, and $\eta_L$ is due to the finite lifetime of the lower laser level. $\eta$ has been calculated[42] using Rigrod's theory[76] for energy extraction from a laser cavity, modified to include distributed losses in the medium, i.e. the non-saturated absorption of laser radiation.

Photo-absorption of the laser wavelength is a significant loss process in the rare gas halides. The relatively high (for an excimer) stimulated emission cross-sections overcome numerous photo-absorption processes and allow successful laser action. The largest absorption cross-sections are an order of magnitude smaller than the stimulated emission cross-section, which allows the gain to saturate at lower intensities than the absorption. The non-saturable absorption reduces the extraction efficiency as the gain length is increased, thus limiting the practical length of a laser to one or two metres[42,74]. In long-pulse (100 ns - 1 μsec) e-beam-pumped systems, typical extraction efficiencies are < 50%, and formation efficiencies of KrF* are $\sim 20\%$[74], resulting in an intrinsic

laser efficiency of $\sim$ 10%.

Listed below are potentially important photo-absorption processes, together with their cross-sections ($cm^2$) in the KrF laser:

Photodissociation of the halogen bearing species,

$$F_2 + h\upsilon \rightarrow 2F \qquad (41)$$

($\sigma = 1.5 \times 10^{-20}$ [77])

and of the rare gas dimer ions,

$$Ar_2^+ + h\upsilon \rightarrow Ar + Ar^+ \qquad (42)$$

($\sigma = 1 \times 10^{-17}$ [78,79])

$$Kr_2^+ + h\upsilon \rightarrow Kr + Kr^+ \qquad (43)$$

($\sigma = 3.1 \times 10^{-19}$ [78])

Photo-ionization of the negative halogen ion,

$$F^- + h\upsilon \rightarrow F + e^- \qquad (44)$$

($\sigma = 5.5 \times 10^{-18}$ [80])

and of excited rare gas atoms and excimers,

$$Ar^*(4p) + h\upsilon \rightarrow Ar^+ + e^- \qquad (45)$$

($\sigma = 4.3 \times 10^{-18}$ [81])

$$Kr^*(5p) + h\upsilon \rightarrow Kr^+ + e^- \qquad (46)$$

($\sigma = 4.5 \times 10^{-18}$ [81])

$$Ar_2^* + h\upsilon \rightarrow Ar_2^+ + e^- \qquad (47)$$

$$Kr_2^* + h\upsilon \rightarrow Kr_2^+ + e^- \qquad (48)$$

($\sigma = 3 \times 10^{-18}$ [58])

The triatomic species $Ar_2F^*$ and $Kr_2F^*$ are important absorbers. They are essentially ionic complexes of the form $Kr_2^+F^-$ and are expected to have cross-sections similar to $Ar_2^+$ and $Kr_2^+$ (see *42*).

In typical e-beam-pumped KrF mixtures, the dominant absorbing species are $Kr_2F^*$, $F_2$ and $F^-$. In a mixture of Ar, Kr, $F_2$ (93.7%, 6%, 0.3%) at 3 bar total pressure, pumped at 6 A $cm^{-2}$, total measured absorption[42,82] due to transient species was $4.4 \times 10^{-3}$ $cm^{-1}$ (27% due to $F^-$, 55% due to $Kr_2F^*$). Background absorption due to $F_2$ was $3 \times 10^{-3}$ $cm^{-1}$. The total gain was $\sim$ 10 times the transient absorption.

The performance of rare gas halide lasers can be considerably enhanced by a mixture which minimizes photo-absorption. An example is the XeCl laser, which was initially operated in Ar, Xe, $Cl_2$ mixtures[11]. However, the high absorption cross-sections at 308 nm ($\sigma_{(Cl_2)} = 1.7 \times 10^{-19}$ $cm^2$ [83], $\sigma_{(Ar_2^+)} = 4 \times 10^{-17}$ $cm^2$ [78]) limited the efficiency. Greatly improved output is obtained using Ne, Xe, HCl mixtures[84] ($\sigma_{(Ne_2^+)} = 8 \times 10^{-18}$ $cm^2$ [78]) which have lower absorption cross-sections. Improvement is also due to the fact that $Xe_2^+$ formation is slower in Ne-rich mixtures, because the intermediate compound $NeXe^+$, unlike $ArXe^+$, is unbound (see *85*). Absorption by $Xe_2^+$ is very important, both in XeCl, and XeF, also improved by use of a Ne diluent ($\sigma_{(Xe_2^+)} = 1.6 \times 10^{-17}$ $cm^2$ at 308 nm, = $4.8 \times 10^{-17}$ $cm^2$ at 352 nm[78]).

In the case of KrF, replacement of the absorber $F_2$ by $NF_3$, which does not absorb at 248 nm, does not improve the performance. There are two reasons for this: (1) the branching ratio of Kr* with $NF_3$ is only 0.57[43] and (2) the krypton ion can transfer to $NF_3$ via the loss process[86]

$$Kr^+ + NF_3 \rightarrow Kr + NF_3^+ \qquad (48)$$

($k = 2 \times 10^{-10}$ $cm^3$ $s^{-1}$)

Performance of the XeF laser does improve with use of $NF_3$, since the

branching ratio of Xe* with $NF_3$ is unity and $Xe^+$ does not have enough energy to ionize $NF_3$.

The intra-cavity flux in a laser can perturb the kinetics of rare gas halide formation, if intensities of more than a few MW $cm^{-2}$ are present. In particular, the photo-detachment process (44) will compete with electron attachment (3) and decrease the efficiency of $F^-$ formation. Note that none of the processes discussed involve atomic fluorine in rare gas halide formation. Therefore if the halogen bearer is "burned up", rare gas halide formation will cease, since the three body recombination rate of atomic fluorine is of the order of $10^{-32}$ $cm^6$ $s^{-1}$, and in typical laser mixtures corresponds to a characteristic recombination time of the order of 10 μsec, much longer than pump pulse lengths achieved to date.

Finally, self-absorption to higher lying levels of the rare gas halide may reduce the effective gain cross-section. Self-absorption will be to a state correlating with an excited rare gas, in a transition which involves an electron transferring from the halogen ion to the rare gas ion. Self-absorption to a state correlating with an excited halogen atom is very unlikely, since this corresponds to a 2-electron transition in which one electron jumps from the halogen ion to the rare gas ion, and a second electron is raised to an excited halogen level. Not all the rare gas halides produce B→X radiation of sufficient energy to reach many excited covalent states. The rare gas fluorides are the most tightly bound in the B state and therefore emit the longest wavelength B→X radiation. XeF radiation will not raise a molecule in the B state to even the lowest state correlating to excited xenon, and in KrF, only states correlating to the lowest excited state of Kr can be reached (see Fig. 3.3). Self-absorption in KrF is not significant, as shown by the close agreement between measured and calculated values of the stimulated emission cross-section[82]. In contrast, XeBr has many covalent states within

the required energy range, and self-absorption may be important in this species as well as in other rare gas heavy halides.

## 3.3 Conclusion

Using krypton fluoride as a specific example, we have seen how efficient laser action in electron-beam-pumped rare gas halides is possible. The formation kinetics are very fast, many important reactions have near unity branching ratios, and the high stimulated emission cross-section allows the gain to saturate and possibly dominate quenching losses. The detailed kinetics differ in each case, but the spectroscopic structure is such that energy is efficiently funnelled into the upper laser level.

The formation kinetics of KrF pumped at moderate e-beam densities ((1-5) x $10^5$ W $cm^{-3}$) are well understood and accurate predictions of laser output can be made in this regime[74,124]. A large body of literature exists on the kinetics of and energy extraction from the other rare gas halides, notably XeF and XeCl, and similar predictive models are being developed. At very high pump powers (> $10^6$ W $cm^{-3}$) uncertainties exist due to electron quenching of the upper state, and the finite lifetime of the ground state, particularly important in XeF and XeCl.

Because efficiency is strongly dependent on stimulated emission dominating collisional quenching, losses will be severe during the laser build-up time. For this reason, long pulse (0.5-1 μsec) systems will be more efficient than short pulse (10-50 ns) systems in which the build-up time is a large fraction of the total pulse length. The high electron densities ($\sim 10^{16}$ $cm^{-3}$) associated with short pulse systems are also responsible for very fast quenching processes and further decrease the efficiency of laser output.

CHAPTER 4

# TRANSVERSELY-PUMPED KrF LASER

## 4.1 Introduction

In this chapter the design and some characteristics of a transversely-pumped KrF laser are described. Information gained from this work was useful in the design of a more efficient co-axially pumped laser diode. It is related here as background and as an opportunity to describe some useful techniques.

Transverse pumping is a flexible method of excitation. Large volume cells can be easily constructed for the purpose of achieving efficient e-beam energy deposition in relatively low pressure (2-4 bar) gases. Side fluorescence is also easily observed using transverse geometry.

## 4.2 Laser Cell and E-Beam Diode Construction

The laser cell and diode are shown approximately to scale in Fig. 4.1.

The cell consisted of a rectangular aluminium alloy box (inner dimensions 9.2 cm x 10.3 cm x 17.0 cm) mounted on a circular dural baseplate containing an oblong e-beam window (6 cm x 14 cm). Vacuum and pressure sealing was provided by Viton "O" rings coated with fluorocarbon vacuum grease. The maximum active volume of the laser, defined by the 1 cm thick, 6.3 cm diameter plane parallel quartz windows, was 530 $cm^3$. Ports in the cell served for the admittance or exhaust of gas mixtures, and for vacuum pumping.

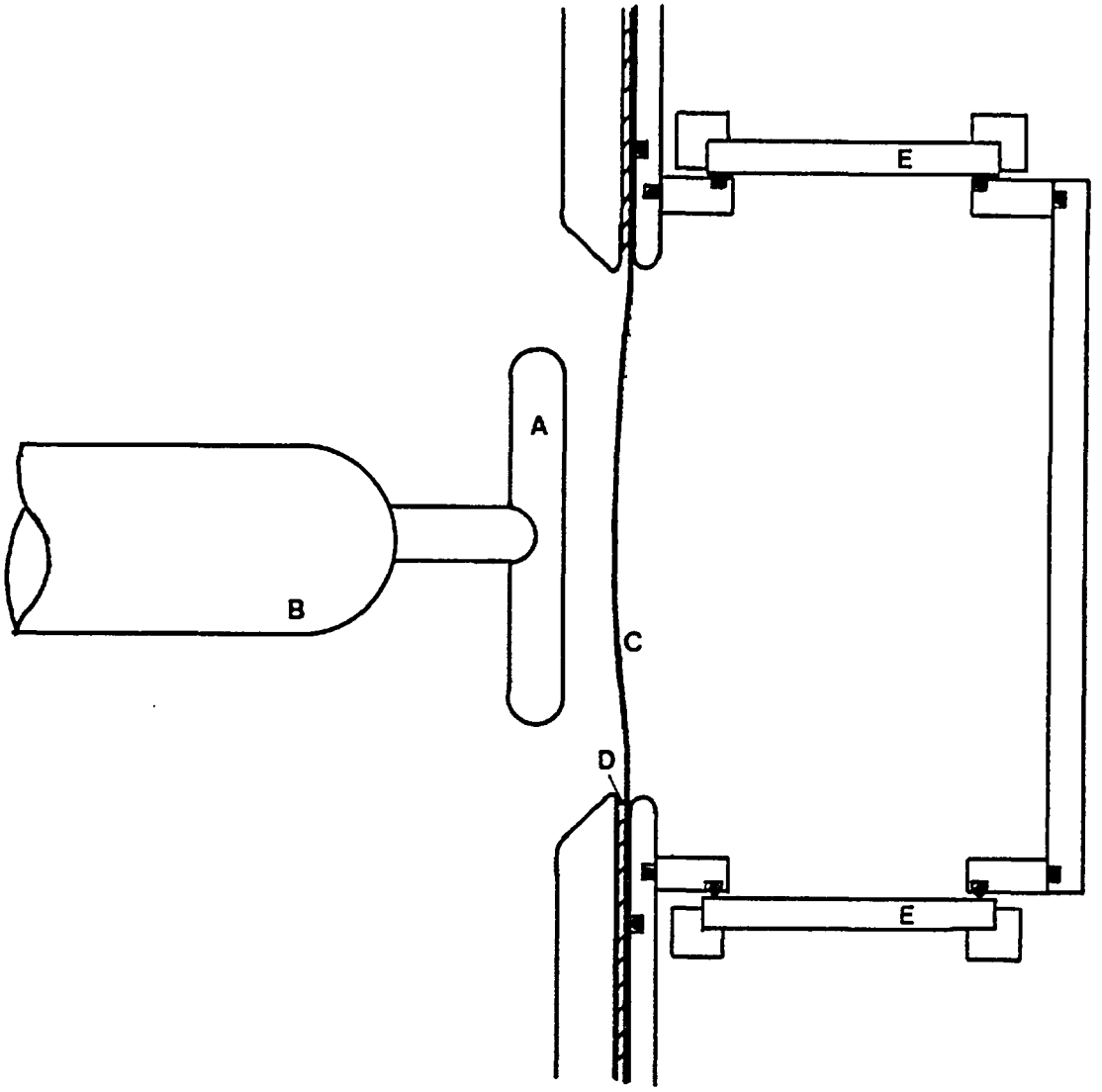


A - Graphite cathode
B - Cathode shank
C - Anode foil
D - Araldite
E - Quartz windows

FIGURE 4.1 Transverse laser diode construction.

The cathode consisted of a graphite blade 10 cm long, tip radius $\sim$ 1 mm, mounted on a cylindrical dural stem which screwed into the end of the vacuum diode chamber. Field grading rings provided uniform gradation of field strength within the diode.

The 50 μm titanium anode foil was affixed with Araldite to the end of the diode vacuum chamber, vacuum sealing the 5 cm x 13 cm e-beam window, and was unsupported over the stated dimensions. The laser cell assembly was mounted over the anode foil, so as to match up the two e-beam windows. The laser cell and anode foil were tested successfully at full e-beam power with the cell pressurized with argon to 4.4 bar.

Cathode-anode separation was 1.2 cm, in a chamber kept at $10^{-4}$ torr pressure. Peak current, measured with a pre-calibrated B-loop monitor, was 32 kA in a 35 ns (FWHM) pulse (see Fig. 2.16), corresponding to a peak current density at the anode of $\sim$ 900 A $cm^{-2}$. Peak voltage was approximately 500 kV in a 30 ns pulse, resulting in a total e-beam energy of $\sim$ 350 J.

In use, a foil survived about 90 shots. Non-catastrophic failure was due to the formation of pinhole leaks, caused by sputtering of carbon from the cathode onto the foil.

The diode chamber required regular cleaning to remove carbon deposited onto all surfaces. After cleaning, the cathode stem, field grading rings and electrical insulation were coated with a thin layer of diffusion pump oil, to help prevent spurious emission.

## 4.3 Gas Handling

Typical gas mixtures were Ar:Kr:$F_2$ in the ratio 500:25:1, respectively, at a total pressure of 3.9 bar. Argon was B.O.C. high-purity grade (99.999%), krypton was B.O.C. research grade (99.9997%) and fluorine was Air Products commercial purity (99%). The major

impurity in the fluorine was hydrogen fluoride (HF). In some experiments, nitrogen trifluoride ($NF_3$), 98% pure, was used as the fluorine donor (Ozark Mahonning, Oklahoma).

Fig. 4.2 is a schematic diagram of the (largely) stainless steel gas handling system (G.H.S.) attached to the laser cell. Gas mixtures were made in a 20 litre stainless steel mixing cylinder, in sufficient quantity for about 15 fills of the laser cell.

Before use, the mixing cylinder was vacuum baked, and all parts of the G.H.S. were evacuated to $\sim 10^{-2}$ torr with a rotary-pump-backed, cold-trapped oil diffusion pump. All parts of the G.H.S. likely to be in contact with fluorine were pre-passivated. Fluorine passivation is necessary to prevent fluorine, typically at a few torr partial pressure, from reacting with the walls of the G.H.S. and laser cell and removing itself from the laser gas mixture. It is carried out by admitting relatively high pressure fluorine to the G.H.S. and laser cell. A metal fluoride layer forms on the side-walls and prevents further reaction, and at the same time the fluorine reacts with and consumes any traces of organic dirt in the system.

Fluorine is very toxic and is a very strong oxidising agent, requiring great care in its use. High pressure fluorine was handled separately in a special room for the purpose, containing a proper ventilation system in the event of a leak. Great care was taken to avoid the possibility of a fluorine fire, by cleaning all components scrupulously with acetone, removing as much organic material as possible.

The mixing cylinder was passivated by slowly pressurizing it with a 1:1 argon:fluorine mix to one bar total pressure, and leaving it to stand for one hour. The rest of the G.H.S. and the laser cell were passivated with 100-120 torr pure fluorine left overnight. The laser cell was frequently "down" and was re-passivated each time.

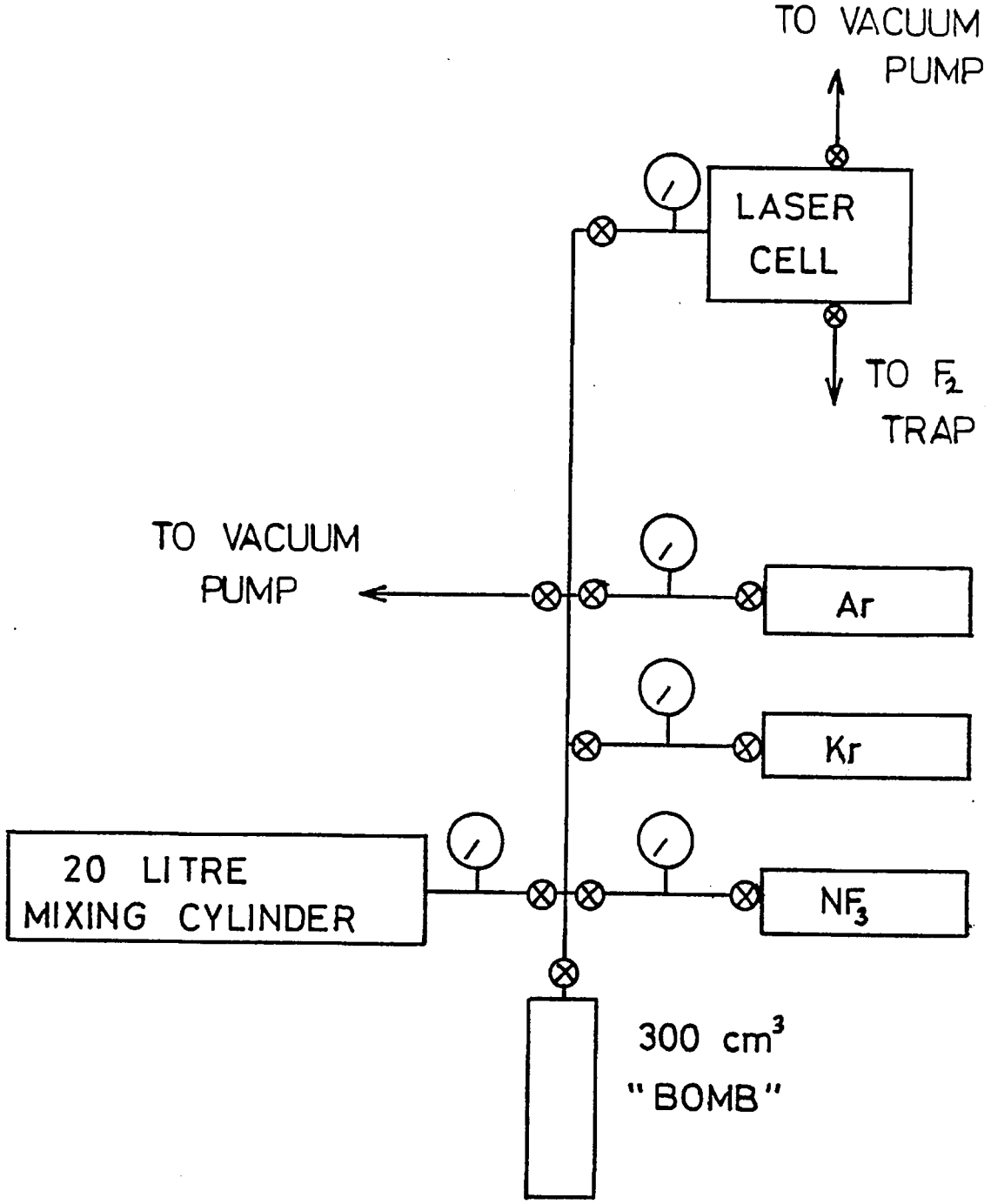


FIGURE 4.2 Schematic diagram of gas handling system.

A 300 $cm^3$ stainless steel cylinder or "bomb" was used to transfer high pressure fluorine (up to 2 bar) to the G.H.S. To make up a laser mixture, the bomb was first cooled to 78°K with liquid nitrogen, before allowing fluorine into the evacuated mixing cylinder with a concomitant increase in volume by a factor of 68. The cold temperature removed the HF impurity from the fluorine, preventing attack of the quartz windows of the laser cell. The vapour pressure of fluorine at 78°K is 250 torr, compared with an HF vapour pressure of $\sim 10^{-3}$ torr at the same temperature, and a required $F_2$ partial pressure of $\sim$ 20 torr in the mixing cylinder (see Fig. 5.18).

The mixing cylinder was then filled with krypton and argon, in that order, bringing the total pressure up to 10 bar. After allowing a minimum of one hour for the gases to mix thoroughly, the mixture could be admitted to the laser cell as required.

Used mixtures were exhaused through a fluorine trap, consisting of a glass bottle containing concentrated potassium hydroxide solution, and purged with argon. Trace amounts of fluorine were removed by the rotary pumps, with no ill effects.

Nitrogen trifluoride was used in an experiment measuring gain in the laser medium. $NF_3$ is far easier than $F_2$ to handle, due to its much lower reactivity and hundred times lower toxicity (maximum allowed working level = 10 ppm, compared with 0.1 ppm for $F_2$). In safety terms, the only disadvantage of $NF_3$ is its relative odourlessness, which means leaks may go undetected. Fluorine has a very distinctive smell, detectable at concentrations well below the recommended safety limit, making leaks easy to detect. Fluorine was preferred in this work due to the greater gain in a KrF laser.

## 4.4 KrF Lasing and Fluorescence

Maximum laser energy was 100 mJ at 2484 Å, operating in an Ar:Kr:$F_2$ mixture (= 500:25:1) at 3.9 bar total pressure. The 26 cm long laser cavity consisted of a 2.5 cm diameter, spherical 2 m radius of curvature, dielectric 99% reflector, and a 60% reflectivity plane dielectric output mirror, 3.8 cm in diameter. The plane parallel quartz windows were aligned with the cavity to minimize losses. Maximum laser energy was produced when the laser axis was aligned as close as possible (3 cm) to the foil, and cavity length was minimized, thus allowing the greatest number of round trips. Energy was measured with a Laser Instrumentation Ltd Model 142 L.R. calorimeter, and corresponded to a specific laser energy storage density of 1.7 J litre$^{-1}$ in the active medium. Three factors were responsible for the rather low maximum energy. Firstly, much of the pump energy was dissipated close to the foil in a region outside the laser cavity; secondly, the active volume using the 2.5 cm diameter back reflector was only 15% of the active volume defined by the laser cell windows; and thirdly, the excitation was highly non-uniform.

The time behaviour of lasing at threshold and fluorescence is shown in Fig. 4.3, recorded with an ITT4115 solar blind fast photodiode and a Tektronix 519 oscilloscope. For threshold lasing, the cavity consisted of a 95% reflectivity plane dielectric mirror (3.8 cm diameter) and a quartz window output coupler. The 14 ns pulse (FWHM) delivered 0.5 mJ with a delay of 25 ns with respect to the beginning of the e-beam pump pulse. Pulse width and delay did not change appreciably at high laser energies (see Section 5.6).

Laser energy increased with mixture pressure, up to the safe working pressure of the laser cell, as shown in Fig. 4.4. Fresh mixture was used at each pressure tested, because of the drop in KrF energy with shot number, shown in Fig. 4.5 for a single fill.

FIGURE 4.3 Fluorescence (top) and threshold lasing (bottom) in KrF, synchronized, 10 ns/div.

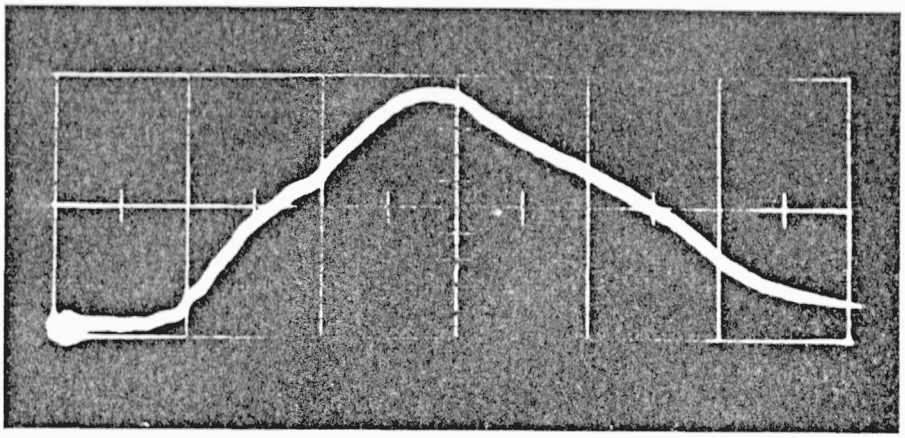

→10 NS←

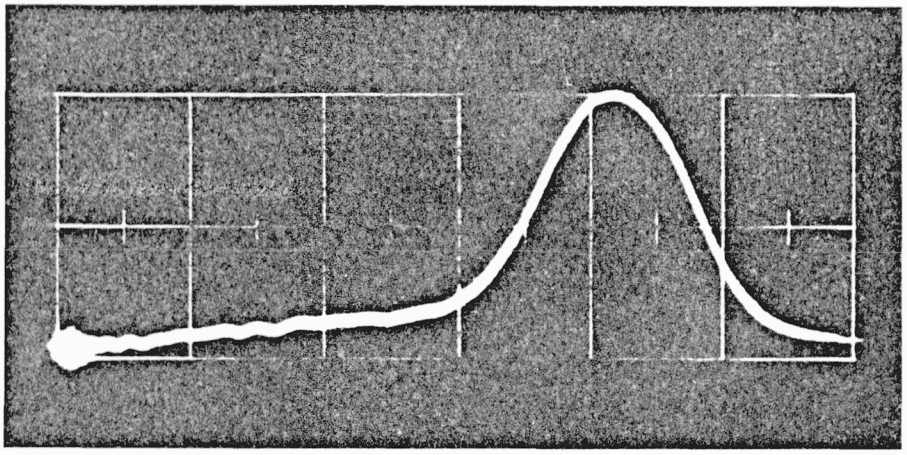

→10 NS←

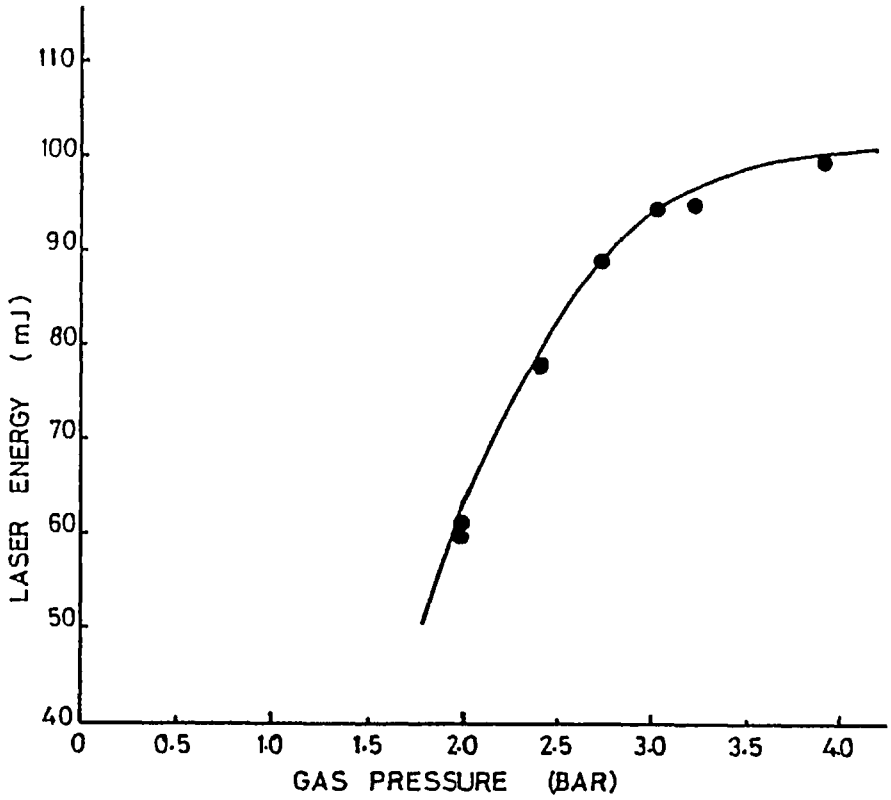


FIGURE 4.4 KrF laser energy versus pressure.

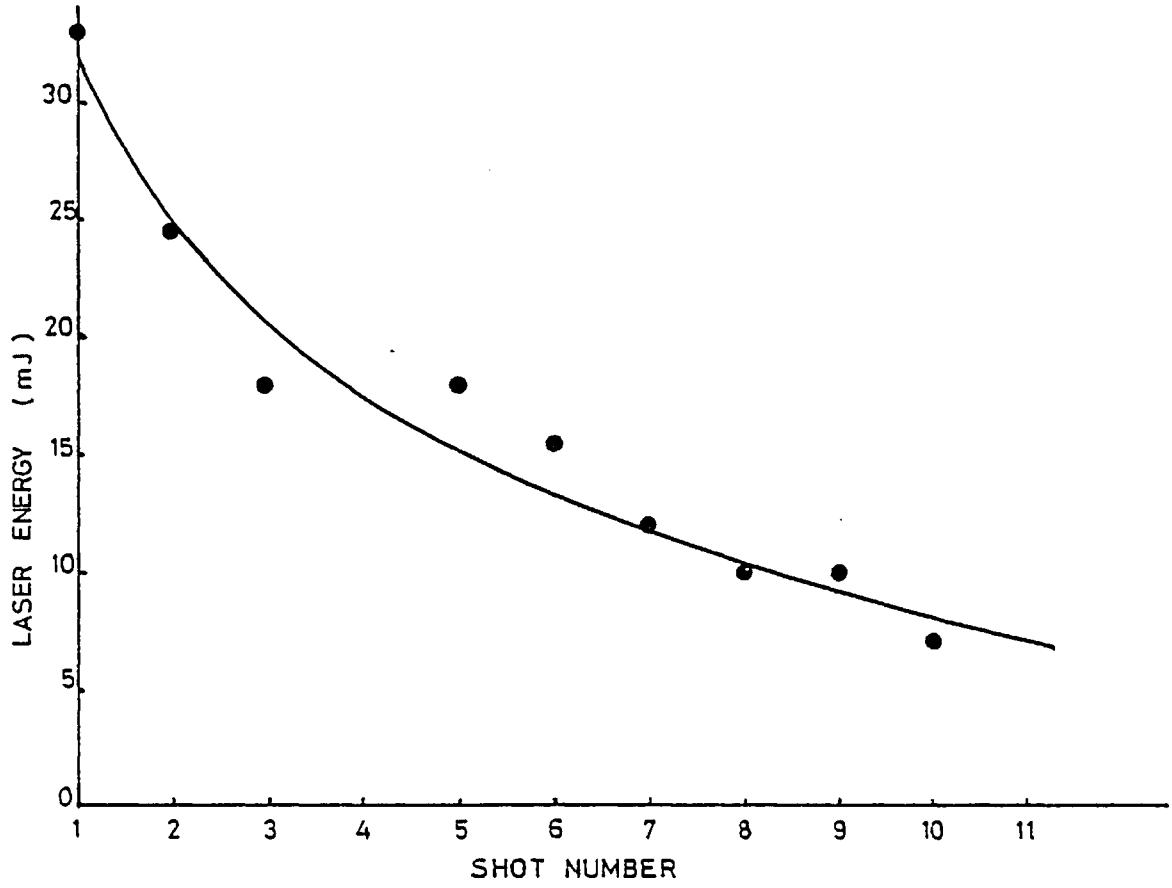


FIGURE 4.5 KrF laser energy versus shot number.

Fluorescence and laser spectra, taken with a Hilger and Watts 0.6 m Czerny-Turner grating spectrograph in first order, calibrated with a low pressure mercury lamp, are shown in Fig. 4.6 and Fig. 4.7. Strong laser emission was recorded at 2484 Å, and a weak secondary peak was seen at 2490 Å. Laser bandwidth was 3 Å, based on the nominal response of the Ilford FP3 plate. The fluorescence showed strong emission centred at 2484 Å, as well as much weaker emission at shorter wavelengths from transitions originating from higher vibrational levels in the KrF(B) upper state. Fluorescence bandwidth was $\sim$ 2 nm.

Total beam spread was of the order 20 mrad, estimated by observation of the fluorescence pattern on a white card target.

## 4.5 Gain Measurement

Gain in the laser medium was measured in both $F_2$ and $NF_3$ mixtures. The $F_2$ mixture was as stated earlier, and the $NF_3$ mixture was Ar:Kr:NF (= 1300:130:1, as used by Bhaumik[19]), at a total pressure of 3.7 bar. Due to its smaller gain coefficient, laser action was not achieved using $NF_3$ mixtures.

Peak gain was estimated by comparing the signals due to amplified spontaneous emission, detected by a fast photodiode P, in the presence ($S_2$) or otherwise ($S_1$) of a maximum back reflector M. Fig. 4.8 is a schematic of the experimental arrangement. The output from the laser cell passed through a 0.6 m monochromator set at 2484 Å (slit width = 1.5 mm) before being detected by P. The back plane, dielectric mirror was 3.8 cm in diameter. The laser cell windows were misaligned $2^{\circ}$ with respect to the cell axis to prevent extraneous reflection into the detection system. A fast, solar blind photodiode B monitored sidelight.

FIGURE 4.6 KrF fluorescence (top) and laser (bottom) spectra. Wavelength increases to right.

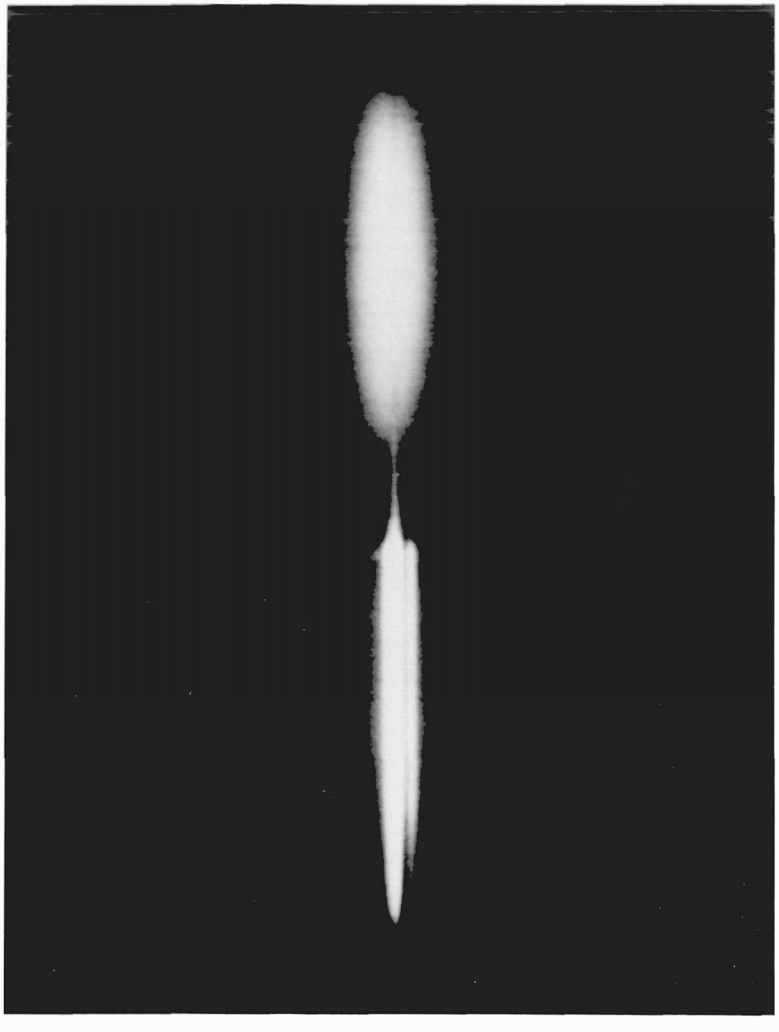

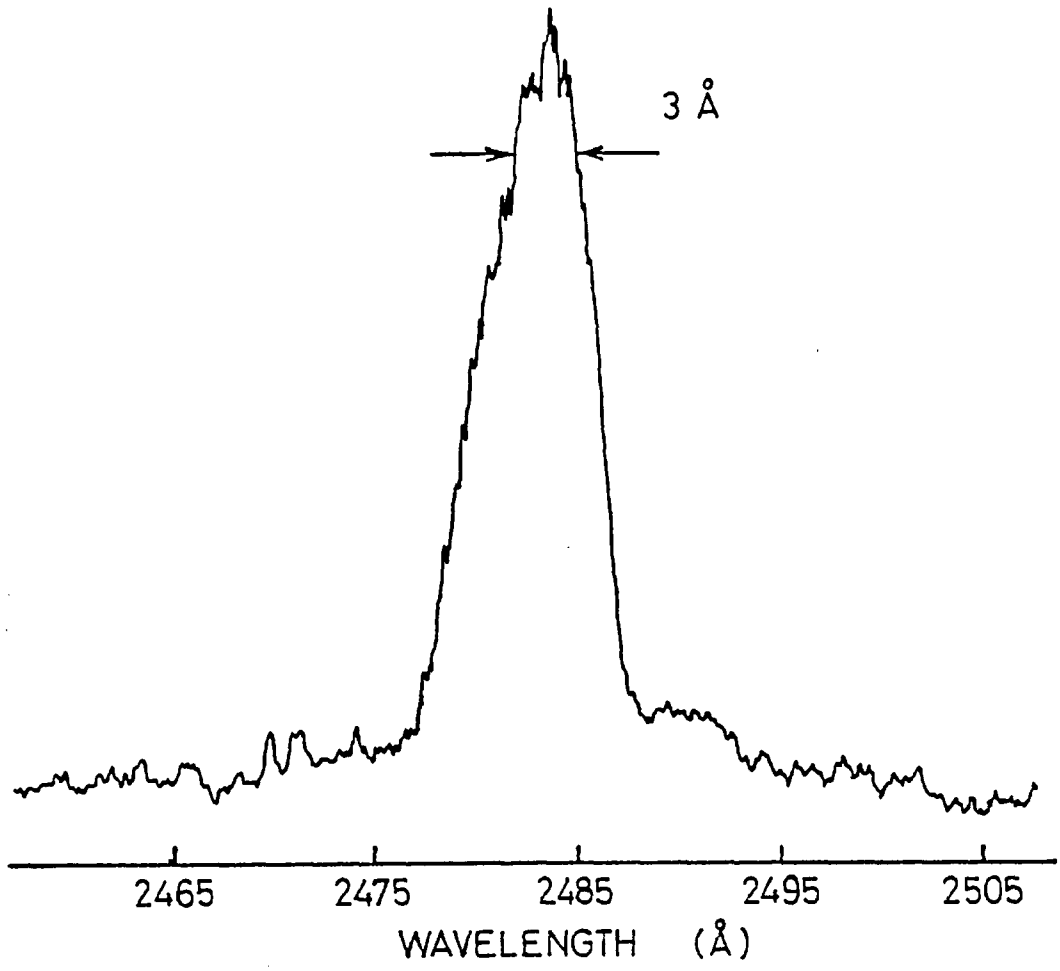


FIGURE 4.7 KrF laser spectrum.

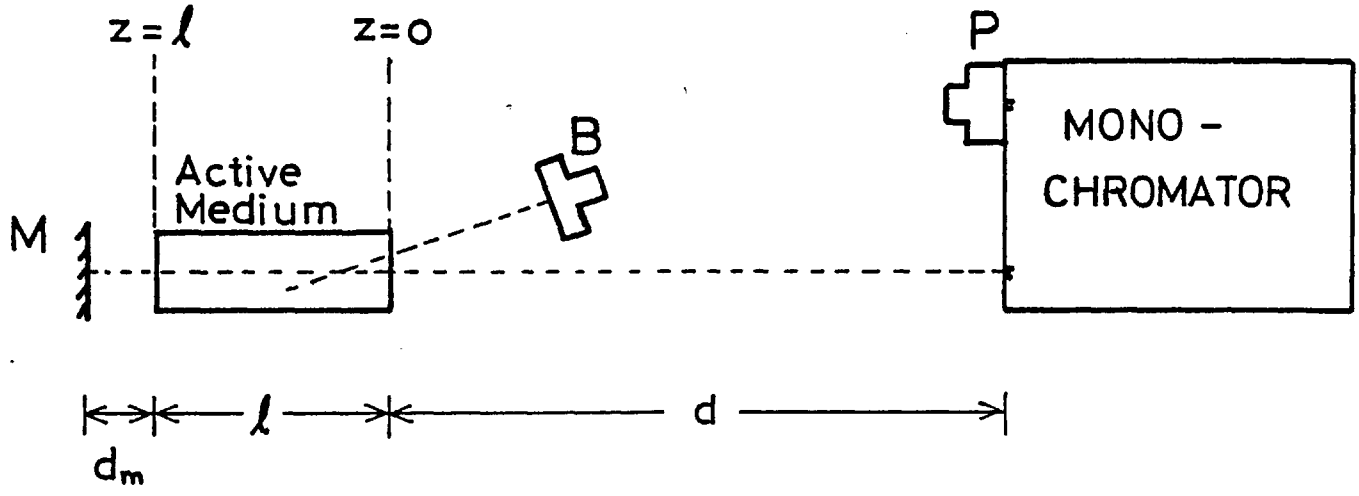


FIGURE 4.8 Schematic of experimental arrangement for gain measurement.

Gain $\alpha$ is assumed to be small signal and constant over the active length $\ell$ (= 12 cms). Other dimensions are $d_m$ = 15 cm, d = 108 cms (see Fig. 4.8). Solid angles are neglected and a "plane wave" analysis is used, valid if $d_m$, $\ell \ll d$, as in this case. A simple analytic solution exists for the relationship between signals $S_1$ and $S_2$ (mirror blocked and unblocked, respectively), valid for gain length products up to $\sim$ 10, assuming that the medium does not saturate.

Consider

$$S_1 = K_1 \int_{z=o}^{\ell} \frac{e^{\alpha z}}{(d+z)^2} \, dz \qquad 4.1$$

$$S_2 = S_1 + K_2 R \int_{o}^{\ell} \frac{e^{\alpha(2\ell - z)}}{s^2} \, dz \qquad 4.2$$

where $s = d + 2d_m + 2 = 160$ cm

$R$ = effective reflectivity of M $\simeq$ 0.80

$K$ = constant proportional to peak fluorescence power (arbitrary units), monitored by solar blind photodiode B.

The ratio between the two signals is

$$S_2/S_1 = 1 + R \frac{d^2}{s^2} \frac{K_2}{K_1} e^{2\alpha\ell} \frac{\int_o^{\ell} \frac{e^{-\alpha z}}{(1 - z/s)^2} \, dz}{\int_o^{\ell} \frac{e^{\alpha z}}{(1 + z/d)^2} \, dz} \qquad 4.3$$

To solve for $\alpha$, we find that integration by parts gives

$$\int_o^{\ell} \frac{e^{az}}{(1+bz)^2} \, dz = \frac{1}{b}\left[1 - \frac{e^{a\ell}}{(1+b\ell)}\right] + \frac{a}{b}\int_o^{\ell} \frac{e^{az}}{1+bz} \, dz \qquad 4.4$$

The integral on the right hand side of 4.4 is found by substitution of $t = a/b + az$ (a,b constants)

$$\int_0^{\ell} \frac{e^{az}}{1+bz}\,dz = \frac{e^{-a/b}}{b}\int_{a/b}^{a/b+a\ell}(e^t/t)\,dt \qquad 4.5$$

where

$$\int e^t/t\,dt = \ell nt + t + t^2/2.2! + t^3/3.3! + \ldots \qquad 4.6$$

Setting $a = -\alpha$, $b = -1/s$ for $S_2$, and

$a = \alpha$, $b = 1/d$ for $S_1$, we find

$$\frac{S_2}{S_1} - 1 = \frac{Rd(d+\ell)K_2 e^{\alpha\ell}}{s(s-\ell)K_1} f(\alpha) \qquad 4.7$$

where

$$f(\alpha) = \frac{s-\ell}{d+\ell} \frac{\left[\frac{1}{1-\ell/s} - e^{\alpha\ell}\right] - \alpha s e^{(-\alpha s+\alpha\ell)}\int_{\alpha s}^{\alpha s-\alpha\ell} e^t/t\,dt}{\left[1 - \frac{e^{\alpha\ell}}{1+\ell/d}\right] + \alpha d\, e^{-\alpha d}\int_{\alpha d}^{\alpha d+\alpha\ell} e^t/t\,dt} \qquad 4.8$$

Sala[101] has pointed out that $f(\alpha)$ can be simplified using the Taylor expansion:

$$f(\alpha) = f(o) + f'(o)\alpha + f''(o)\frac{d^2}{2} + \ldots \qquad 4.9$$

We find that $f(o) = 1$ exactly 4.10

$$f'(o) = (s-\ell)\left[-\frac{s}{\ell}\,\ell n(1-\ell/s) - 1\right]$$

$$-(d+\ell)\left[\frac{d}{\ell}\,\ell n(1+\ell/d) - \frac{1}{1+\ell/d}\right]$$

$$= 0.05 \qquad 4.11$$

f"(o) is smaller still.

Therefore for values of $\alpha \lesssim 0.2$ cm$^{-1}$, $f(\alpha) = 1$ to within 1%, and we can re-write (4.7) to get our final expression

$$\frac{S_2}{S_1} - 1 = \frac{Rd(d+\ell)K_2 e^{\alpha\ell}}{s(s-\ell)K_1}$$

$$= 0.44 \frac{K_2}{K_1} e^{\alpha\ell} \qquad 4.12$$

Any two consecutive shots determine $S_1$, $S_2$, $K_1$ and $K_2$. The value of $\alpha$ calculated from (4.12) will be an average between the two shots.

Fig. 4.9 shows signals recorded by photodiodes P and B while looking at consecutive shots in an Ar:Kr:$F_2$ mixture. Fig. 4.10 shows graphically how the peak gain and fluorescence power drop with shot number, for both $F_2$ and $NF_3$ mixtures. The large variations in the case of $NF_3$ are due to the fact that the laser cell was unpassivated. In both cases the gain dropped after a number of shots, and heavy scattering of a He-Ne laser beam was observed after $\sim$ 5 shots in the $NF_3$ case, $\sim$ 20 shots with $F_2$, implying the presence of break-down products from the cell walls and halogen donor.

These results show that gain is roughly doubled using fluorine instead of $NF_3$, and the importance of gas cleaning and renewal for continuous operation. The maximum repetition rate of the Pulserad system was only 0.5 min$^{-1}$, so no special measures were taken to recycle the gas.

According to equation 2.14, using the values given in Section 2.2.3, current density $j \sim 600$ A cm$^{-2}$ is required to attain the measured peak gain $\alpha \sim .15$ cm$^{-1}$. This is less than the peak current density at the anode ($\sim$ 900 A cm$^{-2}$) by a factor $^2/_3$, of the order expected due to scattering of the e-beam. The corresponding excitation

FIGURE 4.9 Sidelight and amplified spontaneous emission from KrF cell.
(a) left: 5 consecutive sidelight signals, recorded by photodiode B, 20 ns/div.
(b) top right: amplified spontaneous emission with back mirror M aligned, photodiode P, 100 ns/div.
(c) bottom right: amplified spontaneous emission with back mirror M blocked, photodiode P, 100 ns/div.

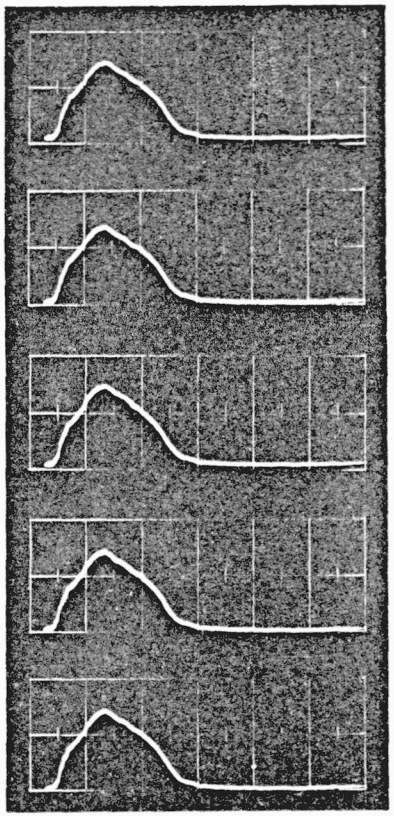

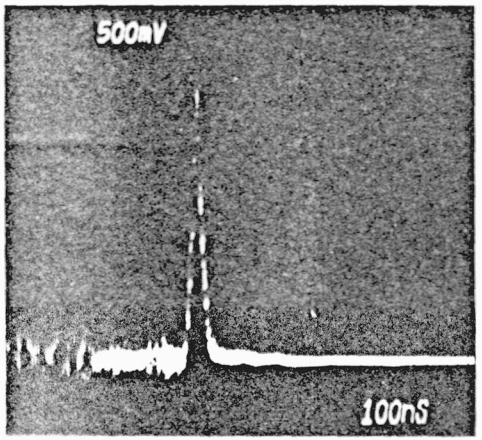
500mV
100nS

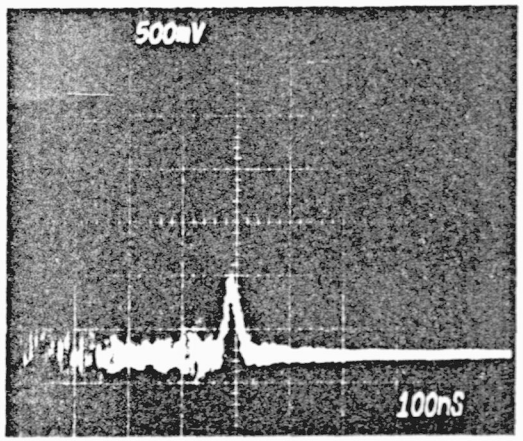
500mV
100nS

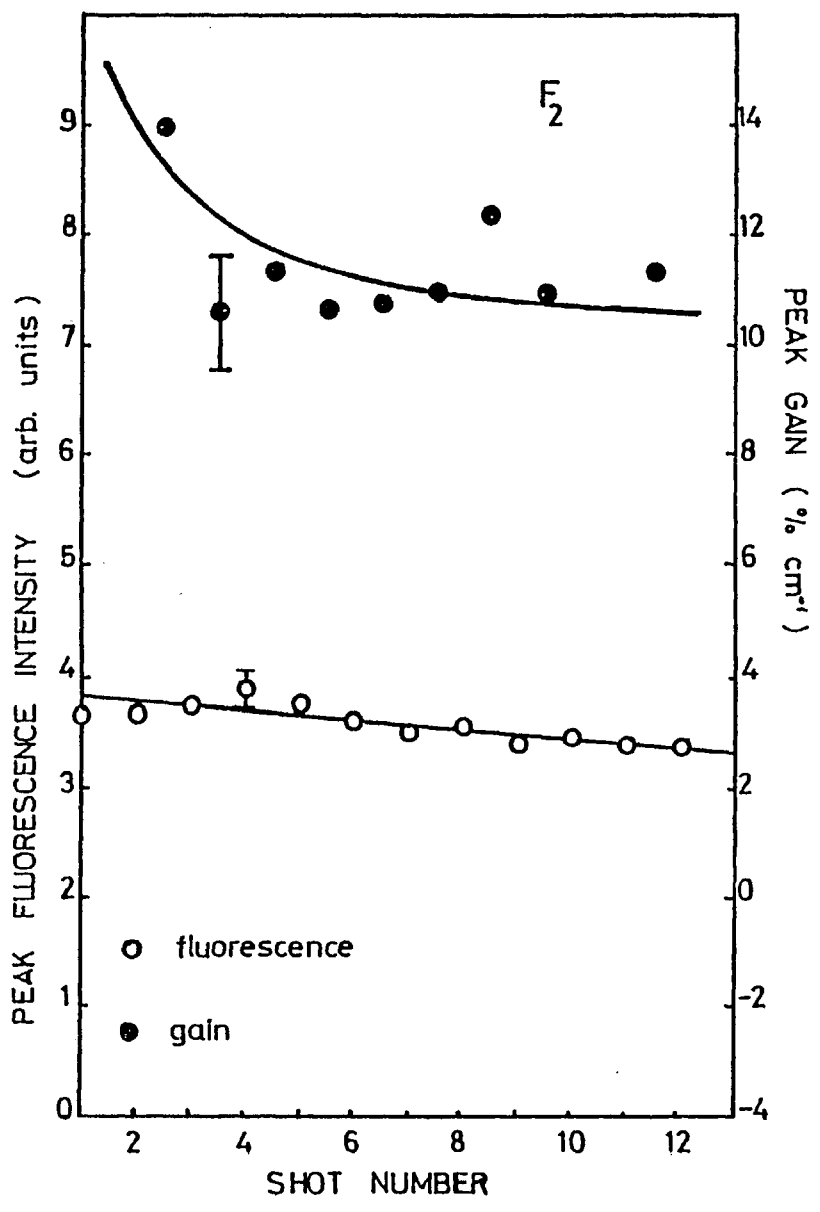


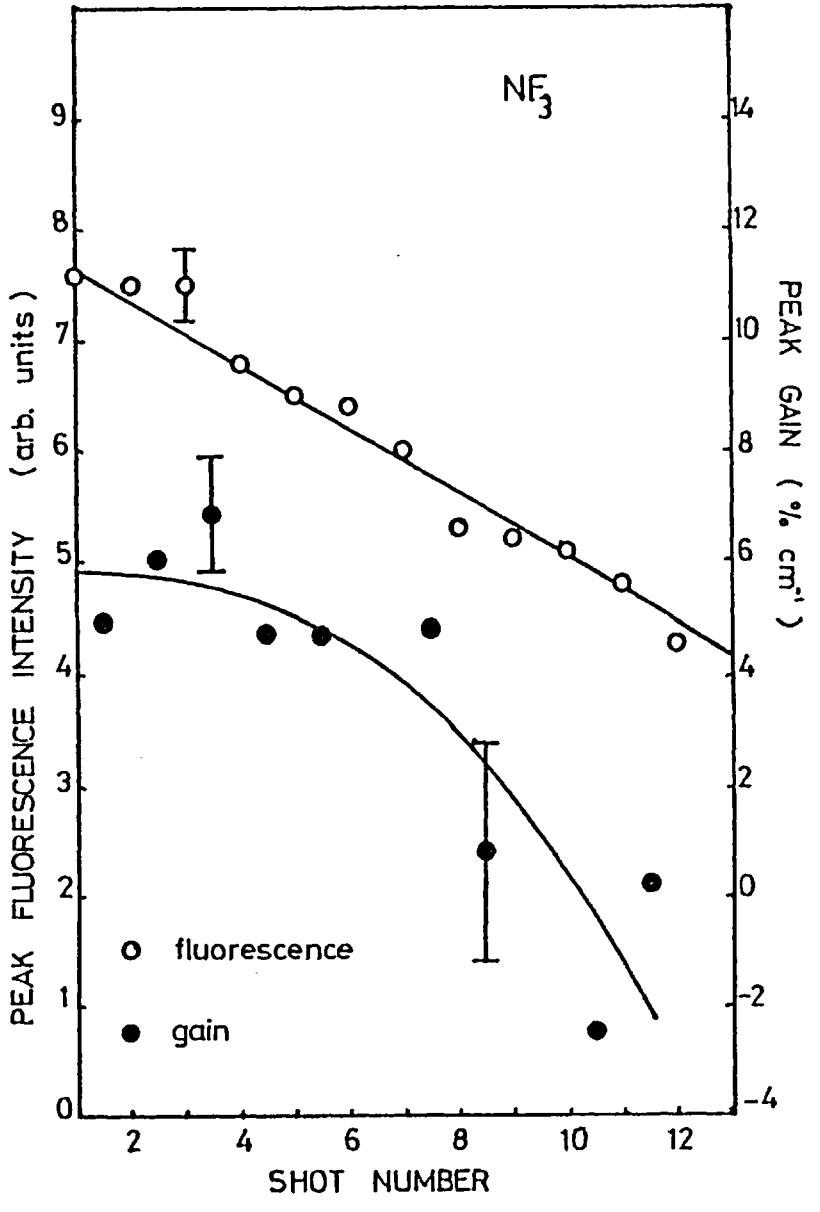


FIGURE 4.10 (a) Peak gain and fluorescence intensity versus shot number - $F_2$ gas mixture.

(b) Peak gain and fluorescence intensity versus shot number - $NF_3$ gas mixture.

rate of the medium is $P \sim 18$ MW $cm^{-3}$.

## 4.6 E-Beam Energy Transmission

E-beam energy transmission through the anode foils was measured by calorimetry, and is described here as a useful diagnostic. At the time, the anode consisted of two 50 μm titanium foils separated by 1 cm of air. The anode construction was changed to a single 50 μm titanium foil for the laser, as already shown in Fig. 4.1, so as to reduce transmission losses and scattering by the foil.

The calorimeter consisted of a copper-constantan thermocouple of negligible heat capacity, peened to the centre back of a rectangular piece of aluminium alloy sheet (8.4 cm x 16 cm x .16 cm) which intercepted the transmitted e-beam. Aluminium was chosen for its high heat conductivity and low electron backscattering cross-section. The experimental arrangement is shown in Fig. 4.11. The calorimeter was placed inside the laser cell and was supported by short lengths of brass studding which provided an electrical path to ground. Thermocouple leads were passed across an "O" ring seal to a chart recorder, which had a 0.1 μF capacitor connected across its input terminals to prevent damage from high frequency transients while firing the e-beam.

Initially the calorimeter was placed 1 cm from the anode foil. Fifteen torr of argon in the cell neutralized the space charge of the e-beam as it propagated and thus prevented beam spread. Fig. 4.12 shows typical chart recorder traces linearly and semi-logarithmically. The initial peak is caused by preferential heating of the centre of the calorimeter, which has a characteristic time to reach internal thermal equilibrium of the order of 10 seconds. The cooling curve following the peak is mainly due to radiation losses, indicated by the agreement of the calculated rate of radiative cooling with the

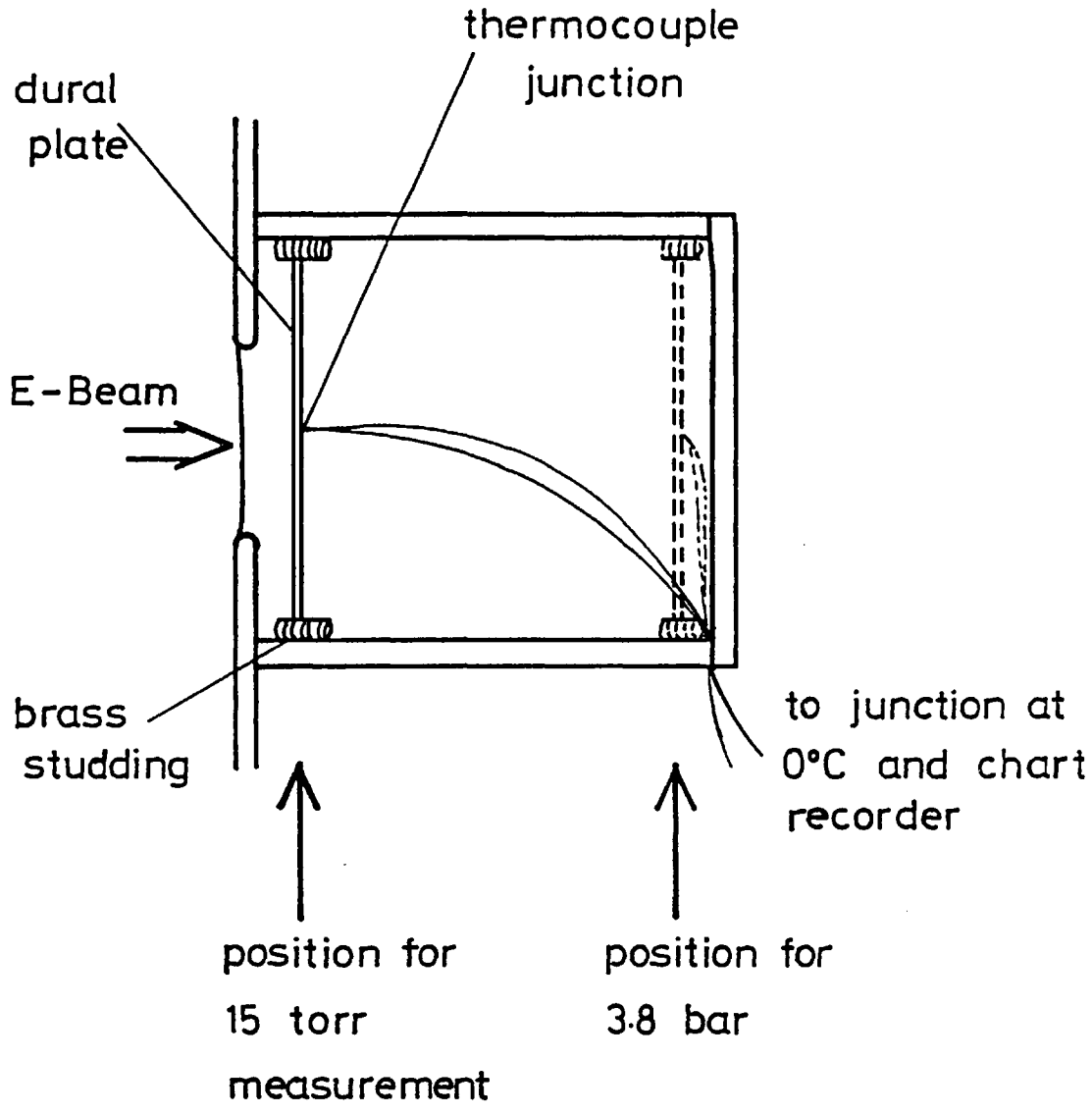


FIGURE 4.11 Experimental arrangement for e-beam transmission measurements.

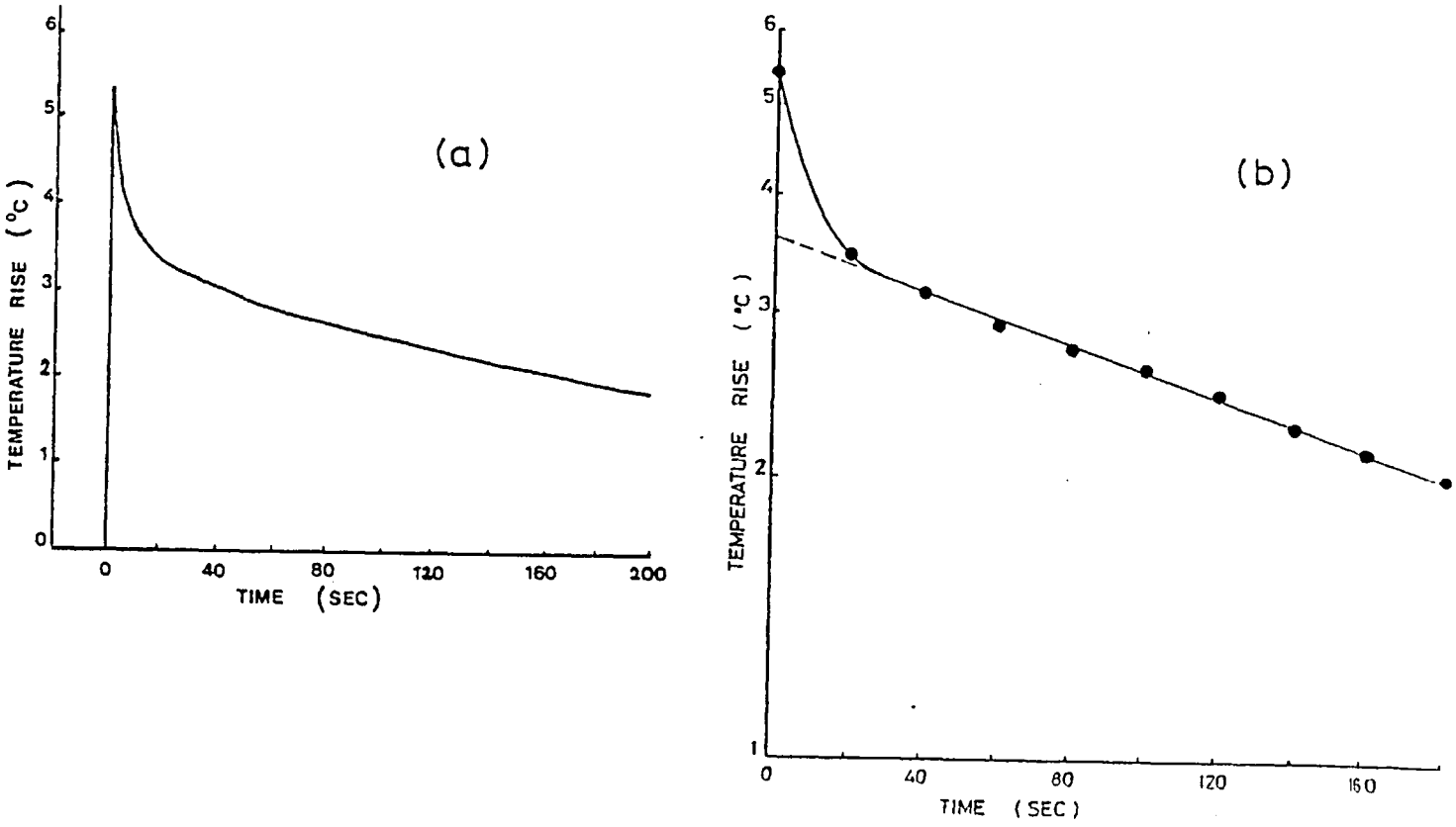


FIGURE 4.12 (a) Recorded calorimeter signal versus time.
(b) Calorimeter signal plotted semi-logarithmically.

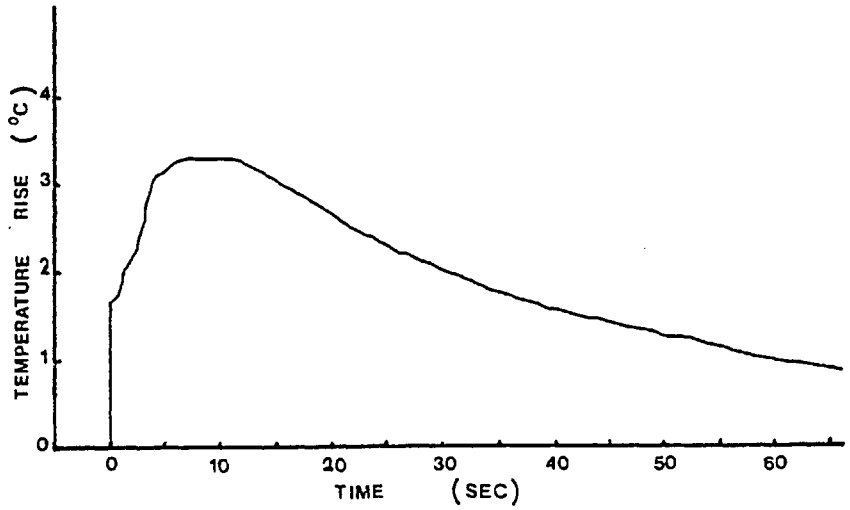


FIGURE 4.13 Calorimeter signal versus time in high pressure Ar.

measured rate to within 5%. For a small temperature rise, radiative cooling obeys Newton's cooling law, and a least squares straight line fit to the logarithmic decay after time t = 40 seconds gives a corrected temperature rise in the calorimeter of 3.6 (± 0.2)$^{o}$C, corresponding to a transmitted energy of 185 (± 15) joules, slightly more ($\lesssim$ 10%)[102] if backscattering is taken into account. This is roughly half the estimated initial e-beam energy of 350 (± 70) joules (see Chapter 5).

Energy incident on the back plate of the laser cell was also measured by placing the calorimeter 10 cm from the foil (see Fig. 4.11), at an argon pressure of 3.8 bar to simulate laser conditions. At high pressure it is important to ensure that gas heating of the calorimeter does not distort the e-beam energy measurements. Fig. 4.12 shows the chart recorder output in this case, on a faster time scale. The instantaneous rise represents the prompt e-beam heating of the calorimeter, followed by a later rise due to gas heating. Assuming that the calorimeter is uniformly heated by the scattered e-beam, the instantaneous temperature rise corresponds to an energy of 90 joules, a factor of 2 less than the transmitted energy. The remainder is absorbed by the gas medium or side-walls, putting an upper limit of 50% absorption of transmitted e-beam energy by the gas in the 1.6 litre laser cell.

Closer to the foil it is difficult to distinguish the effects due to gas heating and calorimeter thermalization using this type of simple calorimeter. If the complicating effect of long thermalization times is to be avoided, it is necessary to divide the calorimeter up into many small independent sections and record their total signal.

CHAPTER 5

# CO-AXIALLY-PUMPED KrF AND XeCl LASERS

## 5.1 Introduction

In this chapter the design and operation of a co-axial laser diode is described. Because of the possibility of significant beam pinch, it was made compatible with either axial or radial current return operation.

At pressures typical of the rare gas halides ($\sim$ 3 bar for Ar-diluent mixtures, $\sim$ 6 bar for Ne-diluent), a 500 keV electron has a penetration depth of approximately 15 cm, calculated from equation 2.3 using the values for stopping power dE/dx given by Daugherty[21] (see Fig. 2.2) and multiplied by a factor of 2 to account for electron scattering. Therefore to attain near 100% deposition of transmitted electron energy in the gas medium, the anode diameter $d_a$ of a 500 kV co-axial system should be in the range 12 cm $\leq d_a \leq$ 15 cm, allowing for energy loss in the foil. However, in the present work the current density j incident on the anode was kept high (200 amp $cm^{-2}$) and the optics were kept to a reasonable size, using a 3.8 cm diameter anode. In this case, an estimated 20-30% of the transmitted e-beam energy was absorbed by the gas medium. The current density just inside the anode was $\sim$ 400 amp $cm^{-2}$, and increased towards the centre due to the focussing effect of the co-axial system.

Laser action was observed in both KrF and XeCl, at 248 nm and 308 nm respectively. Compared with the transverse laser, laser energy was an order of magnitude greater. This is attributed to the increased average pump density in the active volume, a more favourable pattern of energy deposition, and an increased gain length.

## 5.2 Laser Diode

The laser diode is shown approximately to scale in Fig. 5.1, set up for axial current return. The cathode consisted of 100 μm titanium foil pierced at 6 mm intervals to form an array of spikes, in the shape of an incomplete cylinder with an emitter radius of 4.0 or 4.2 cm. A $100^{\circ}$ opening along its length allowed for radial current return. Fig. 5.2 shows a side view of the laser diode, set up for radial current return. In the latter case, the current to ground passed through mild steel plates 1.5 mm thick, which were screwed together to hold a brass foil contact with the anode tube. The plates were carefully adjusted to bisect the cathode opening to within ± 1 mm. Fig. 5.3 is a photograph of the partially assembled radial return diode. To convert to axial return geometry, the plates were replaced by tightly fitting stainless steel rings placed over the anode tube ends, providing electrical contact between the anode and the stainless steel laser end-cells, and hence to ground.

The cathode foil, 14 cm or 18 cm in length, was conveniently held by springy wire clips in an aluminium sheet former (not shown in Fig. 5.3), slotted into a highly polished, properly radiused cathode holder 21 cm in length, 2 cm thick. The radiused edges of the cathode holder ensured that electrical field strengths did not exceed 200 kV $cm^{-1}$, preventing cold field emission of electrons from the dielectric coated surfaces. Field strengths were checked beforehand using highly conducting silver paint on resistive paper to plot the 2-dimensional potentials of different diode configurations, and were highest in the gap region between the radial return plate and the open "jaws" of the cathode holder.

The orientation and position of the cathode holder were fully adjustable by means of a universal joint attached to the cathode stem.

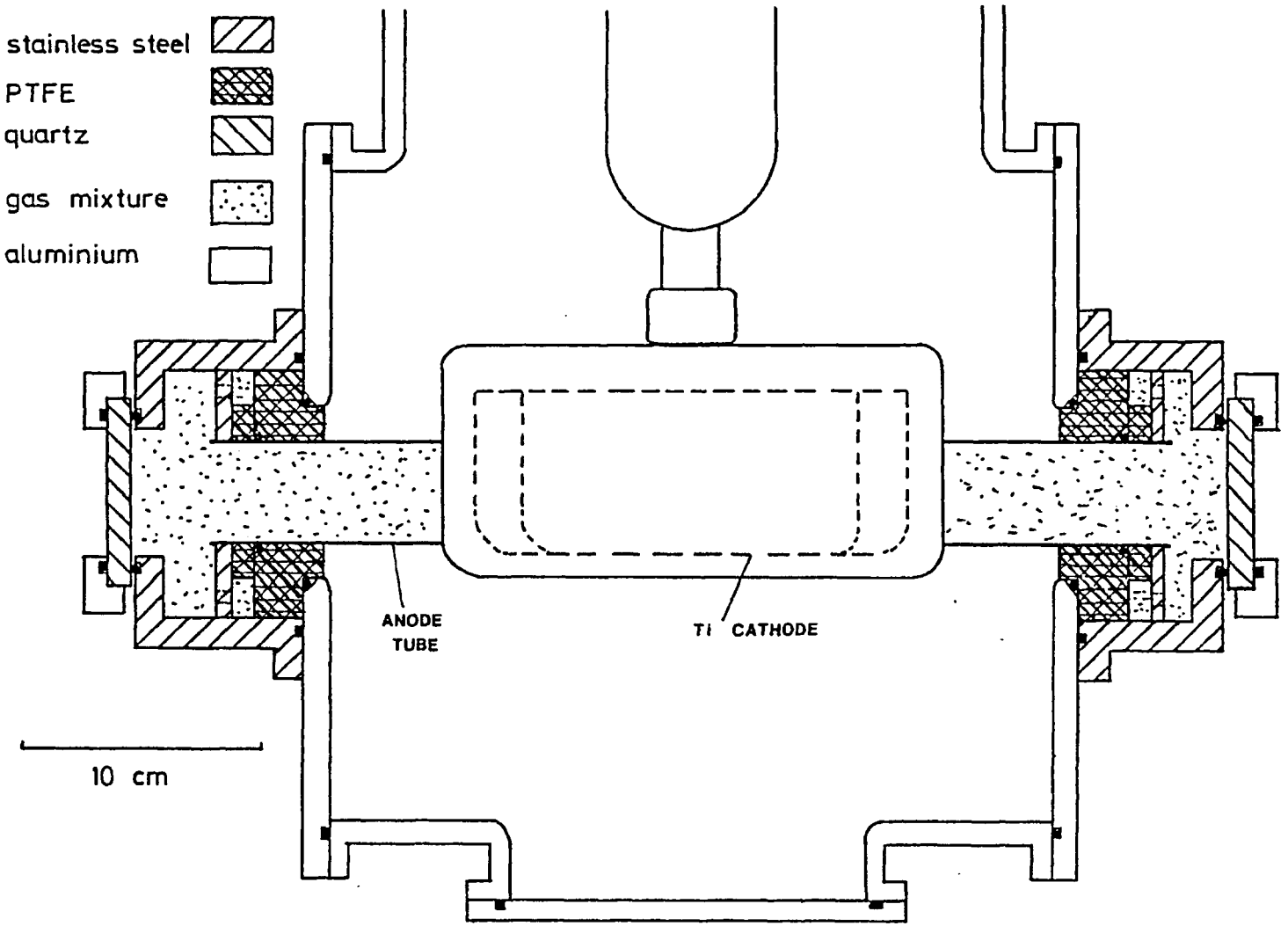


FIGURE 5.1 Co-axial laser diode using axial current return geometry.

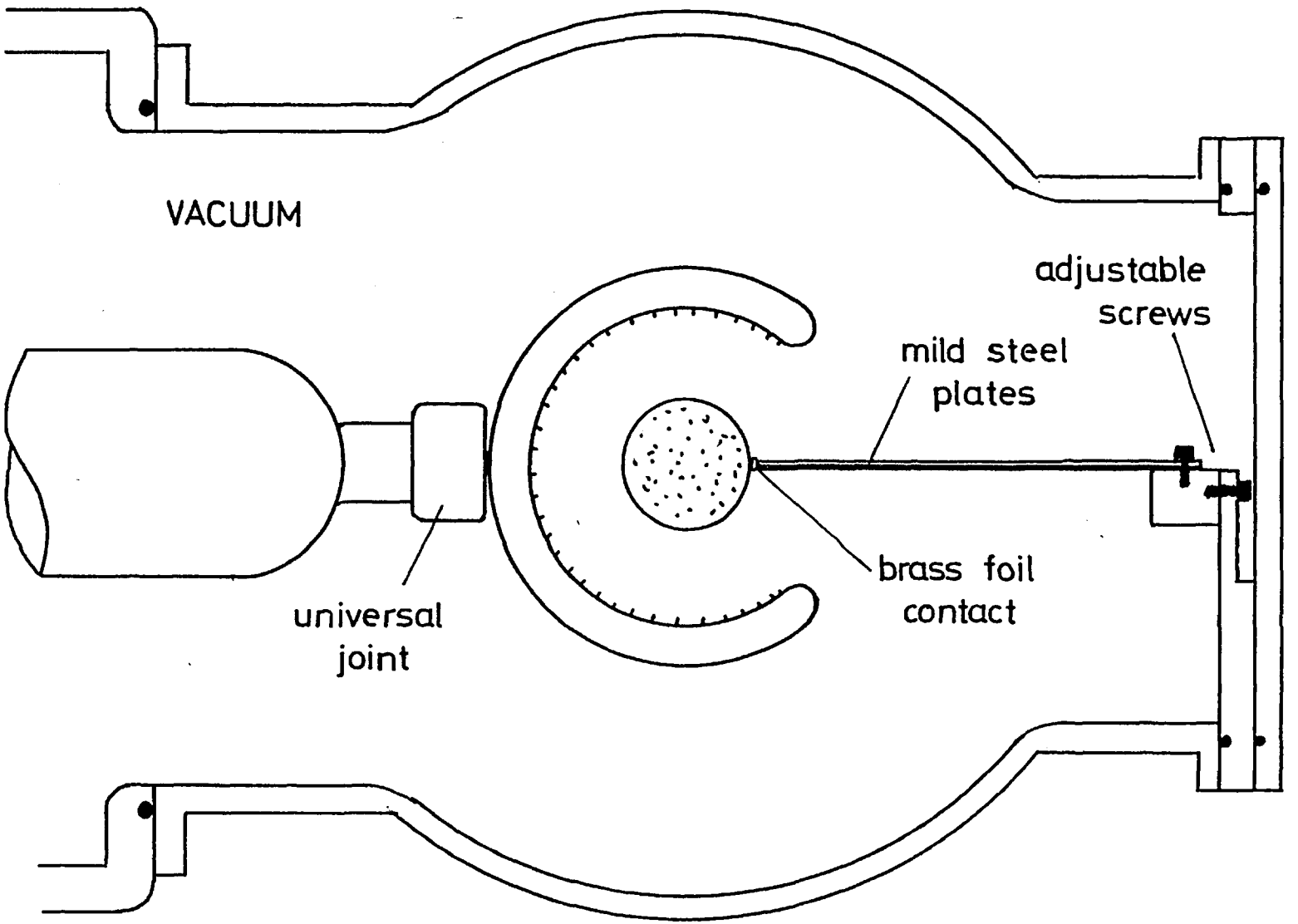


FIGURE 5.2 Side of laser diode using radial current return geometry.

FIGURE 5.3 Partially assembled radial return diode.

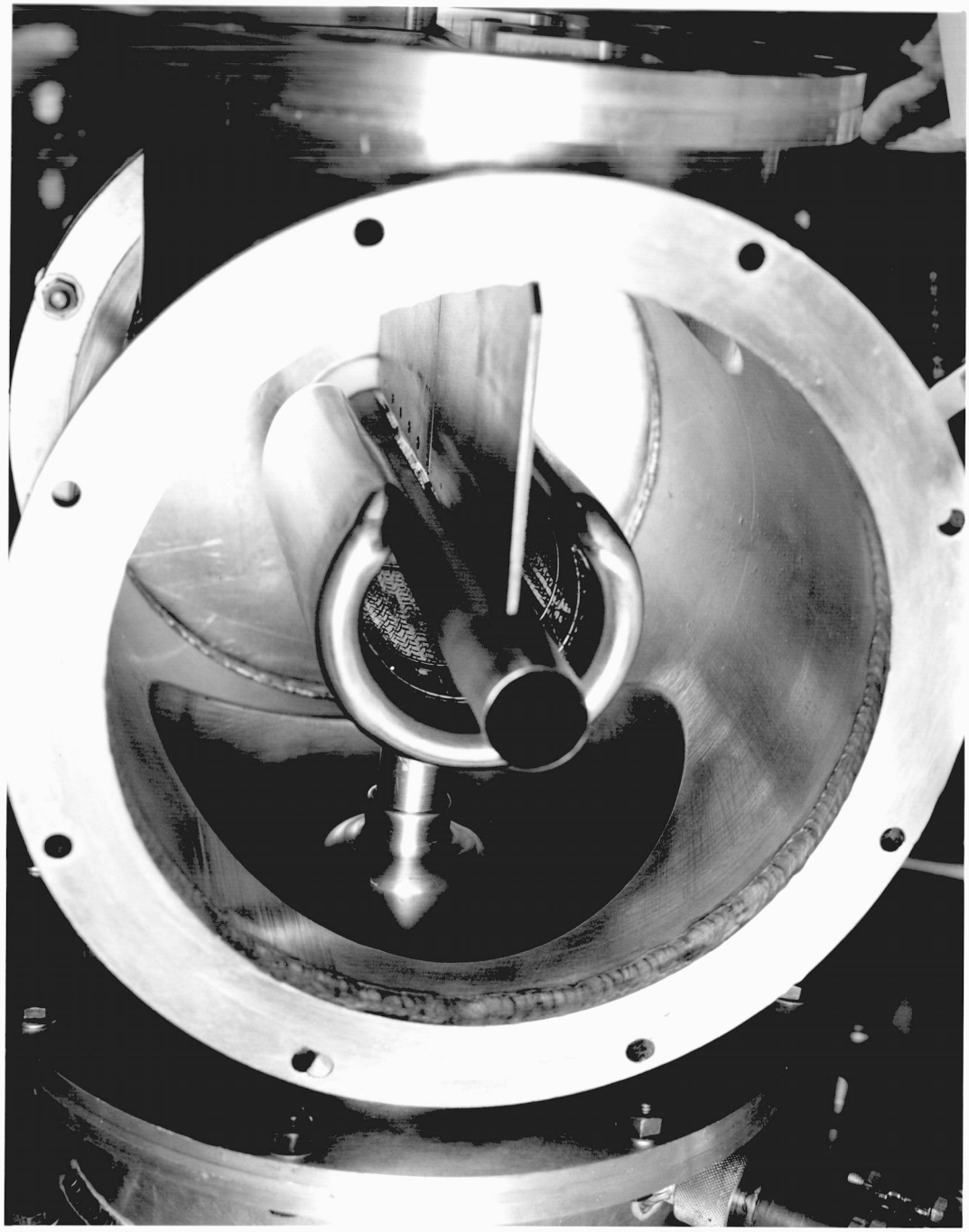

The anode tube (Oxford Instruments) was stainless steel, electrochemically etched to 95 (± 15) μm from an initial thickness of 400 μm. In some cases titanium tubing was used, laser welded (JK Lasers) from 100 μm titanium foil.

## 5.3 Anode Tubes

The first co-axially-pumped lasers had anode tube diameters of several millimetres[28,103,104], giving the thin anode enough strength for operation at 10-20 bar, typical of pure excimer systems. The rare gas halides operate at lower pressures and therefore require larger diameter anodes having less strength for a given foil thickness. Allowing for a safety factor of two, the maximum pressure p supported by a cylindrical tube of radius r and foil thickness t is

$$p = St/2r \qquad 5.1$$

where S is the yield strength of the material. A 50 μm stainless steel anode 10 cm in diameter is quoted in reference *29*, and to increase the pressure above the maximum unsupported value p = 3.4 bar an outer support structure, known as an "Hibachi", is required. In the present work a smaller 3.8 cm diameter unsupported anode was used. Stainless steel 95 μm thick has a value p = 15 bar, greater than necessary due to the difficulty of etching the tube further without pinholes developing. A sample stainless steel anode was successfully tested at full e-beam power at a pressure of 12.6 bar, limited by the gas handling system.

As an alternative, laser welded 100 μm titanium foil tubes 3.8 cm in diameter were used. These had a value p = 14 bar and gave increased laser energy due to the lower energy loss in the foil compared to stainless steel (130 keV compared to 220 keV).

The excitation rate P (see equation 2.1) does not depend strongly on electron energy near 500 keV, and it is not immediately clear why the reduced transmitted electron energy using the stainless steel anode should affect the laser energy, since the anode diameter is well below the electron penetration depth using either type of anode material. The explanation is that it is an oversimplification to consider peak electron energy only; the stainless steel anode completely absorbs incident electrons in the energy range 130-220 keV, which are transmitted by the titanium anode during voltage build-up and decay, and which are evidently a significant source of pump energy.

The limitation on the titanium foil thickness was imposed by welding requirements. Although stainless steel tubes absorbed an appreciable fraction of the incident electron energy, they were used most of the time, because of the low cost.

The arrangement for etching stainless steel tubes is shown in Fig. 5.4. The etching mixture was 10% conc. orthophosphoric acid, 11% conc. sulphuric acid, 20% water and 59% glycerol. Stainless steel mesh lining the two litre graduated cylinder acted as a cathode at about -3 volts. The resulting current of $\sim$ 2 amps removed metal from the anode at $\sim$ 5 $\mu m\ hr^{-1}$, an order of magnitude faster than the calculated pure electrolytic rate. Perspex spacers centred the tube, which was frequently rotated and reversed to ensure uniform etching. The rate of etching was accurately controlled by variation of the current.

Both types of tube developed pinhole leaks after about 50 shots, caused by buckling of the tube after repeated shock heating and expansion of the tube ($\Delta T$ = 20-25$^{o}$C). Fig. 5.5 shows titanium and stainless steel anode tubes after removal from the diode. Millimetre diameter tubes do not buckle in this manner, freely sliding through

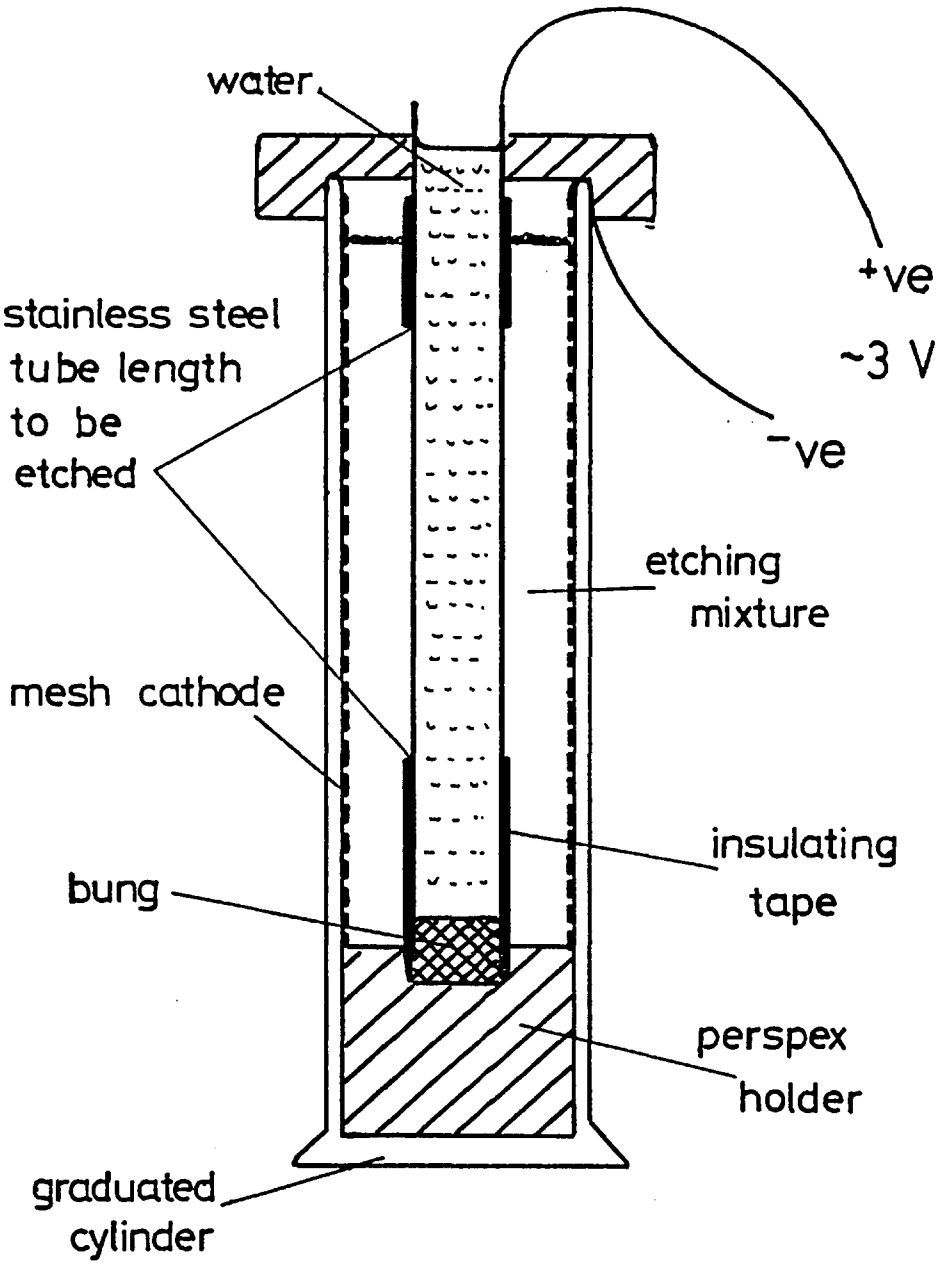


FIGURE 5.4 Etching of stainless steel anode tubes.

FIGURE 5.5 Anode tubes: stainless steel (left), titanium (middle), 6.4 mm diameter anode showing effect of beam pinch (right).

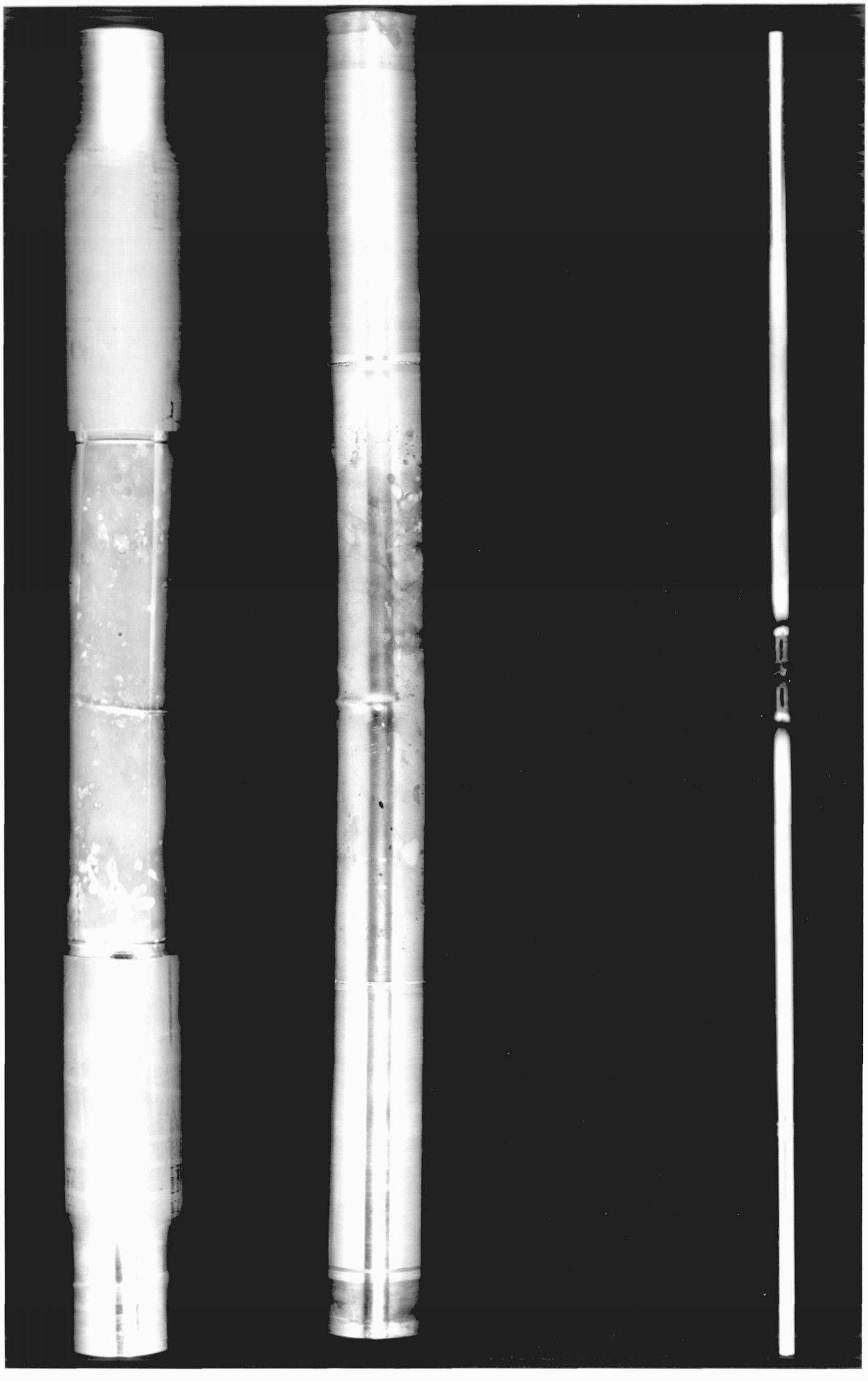

the vacuum seal instead[103]. Larger tubes are more likely to buckle due to their relatively low strength and increased friction at the vacuum seal. An Hibachi solves the problem by dividing the foil into N mechanically and thermally independent sections, each experiencing stress reduced by a factor $N^{-1}$.

## 5.4 Beam Pinch and the Radial Return Diode

Equation 2.20 predicts that the angle of beam pinch at the peak of the pump pulse in the axial current return diode will be $\theta = 72^{o}$, setting the measured parameters at $r_a = 1.9$ cm, $r_c = 4.2$ cm, $I = 35$ kA, $V = 500$ keV ($\gamma = 2$, $\beta = 0.86$), whereas according to the discussion of Section 2.3.3 there is no longitudinal pinching in a radial current return diode*. This was checked using blue cellophane (Avisco MSC 185, Hewlett Packard) e-beam dosimetry to monitor the time-integrated, space-resolved e-beam dose in both the axial and radial current return diodes, showing the broad features of e-beam flow in each case. Passage of electrons through the cellophane bleaches the dye, and a calibration curve yielded the e-beam dose (megarads) for a given fractional change in transmittance at 655 nm, $\Delta T = (T_2 - T_1)/T_1$, where $T_1$ and $T_2$ are the transmittance before and after irradiation, respectively. A microdensitometer in conjunction with a filter transmitting at 655 nm was used to measure the change in density $\Delta D = D_2 - D_1$ of the cellophane, related to $\Delta T$ by the expression

$$\Delta T = 10^{-\Delta D} - 1 \qquad 5.2$$

---

* Equation 2.21 predicts a cut-off current $I_c = 14$ kA for a 500 kV diode having radii $r_a = 3.2$ mm, $r_c = 27$ mm. Fig. 5.5 shows an anode tube from a nominal ten ohm diode of the given dimensions, showing how beam pinch has destroyed the centre of the anode after one shot, at an estimated peak current of 30 kA[105].

Cellophane dosimetry thus provides a useful means of comparing relative e-beam doses.

The transmitted e-beam dose using axial or radial return geometry was compared by inserting into the stainless steel anode a close fitting aluminium mandrel lined with cellophane. In the axial return case, copper clips provided a low inductance path to ground, and in both cases the identical anode tube was used. Fig. 5.6 shows cellophane microdensitometer traces for axial and radial return, taken longitudinally and around the inner circumference of the anode. The longitudinal traces clearly show how beam pinch results in a smoothed out profile and shorter pump length (FWHM) in the axial return case only. The circumference pattern shows a dip in the e-beam intensity due to the $100^{o}$ gap in the cathode. The e-beam dose half-width relative to the average background is shown, and was the same in each case to within experimental error - $90^{o}$ ($\pm$ 10).

According to equation 2.26, a deflection of $\theta = 35^{o}$ (setting $i = 2 \times 10^{5}$ amp $m^{-1}$, $d = 2.7$ cm) is expected of electrons generated in the gap region between the return plate and the cathode of the radial return diode (see Fig. 2.8). The circumference pattern shows no clear evidence of this, probably because a greater value of $\theta$ is required to effectively couple energy into the anode tube. A more sensitive test is to look at the e-beam dose on the radial return plate. As already noted, electrons generated in the gap region of the diode are deflected towards the anode by the magnetic field set up by the radial current return. This was investigated by comparing e-beam flow to the radial return plate in the presence of either radial or axial return current, i.e. in the presence or otherwise of the relevant magnetic field. Fig. 5.7 shows the diode configuration for the two cases. In case I, ordinary radial return geometry was used. In case II, the

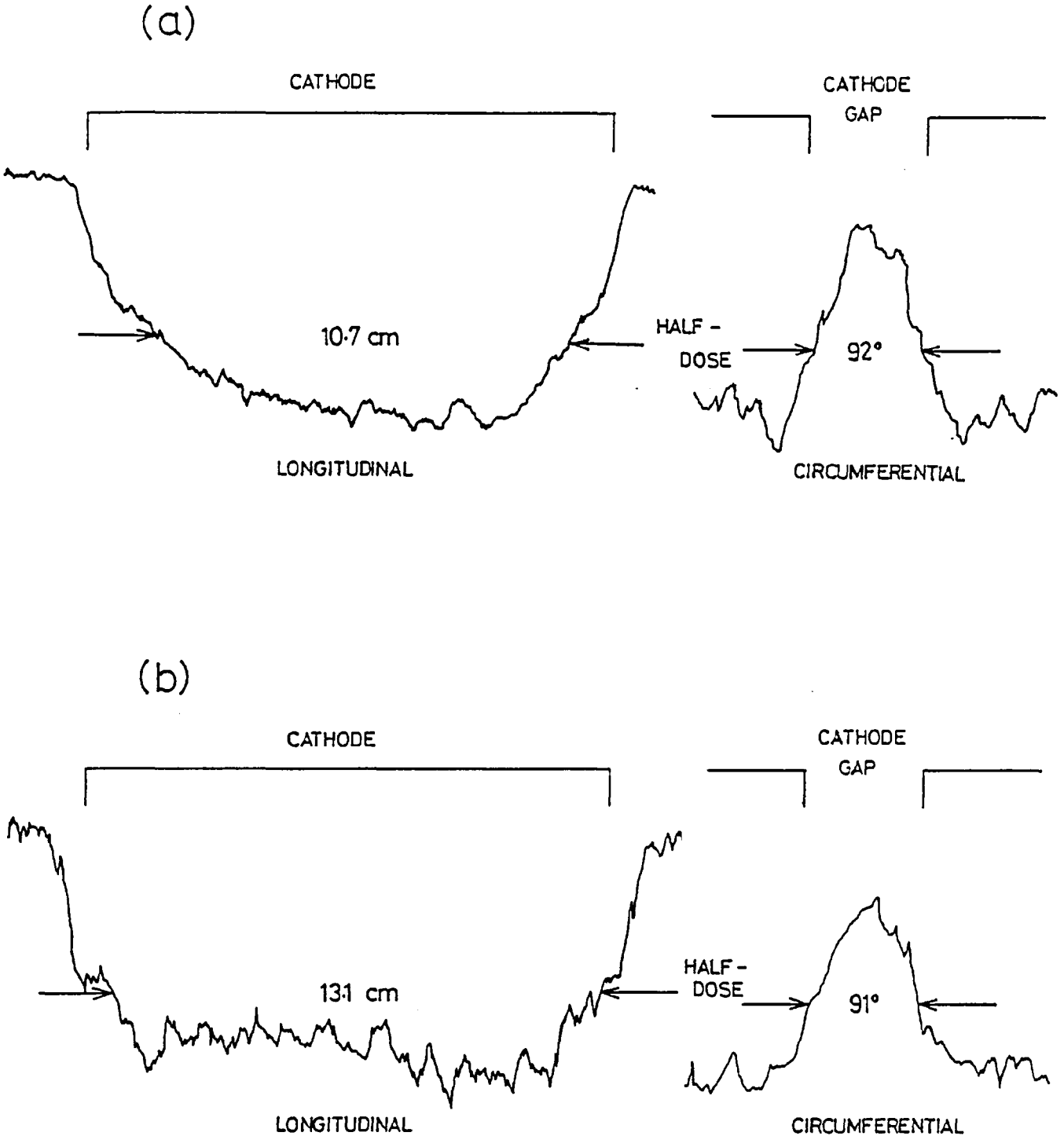


FIGURE 5.6 Microdensitometer traces of blue cellophane used to record transmitted e-beam dose; (a) axial return geometry, (b) radial return geometry.

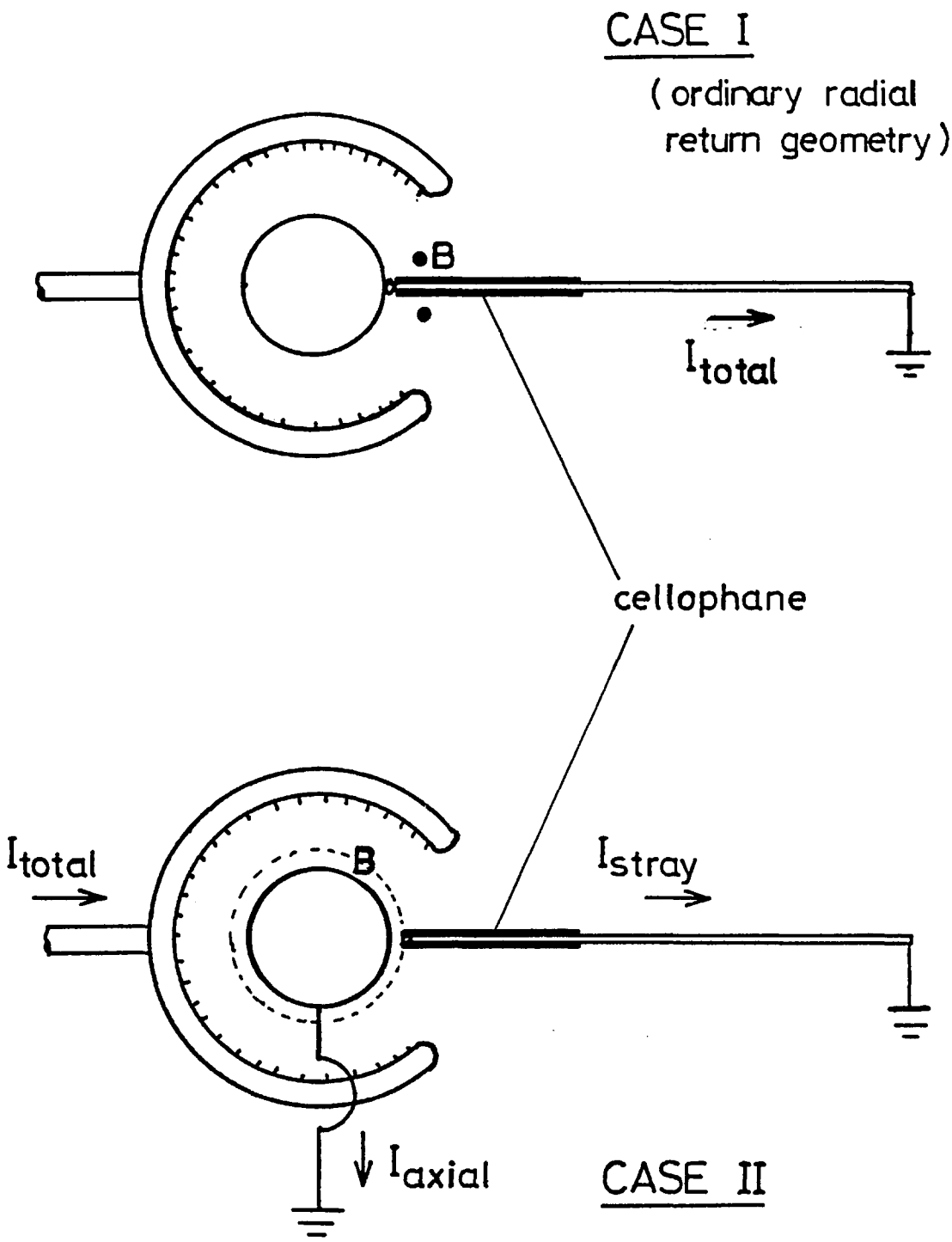


FIGURE 5.7 Case I and II diode configurations.

return current flowed axially to ground through copper grounding clips at both ends of the anode, and the radial return plate was backed off from the anode by 3 mm. The return plate was left in essentially the same position as in case I, but without providing a path for radial current return. In this way, using blue cellophane on the return plate surfaces, cases I and II demonstrate e-beam flow in the presence and absence, respectively, of the radial return current magnetic field, assuming that stray current to the return plate in case II is relatively small.

The relative e-beam dose over the surface of the current return plate in cases I and II is shown in the form of contour maps in Fig. 5.8. In both instances the peak total current was 36 kA. The contours were drawn from points plotted at 1 cm intervals, and show an overall shift towards the anode of approximately 1 cm in case I compared to case II, consistent with the expected deflection. The total relative e-beam dose to the return plate was the same for cases I and II to within experimental error (± 10%).

An important piece of information is the fraction F of e-beam energy incident on the anode tube as opposed to the radial return plate, using ordinary case I geometry. Assuming that in the present instance F is approximately equal for cases I and II, it can be measured by monitoring the axial current $I_{axial}$ and stray current to the plate $I_{stray}$ separately, using case II diode configuration. Before presenting these results, current and voltage monitoring in the diode is described.

### 5.4.1 Current monitoring

Total e-beam current was usually monitored with a Physics International Model PIM-199 fluxmeter or B-probe, consisting of a 2.5 cm diameter conducting loop placed inside the vacuum chamber,

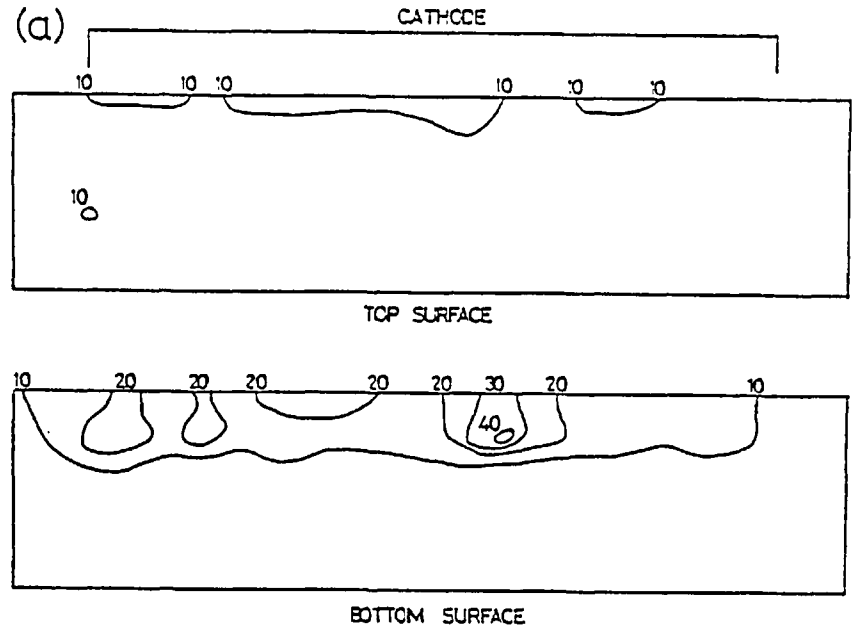


FIGURE 5.8 E-beam dose contour maps: (a) case I, (b) case II.

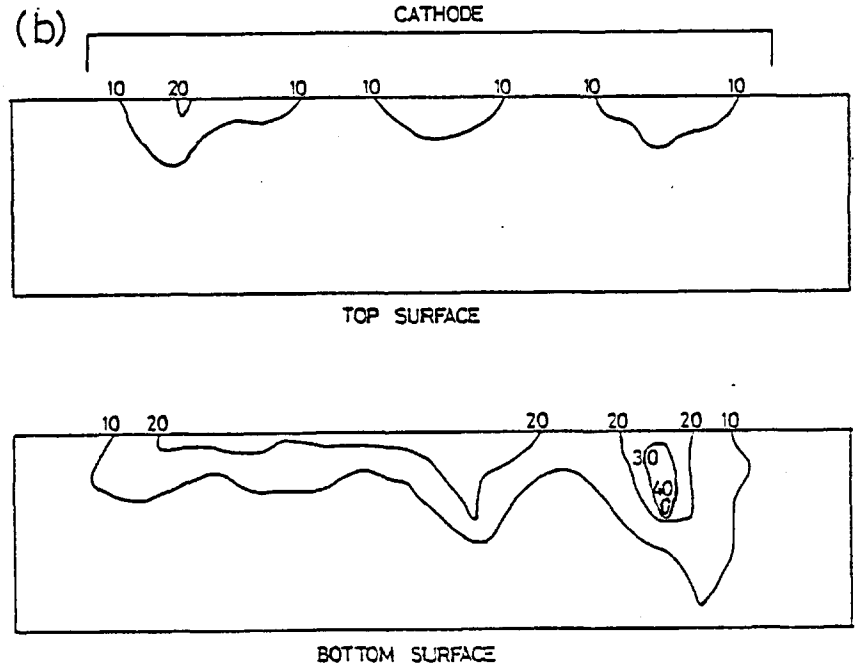

giving an output voltage proportional to the magnetic flux linking it, proportional in turn to the cathode stem current. The sensitivity of the combined B-probe and 10 m of 50 ohm co-axial cable was 2.12 volts $kA^{-1}$. Longer cable lengths decreased the sensitivity by a few percent and were corrected for when necessary. Fig. 5.9(a) shows a typical B-probe current waveform, using axial current return geometry. Signals were reproducible to within 5%.

Using case II diode configuration, $I_{axial}$ and $I_{stray}$ were measured separately with foil monitors in series with the diode. Fig. 5.10 shows the construction of the two monitors.

The axial current monitor was constructed from 20 μm nichrome foil and provided one half of the path to ground, an identical foil construction at the other end of the anode providing the other half. The sensitivity was calculated from the measured anode tube and foil resistances, which were 6.4 mΩ and 15.3 mΩ respectively. Assuming that the current divides equally between the arms of the anode, the equivalent circuit is shown in Fig. 5.11. The calculated sensitivity at the input to the 50 ohm cable was 3.94 volts $kA^{-1}$.

The stray current monitor was constructed from 5 μm nichrome foil in the form of a cylinder 30.4 cm in diameter and 3.2 cm long, measured resistance 8.3 mΩ. The equivalent circuit in Fig. 5.12 gives a calculated sensitivity of 4.3 volts $kA^{-1}$ at the input to the terminated 50 ohm cable.

Axial and stray current waveforms are shown in Fig. 5.9(b) and (c). The recorded signals were highly reproducible, shown by the overlapping current waveforms. Agreement between ($I_{axial}$ + $I_{stray}$) and the B-probe ($I_{total}$) was within 10%, as shown in Fig. 5.13.

FIGURE 5.9

(a) Total current, B-probe monitor, pure axial return geometry, 20 ns/div., 25 kA/div.

(b) Axial current, foil monitor, case II diode configuration, 20 ns/div., 28 kA/div. Top - single trace; bottom - 3 overlapping traces.

(c) Stray current, foil monitor, case II diode configuration, 20 ns/div., 4 kA/div. Top - single trace; bottom - 2 overlapping traces.

(d) Voltage, pure axial return geometry, 20 ns/div., 350 kV/div.

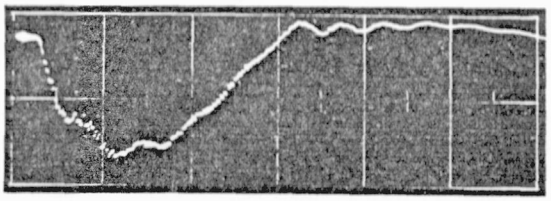

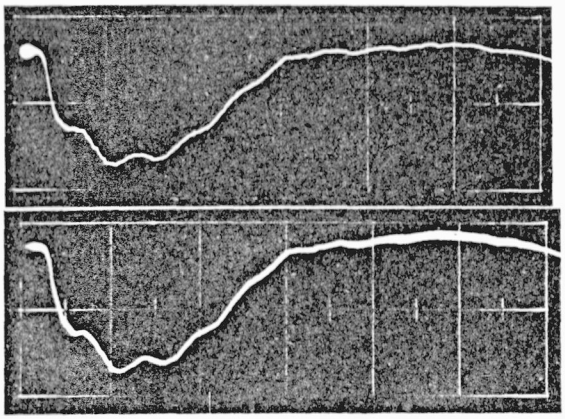

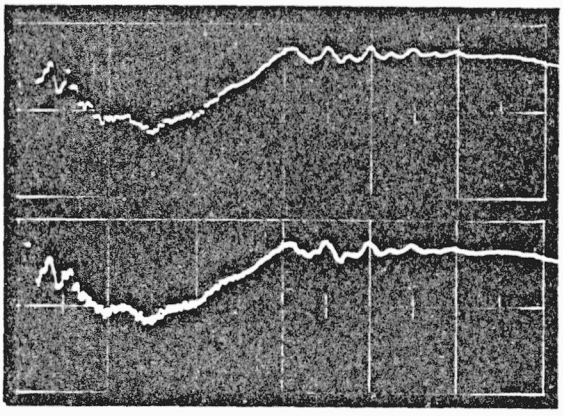

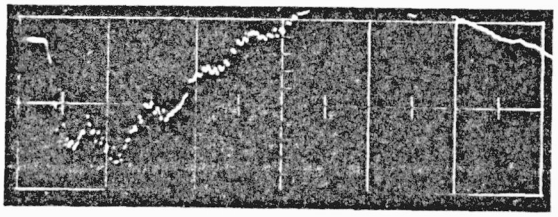

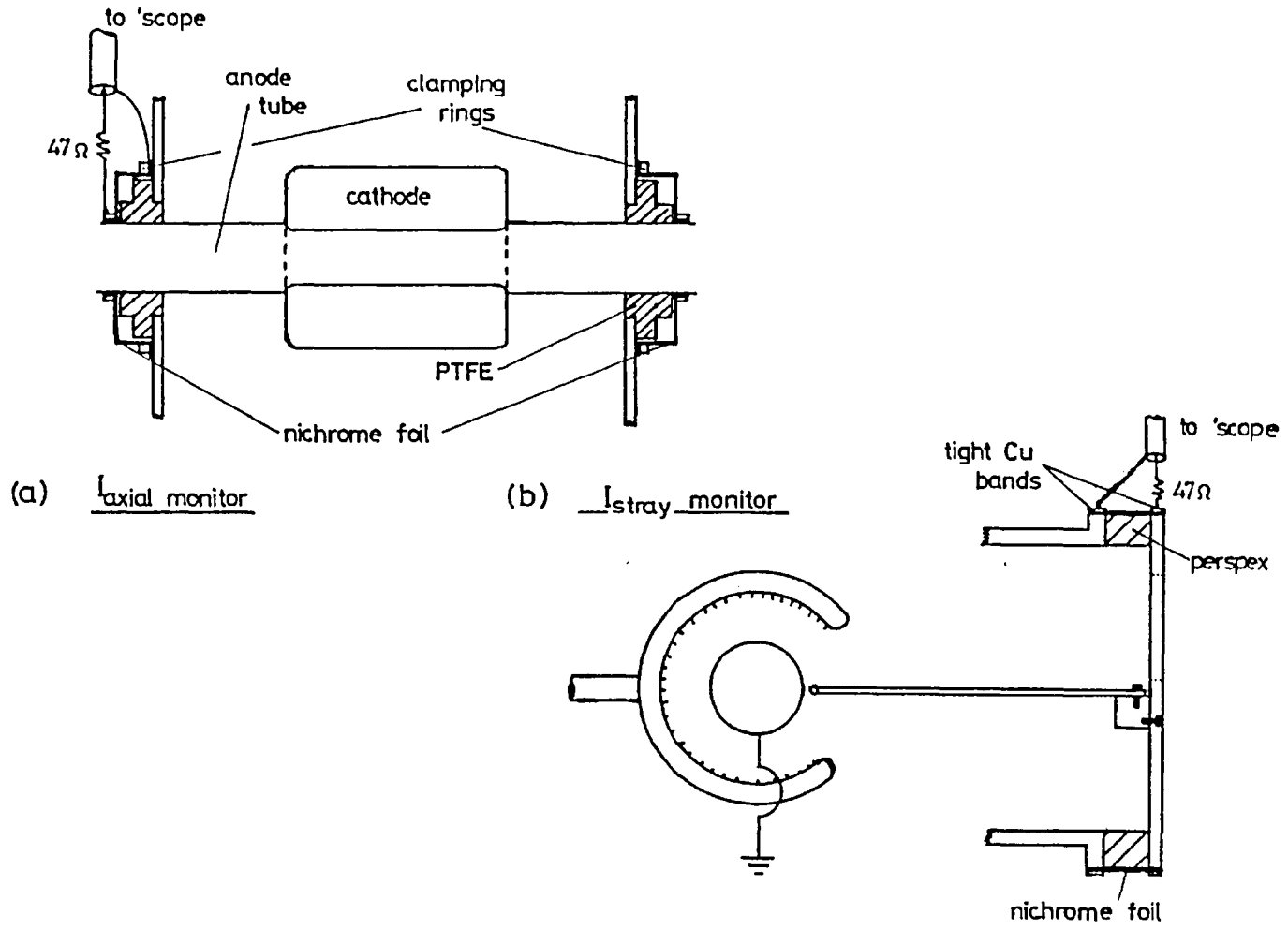


FIGURE 5.10 Construction of (a) axial and (b) stray current monitors. The foil provided excellent electrical shielding to the oscilloscope input.

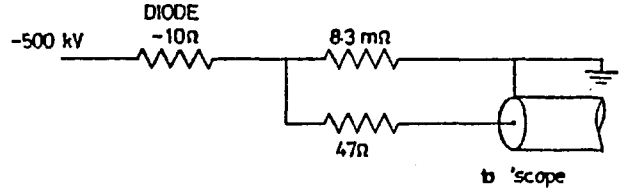


FIGURE 5.12 Circuit of stray current foil monitor.

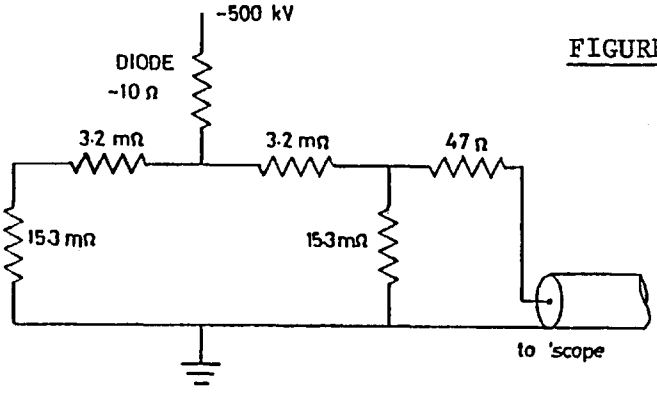


FIGURE 5.11 Circuit of axial current foil monitor.

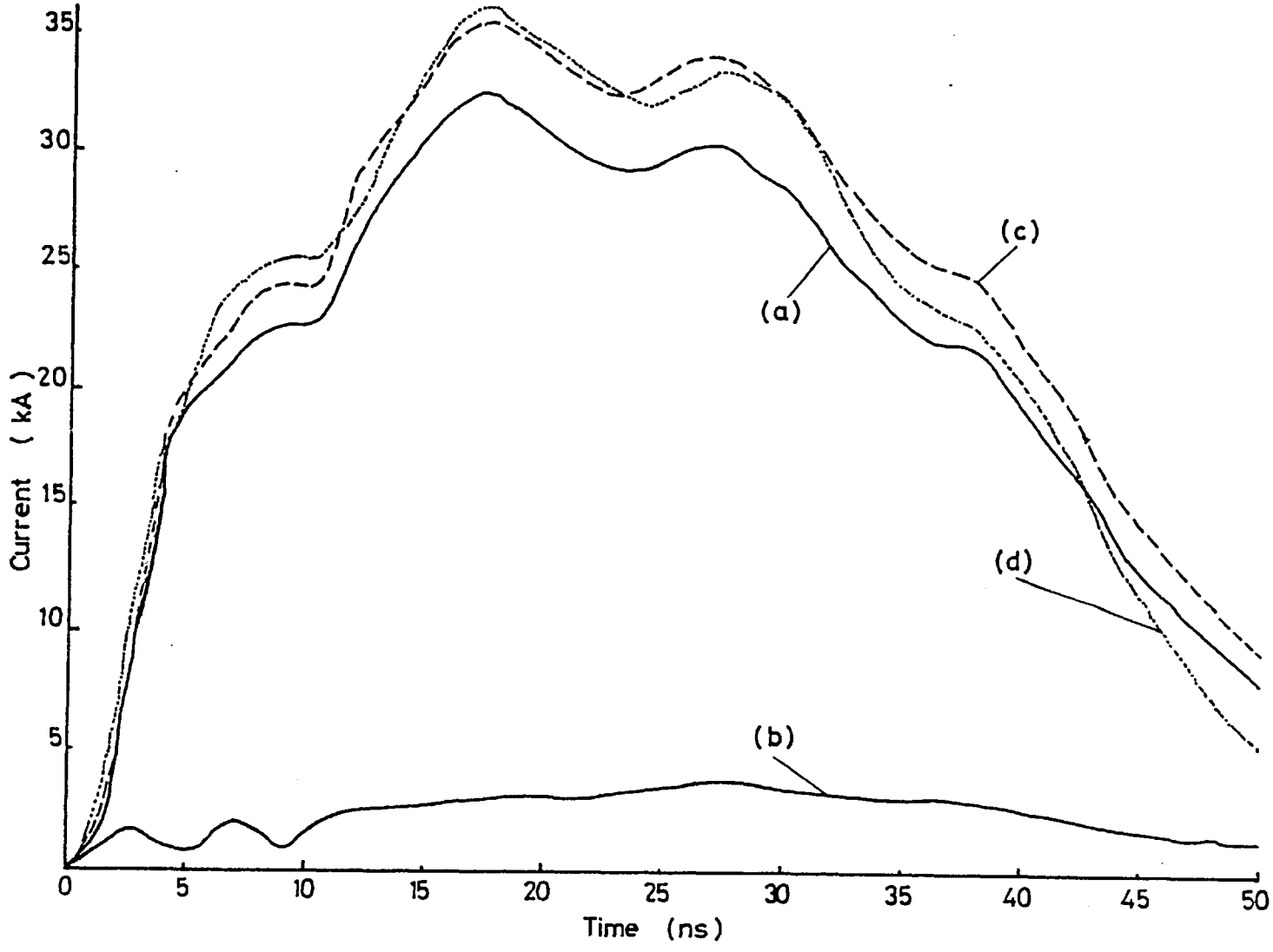


FIGURE 5.13 $I_{axial}$ (a), $I_{stray}$ (b), $I_{axial} + I_{stray}$ (c), $I_{total}$ (d) versus time, case II diode configuration.

5.4.2 Voltage monitoring

Voltage was monitored using a $CuSO_4$ resistive divider in parallel with the e-beam diode. The monitor resistance was 0.95 kΩ with a dividing ratio of 58:1. The construction of the voltage monitor and the equivalent circuit is shown in Fig. 5.14. The output signal of the order of 3 kV was further attenuated with a Physics International high voltage 49x attenuator.

The monitor was calibrated by firing the e-beam into a resistive 9.8 ohm $CuSO_4$ load, comparing the voltage and current. The peak current of 50 kA gives a peak voltage of 490 kV, by Ohm's law, and an attenuation factor of 7300 including the Physics International attenuator. Fig. 5.9(d) shows a typical voltage waveform, obtained using ordinary axial return geometry.

5.4.3 Energy flow in the e-beam diode

We now return to the determination of F in the radial return diode. Energy is calculated from the time integrated power curves, e.g. energy to the anode

$$E_{anode} = \int VI_{axial} dt \qquad 5.3$$

and energy to the plate is given by

$$E_{plate} = \int VI_{stray} dt \qquad 5.4$$

The voltage V was monitored at the same time as $I_{axial}$ and $I_{stray}$, and $I_{total}$ was monitored with the B-probe as a check on accuracy. The onset of diode current was delayed with respect to the voltage pulse by 1 ns (± 1).

Due mainly to uncertainty in the absolute voltage measurement, absolute values of energy are considered accurate to an estimated

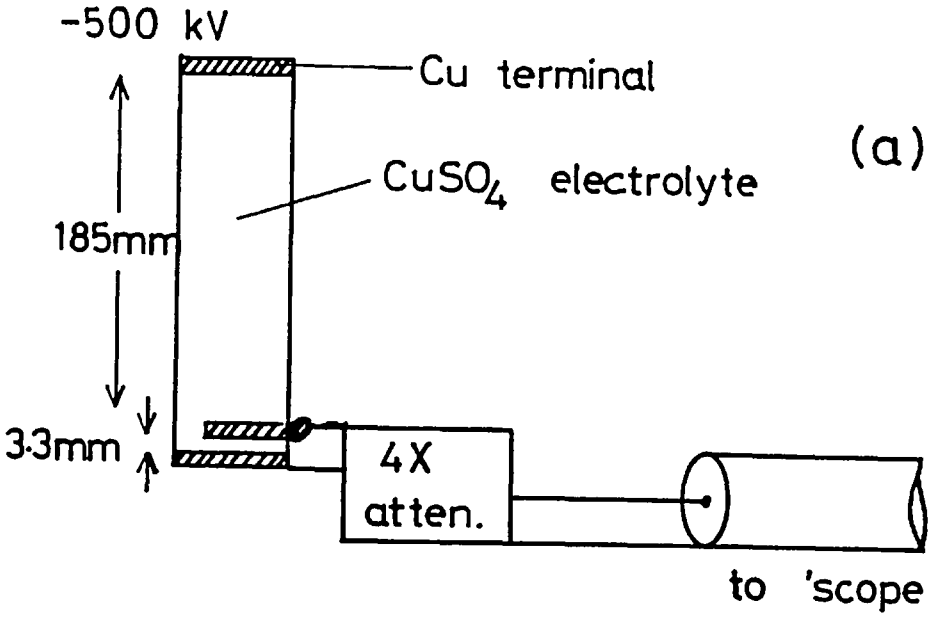


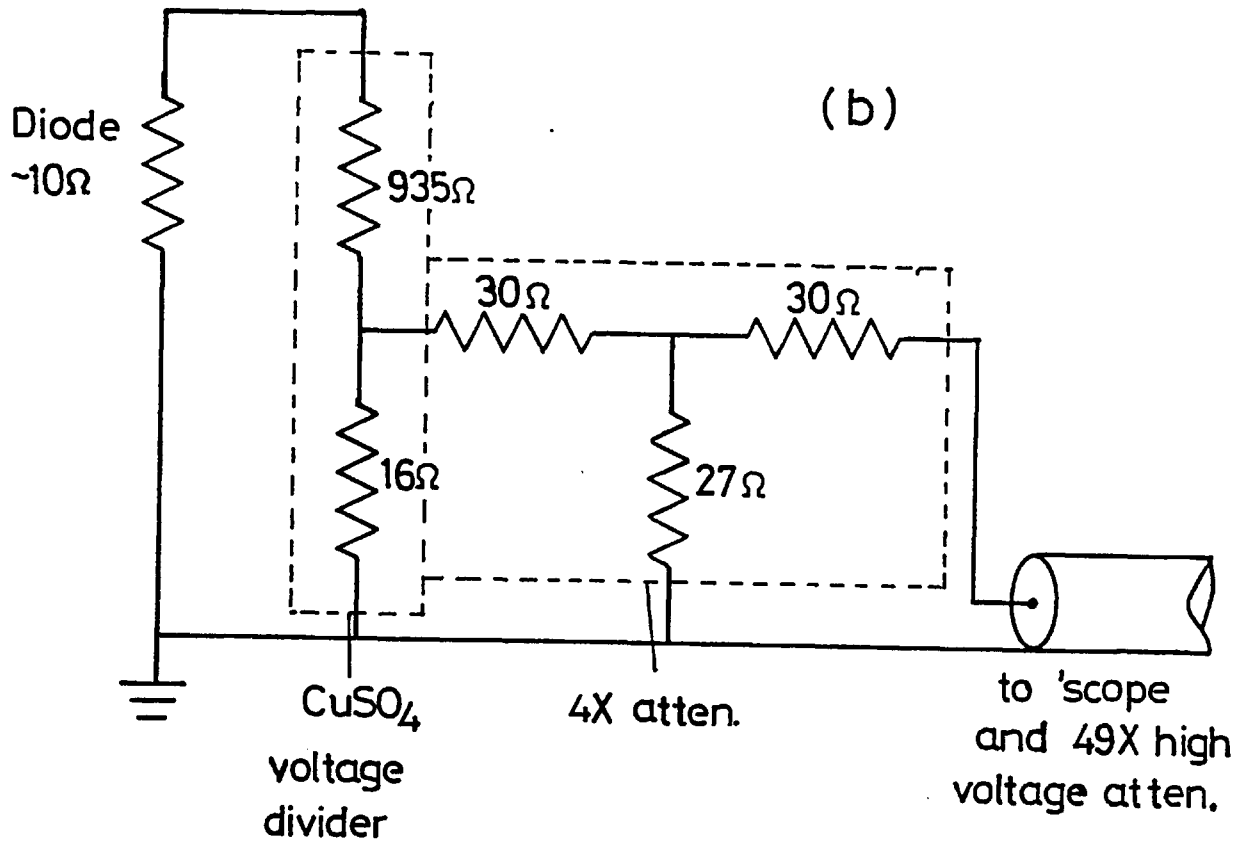


FIGURE 5.14 (a) Construction of voltage monitor, (b) equivalent circuit.

± 20%, although relative values, which are limited in accuracy only by the current measurements, are accurate to ± 10%. Fig. 5.13 is a graph of $I_{axial}$, $I_{stray}$, $(I_{axial} + I_{stray})$ and $I_{total}$, versus time, in a case II diode. The close fit between $I_{total}$ and $(I_{axial} + I_{stray})$ indicates the accuracy of the three independently calibrated current monitors.

Fig. 5.15 is a graph of power versus time in the diode, which yields the values of 380 joules and 29 joules as the total energy dissipated in the diode, $E_{total}$, and energy dissipated on the return plate only, $E_{plate}$, respectively. Therefore 92% (± 1) of the diode energy is dissipated in the anode tube using case II geometry, and the same value F is to be expected in the ordinary radial return geometry (case I).

Losses to the radial return plate would be reduced by increasing the size of the opening in the cathode, although this would reduce the pump uniformity. Alternatively, a higher current would increase $\theta$ and improve e-beam coupling into the laser, using radial return geometry. Increasing the current in the axial return diode would soon lead to catastrophic beam pinch.

$E_{total}$ in radial or axial return diodes was compared by finding the area under the respective $VI_{total}$ curves, and determined to be 300 and 360 joules respectively. Fig. 5.16 shows the voltage, current and power traces for each. The two diode geometries had different impedance characteristics, as shown in Fig. 5.17. The diodes were designed to have a nominal impedance of 10-11 ohms, according to the Langmuir expression for non-relativistic space-charge-limited flow[30], but in practice the impedance varies in a complicated way due to its dependence on $V^{-\frac{1}{2}}$, build-up to space-charge-limited flow, and diode closure. In the absence of a satisfactory theoretical basis, empirical optimization of the diode was not felt to be worthwhile, and was not systematically pursued.

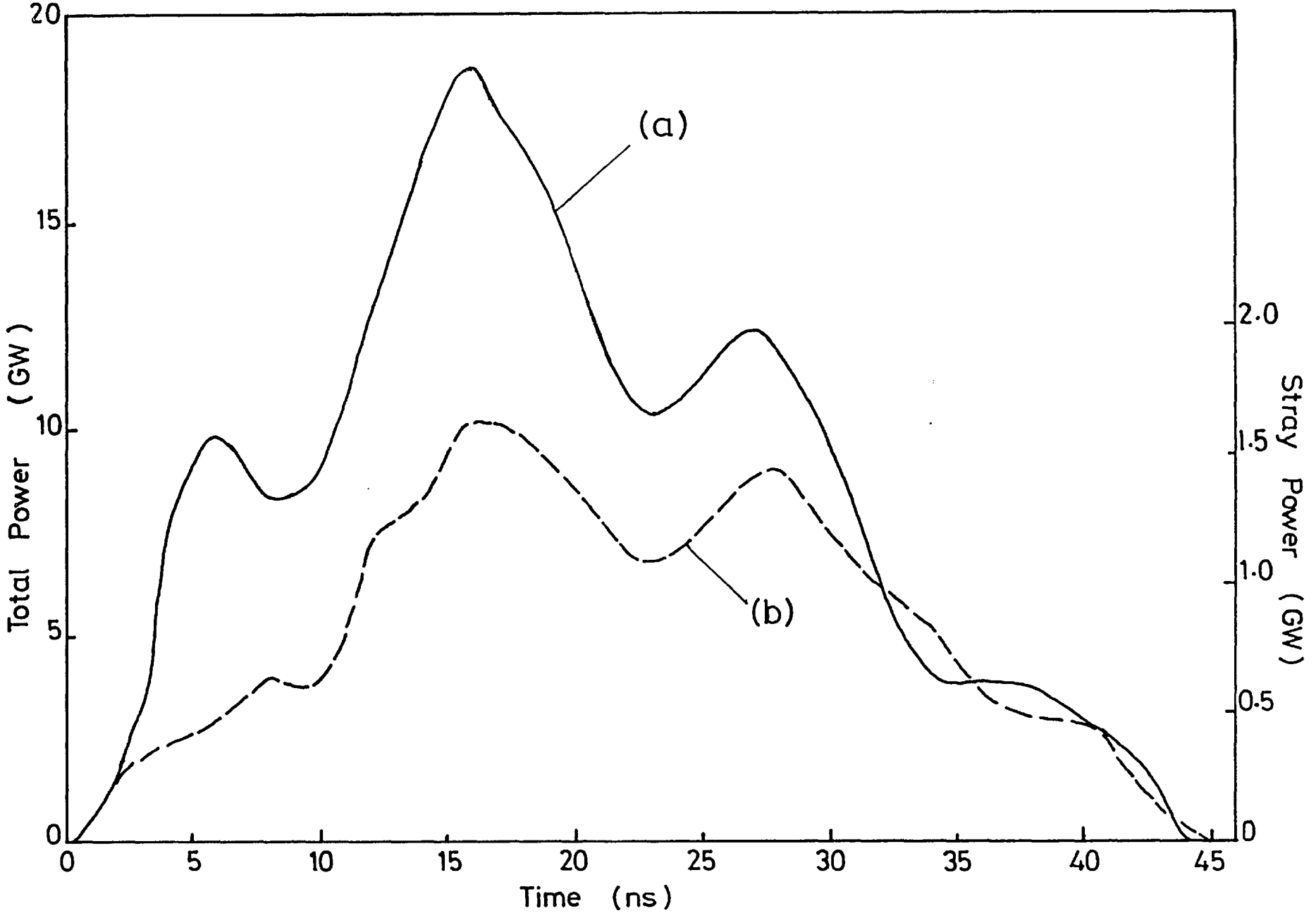


FIGURE 5.15 Total power (a) and stray power (b) in case II diode configuration.

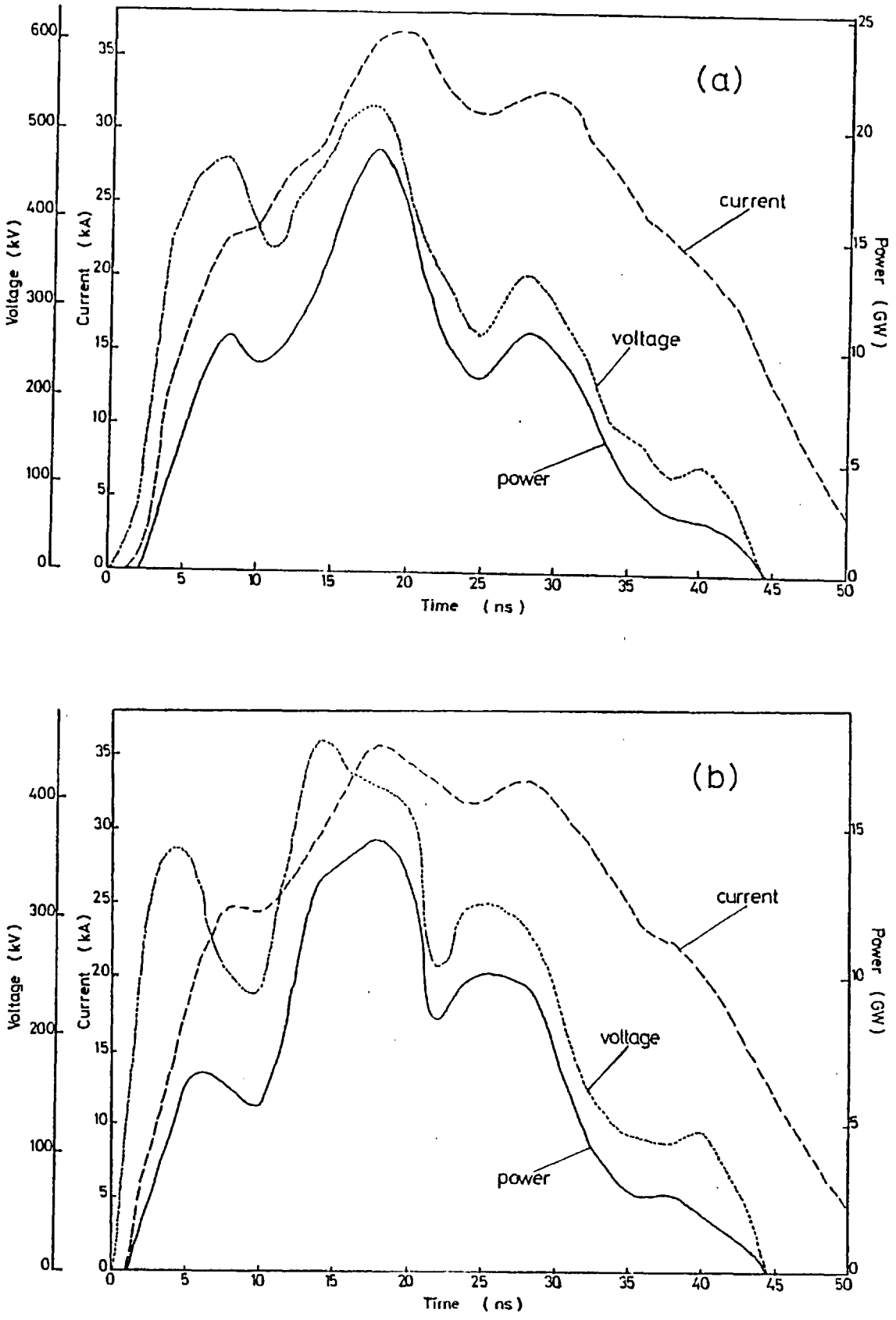


FIGURE 5.16 Current, voltage and power in (a) pure radial current return diode, (b) pure axial return diode.

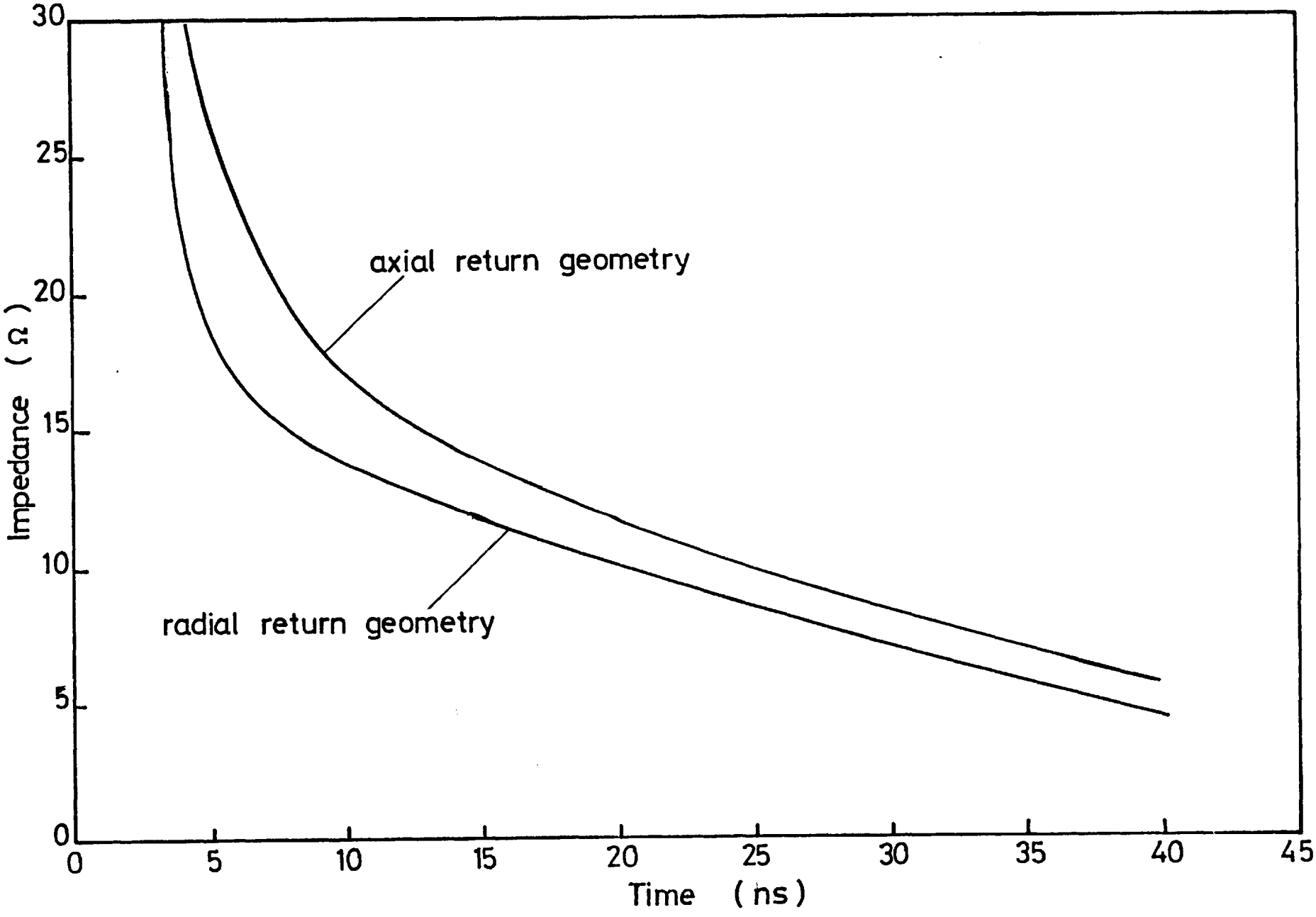


FIGURE 5.17 Impedance in axial and radial return diodes.

## 5.5 Gas Handling

The laser cell was compatible with both KrF and XeCl operation. Gas handling for KrF operation was as described in Chapter 4. XeCl was operated in Ne:Xe:HCl mixtures, typically in the ratio 480:15:1 at 5 bar total pressure, which necessitated the addition of a neon line (BOC research grade) to the gas handling system shown in Fig. 4.2, and the substitution of $NF_3$ and Kr by HCl and Xe respectively. XeCl mixtures were made up directly in the laser cell, which was pre-passivated with $\sim$ 100 torr HCl for several hours. Xenon and HCl purities were rather low (99.5% and 95% respectively), so after filling the evacuated cell with the two gases to just above the required pressure, the vapour was frozen in the liquid-nitrogen-cooled "bomb" and the air impurity pumped away. The bomb was then allowed to warm up to roughly 170$^{o}$K while all the Xe and HCl vapourized and filled the laser cell, after which the bomb was valved off, thus trapping any moisture. The mixture was then topped up with Ne and left for at least $\frac{1}{2}$ hour to mix thoroughly. Low temperatures were monitored to $\pm$ 10$^{o}$K simply by observing the vapour pressure of the Xe or HCl. Fig. 5.18 gives the vapour pressures of gases relevant to the present work. As before, used mixtures were exhausted through the fluorine trap, and the laser cell was purged with argon.

## 5.6 KrF Laser

Ar:Kr:$F_2$ (500:25:1), 4.1 bar, mixtures lased strongly using coaxial pump geometry. Fig. 5.19 shows how energy varied with shot number, using a stainless steel anode, radial current return, and a 42 cm cavity comprising an external, 5.1 cm diameter, 97% reflecting plane multilayer dielectric mirror and a quartz window output coupler. Time

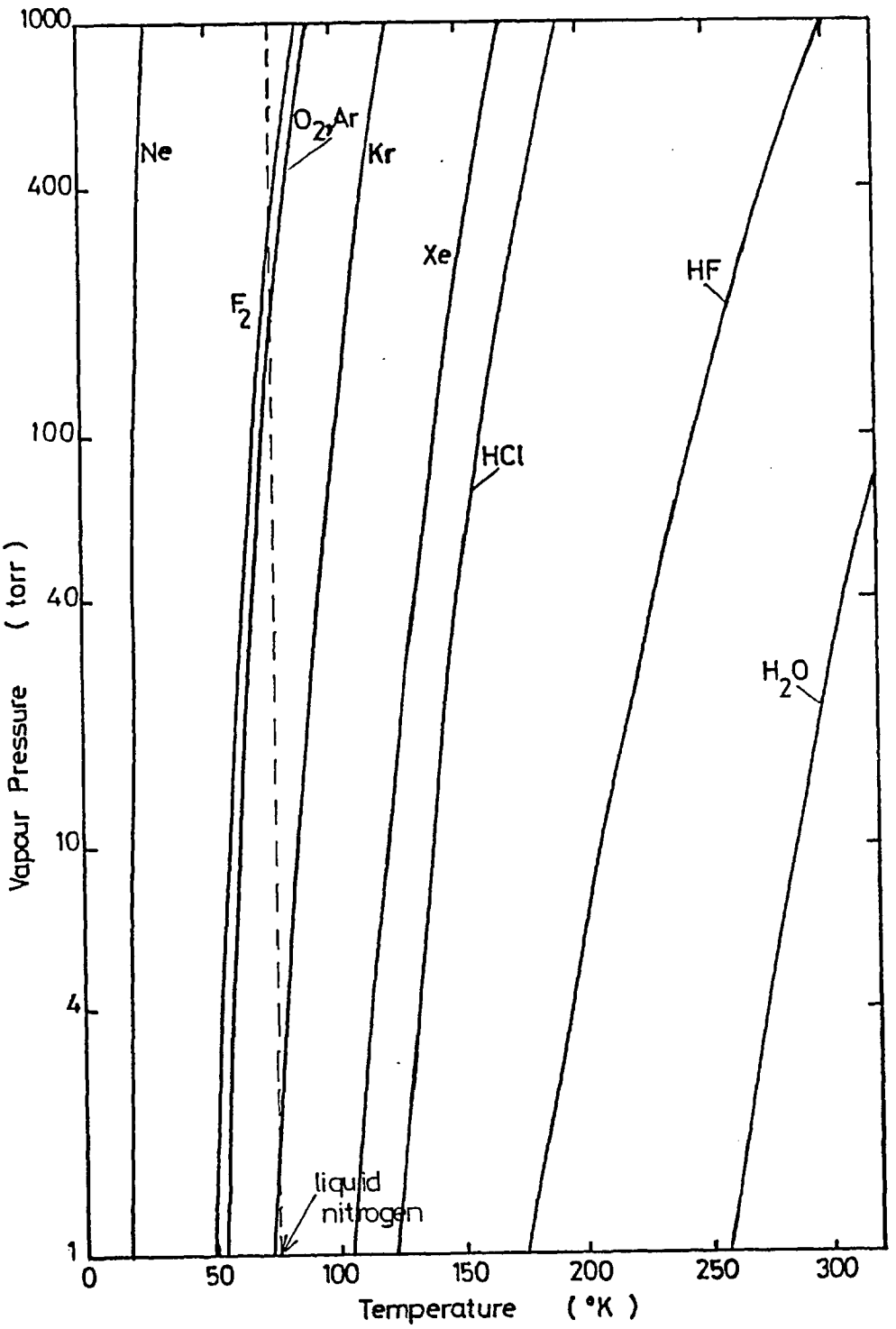


FIGURE 5.18 Vapour pressure curves of various gases.

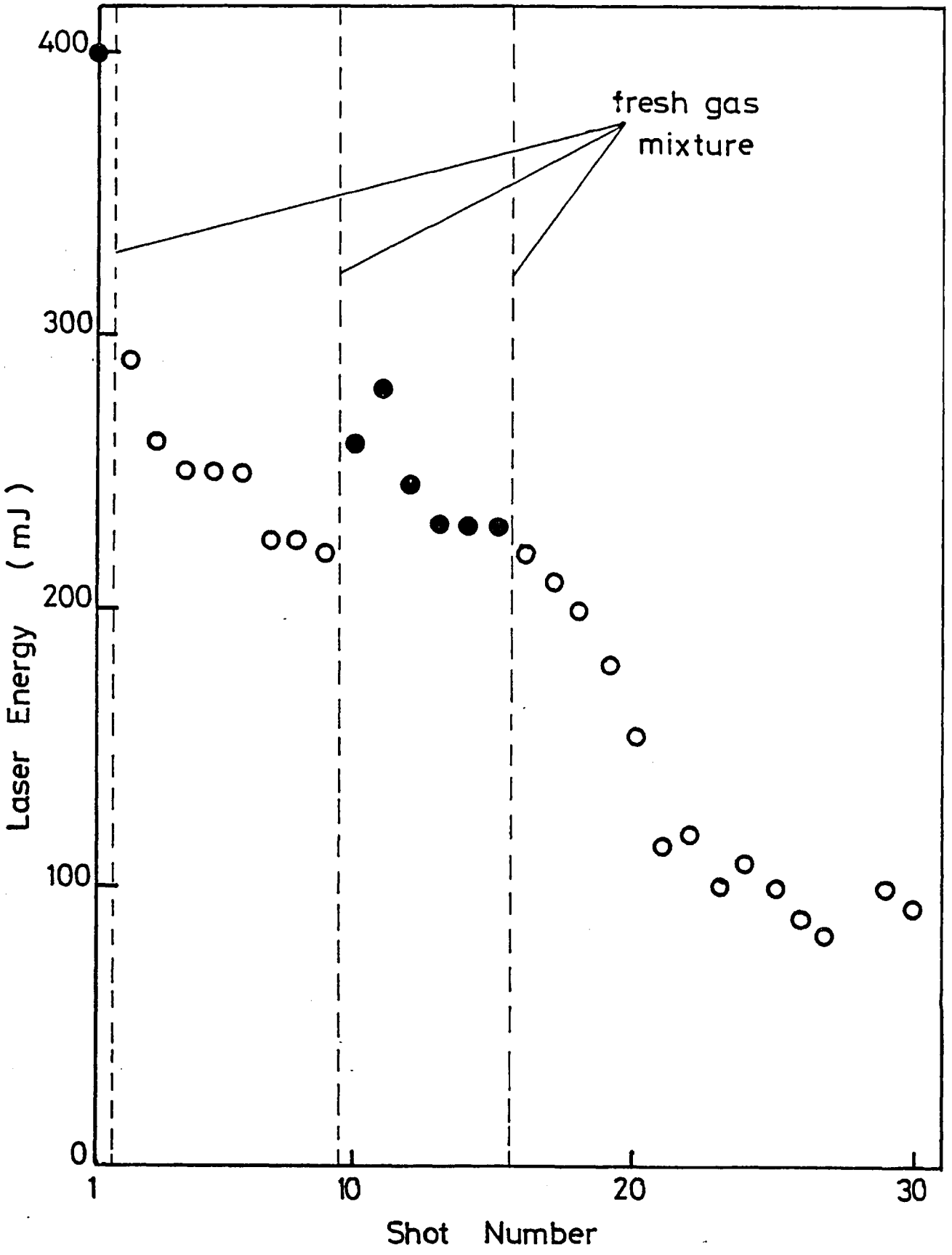


FIGURE 5.19 KrF laser energy versus shot number.

between shots was five minutes, allowing the gas medium to cool completely. As with the transversely-pumped laser, laser energy fell with shot number. The maximum energy under these conditions of 400 mJ in a 10 ns (FWHM) pulse corresponds to a peak power of 40 MW and a laser energy storage density of 2.4 J litre$^{-1}$ in the active medium. Fig. 5.20 shows typical laser pulses, taken at 220 mJ and 80 mJ. Delay between the e-beam and the laser pulse was 25 ns.

A steady drop in energy due to optical damage of the quartz windows was also observed. This was shown by fogging of the Spectrosil B quartz, and falling laser energy in spite of using fresh gas mixtures. The windows possibly suffered radiation damage as well from scattered high energy electrons, a phenomenon previously reported by Heath and Sacher[106]. Finally, in spite of using dry fluorine, the quartz was gradually attacked by the gas. Transmission of a heavily used quartz window at 193 nm and 248 nm was found to be 12% and 60% respectively, observing the emission from Ar:$F_2$ (500:1) and Ar:Kr:$F_2$ mixtures.

Sapphire is resistant to optical and radiation damage[106], as well as to fluorine, and is very hard, and for these reasons is to be preferred to quartz in an e-beam-pumped KrF laser. In addition, the reflectivity of a quartz or sapphire flat at 248 nm is 10% and 20% respectively (assuming incoherent addition from each surface), and the decreased output coupling with sapphire was expected to bring the cavity closer to optimum. Accordingly, the quartz output coupler was replaced by an available 1.7 cm open diameter, 5 mrad wedge sapphire reflector. (Because of the large beam divergence the cavity alignment was not critical, and the small wedge could be ignored.)

The pumping efficiency was improved by replacing the stainless steel anode tube with a titanium one. Fig. 5.21 shows how laser energy

FIGURE 5.20 KrF laser pulses, 20 ns/div. Top - 220 mJ, 10 ns (FWHM); bottom - 80 mJ, 13 ns (FWHM).

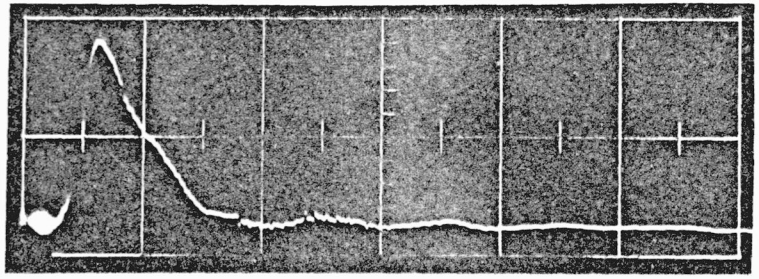

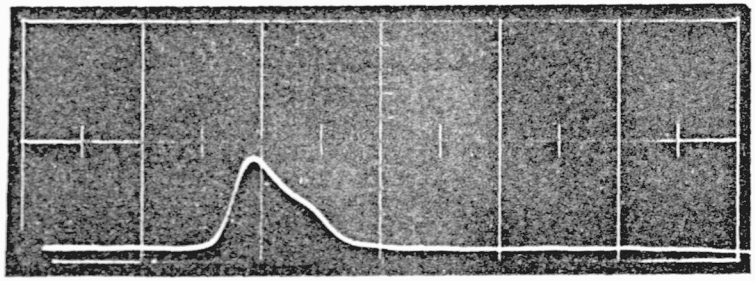

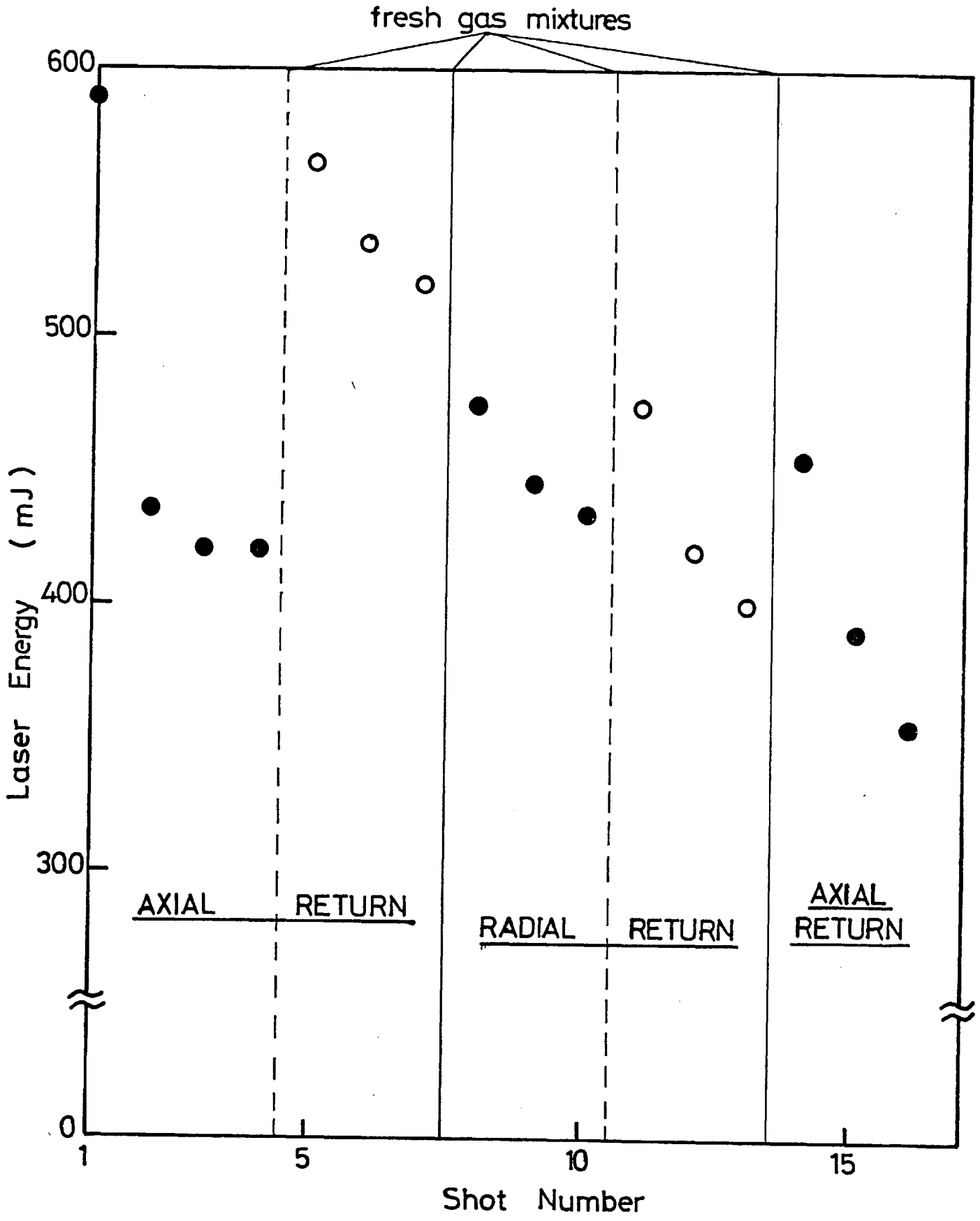


FIGURE 5.21 KrF laser energy versus shot number, showing effect of fresh mixtures and variation of current return geometry.

varied in such a system, as fresh gas mixtures were added, and return geometry was alternated between radial and axial. The main feature is the greatly improved laser energy storage density (by a factor of 7). The maximum energy of 590 mJ corresponds to an energy storage density of 17 J litre$^{-1}$ in the active volume, assuming uniform pumping. Note also that laser energy is comparable using axial or radial return geometry.

The sapphire reflector remained in perfect condition after $\sim$ 50 shots, whereas the other quartz window continued to deteriorate.

## 5.7 XeCl Laser

For XeCl laser action at 308 nm, quartz windows were used. The cavity comprised an external 7.6 cm diameter, $MgF_2$-protected aluminized plane quartz substrate back reflector (R $\sim$ 85%) and a quartz window output coupler. Transmission at 308 nm of the quartz windows was not strongly affected by optical damage or radiation, and sapphire windows were not necessary. Transmission did decrease gradually, mainly due to an easily removed thin greenish deposit.

XeCl laser energy did not drop rapidly with shot number, unlike KrF. In discharge-excited KrF and XeCl mixtures, it has been shown[107] that $F_2$ is gradually depleted by reaction with the cell walls and gas impurities, despite passivation, and forms stable absorbing species, whereas HCl is re-cycled more efficiently after excitation. Fig. 5.22 shows the dependence of laser energy on shot number, using axial return geometry, a stainless steel anode tube, and a Ne:Xe:HCl (625:40:1), 6.1 bar gas mixture. Energy varies by ± 5% around the average trend shown.

Maximum laser energy of 1.35 J in a 20 ns (FWHM) pulse was attained using the same conditions as above, except for the substitution

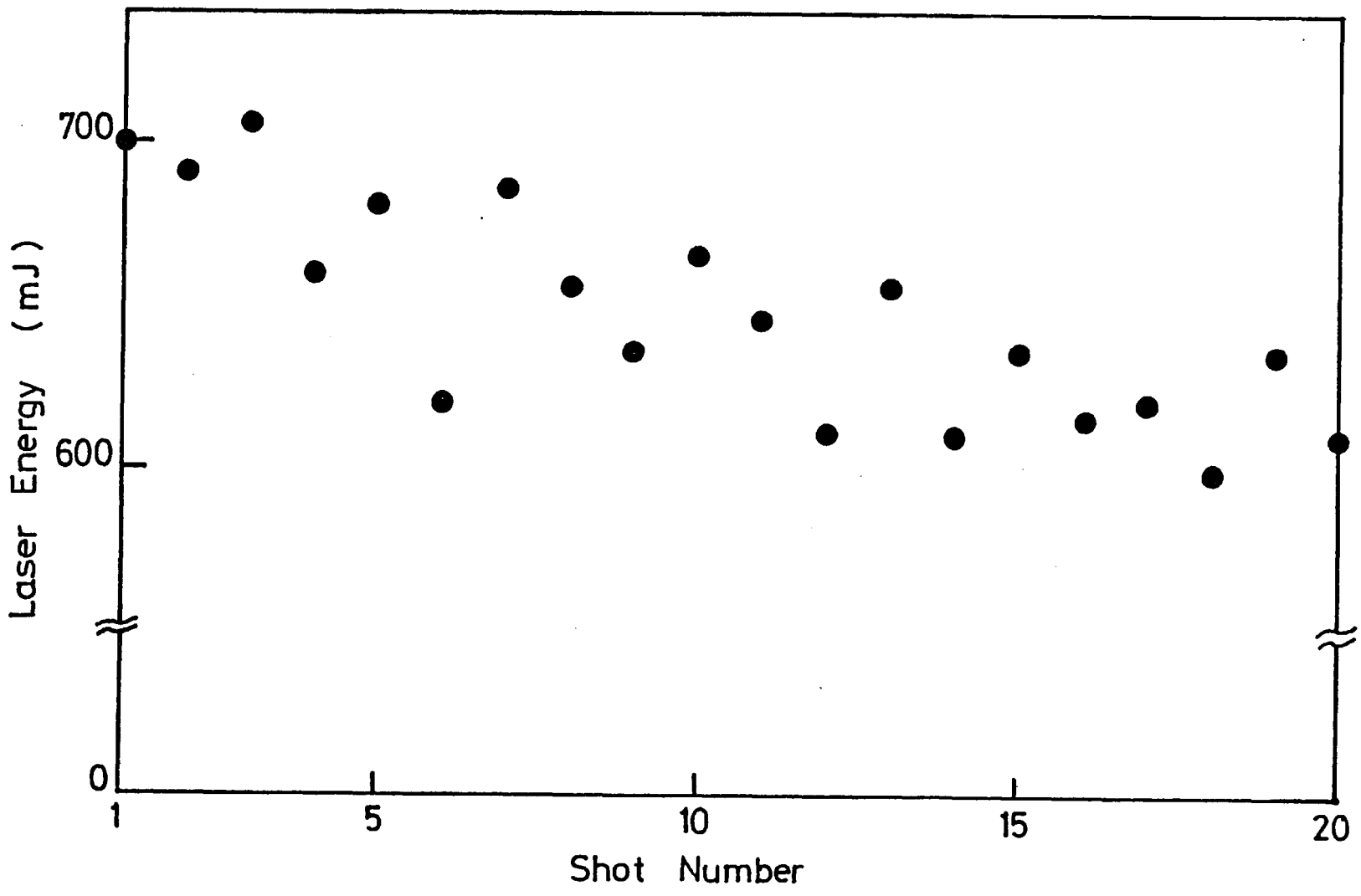


FIGURE 5.22 XeCl laser energy versus shot number.

of a titanium tube. The latter figures correspond to a power of 68 MW and a laser energy storage density of 8 J litre$^{-1}$ in the active medium, about half that attained with KrF. No difference in energy was observed if the output reflectivity was increased by adding an external quartz flat to the cavity, implying that output coupling was near optimum.

Fig. 5.23 shows laser and amplified spontaneous emission waveforms from a 470:30:1, 5 bar mixture, and XeCl fluorescence. The amplified spontaneous emission was recorded after the laser by removing the external optics. To observe fluorescence in the co-axial system, it was necessary to reduce the gain by lowering the gas pressure to 1.4 bar. This had the effect of increasing the time-scale of formation kinetics and quenching of XeCl*. Fig. 5.24 shows the three traces, and the e-beam power, on the same time scale. Relative peak intensities are approximately 10:2:10$^{-4}$ (laser:A.S.E.:fluorescence). Fig. 5.25 compares spectra showing the instrument-limited (1 Å) spectral line narrowing due to amplified spontaneous emission and laser action. The strongest emission at 3080 Å and 3082 Å corresponds to the v'-v" (upper state vibrational level → ground state level) vibronic transitions 0 → 1 and 0 → 2 respectively. The fluorescence spectrum shows the structure expected on a bound-bound transition.

Beam quality and pumping uniformity were checked by burning Polaroid. Fig. 5.26 shows burn marks from focussed and unfocussed beams at a distance of 0.4 m from the output window. The single unfocussed shot (estimated energy 1 joule) using axial return geometry, a titanium anode and 6.1 bar gas pressure, shows good pumping uniformity. The focussed beam beside it was taken using a 20 cm focal length quartz lens placed at the output window. The central burn is approximately 3 mm in diameter, giving a total beam divergence of 15 mrad, assuming beam spread is negligible in the high

FIGURE 5.23 XeCl optical waveforms, 20 ns/div.

Top - laser pulse, 5 bar gas mixture;
middle - A.S.E. pulse, 5 bar gas mixture;
bottom - fluorescence, 1.4 bar gas mixture.

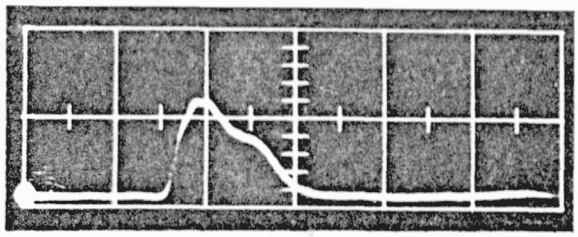

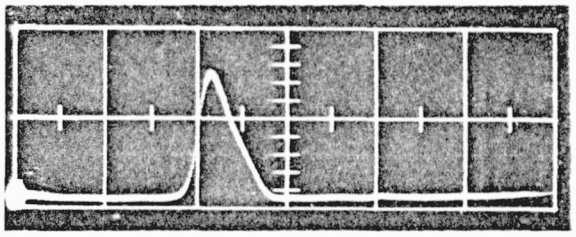

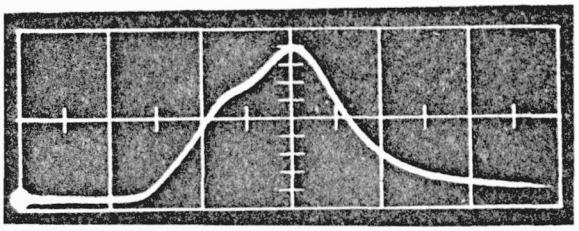

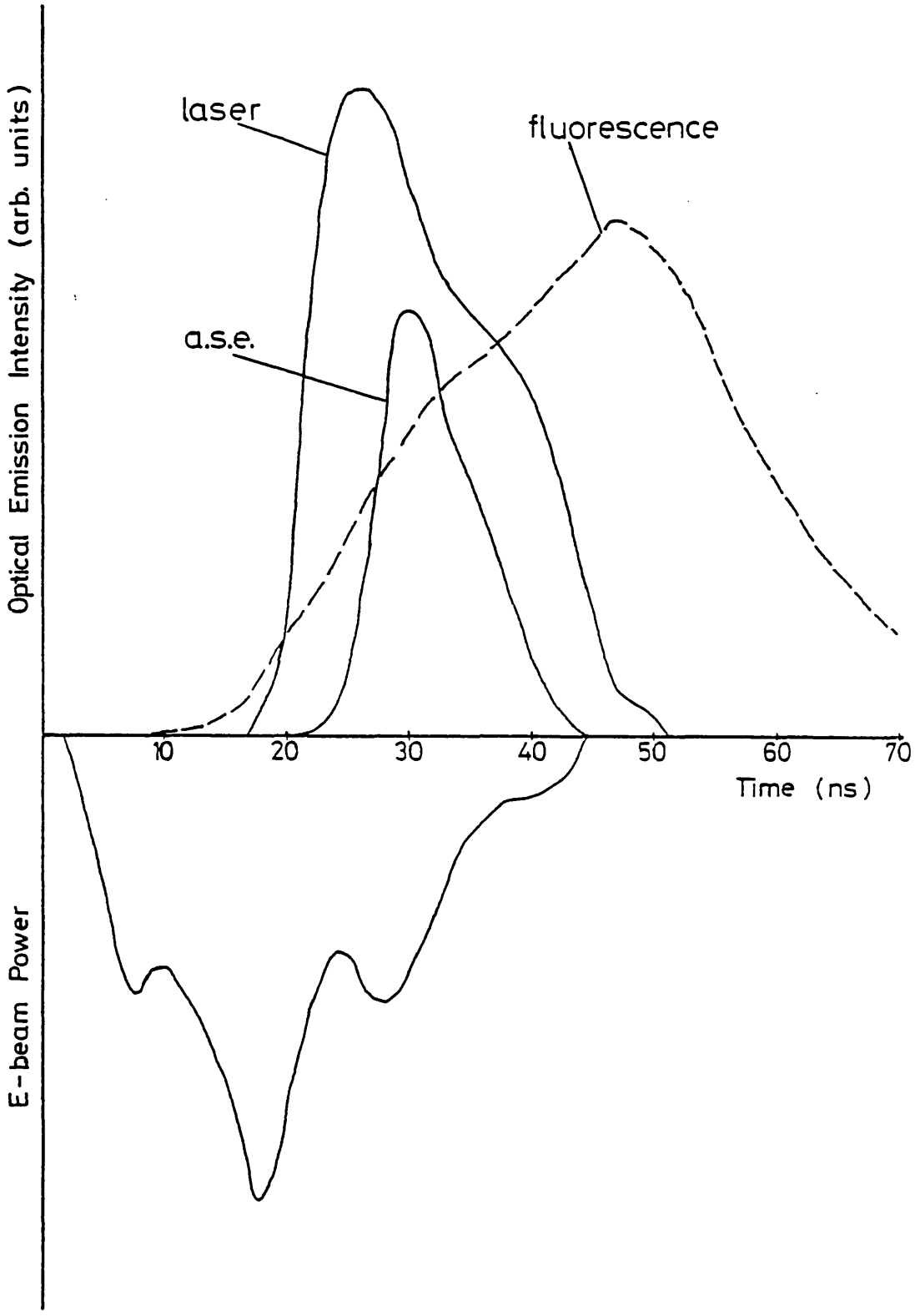


FIGURE 5.24 XeCl optical waveforms and e-beam power.

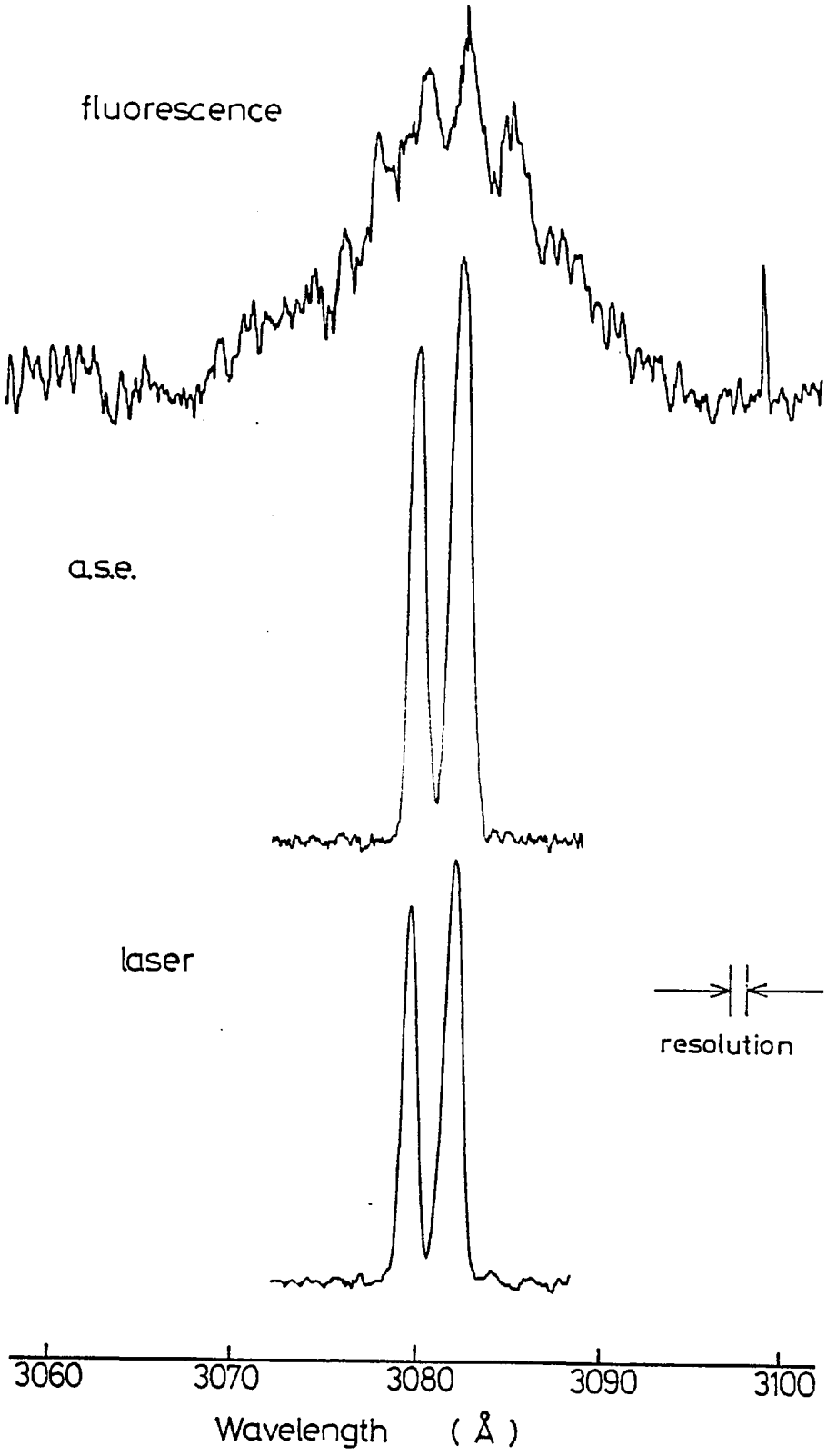


FIGURE 5.25 XeCl laser, A.S.E. and fluorescence spectra.

FIGURE 5.26 XeCl polaroid burn marks, actual size, focussed and unfocussed. Top - axial return current diode; bottom - radial return current diode.

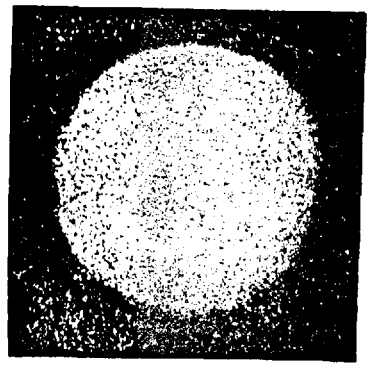

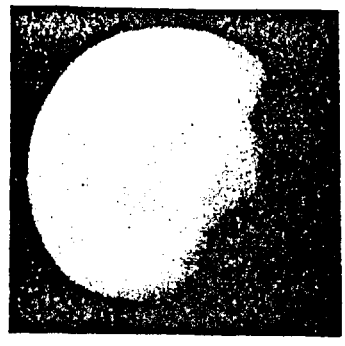

Fresnel number, plane parallel cavity. Using radial return geometry, a stainless steel tube and 6.1 bar gas pressure, the single shot energy of about 400 mJ was too low to give a clear unfocussed burn mark, so we see three shots superimposed in Fig. 5.26. This shows non-uniformity of pumping, greatly exaggerated by the sub-threshold single shot energy in the gap region. Oomen[120] has shown that the non-uniformity is small, in a very similar device. Beam divergence, estimated from the focussed single burn, is again $\sim$ 15 mrad.

### 5.7.1 XeCl gas optimization

The XeCl gas mixture and pressure were optimized from an initial ratio 485:15:1 (0.2% HCl, 3% Xe, 96.8% Ne) at 5.0 bar. First xenon concentration was optimized, followed by HCl at the new xenon concentration, and finally the total pressure was varied, keeping the optimized Ne:Xe:HCl ratio constant. Fig. 5.27 shows how laser energy varied under these conditions. Each energy value is the average of the first two shots taken with a fresh gas mixture. The optimum mixture was found to be 625:43:1 (0.15% HCl, 6.5% Xe, 93.4% Ne) at 6.5 bar.

Strictly speaking, once the "optimum" ratio Xe:HCl has been found, the optimum xenon concentration should be re-determined using the new HCl value. This is shown with the help of Fig. 5.28, a hypothetical contour map of laser energy versus Xe and HCl concentration, at constant pressure (for simplicity). The neon concentration is not an independent variable, and is not considered. Fig. 5.27(a) and (b) merely show two cuts across the contour map, as represented in Fig. 5.28, which approach but do not reach the true optimum. True optimization requires an infinite number of cuts in a 4-dimensional system (the variables are laser energy, Xe and HCl concentrations, and total pressure). In general, more than one local maximum may exist, although there is no evidence to suggest that this is actually the case.

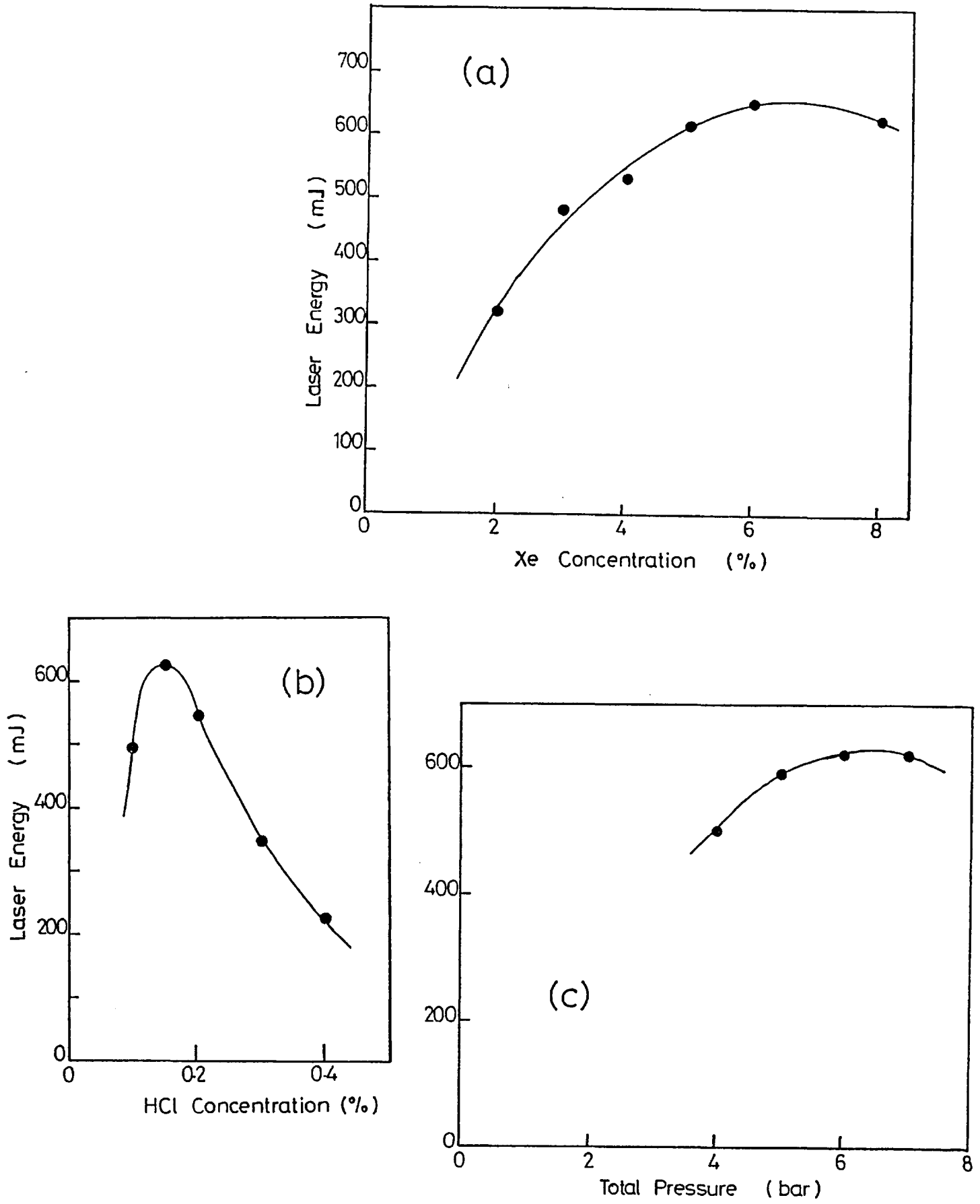


FIGURE 5.27 Gas optimization curves in XeCl: (a) laser energy versus Xe concentration, (b) laser energy versus HCl concentration, (c) laser energy versus total pressure.

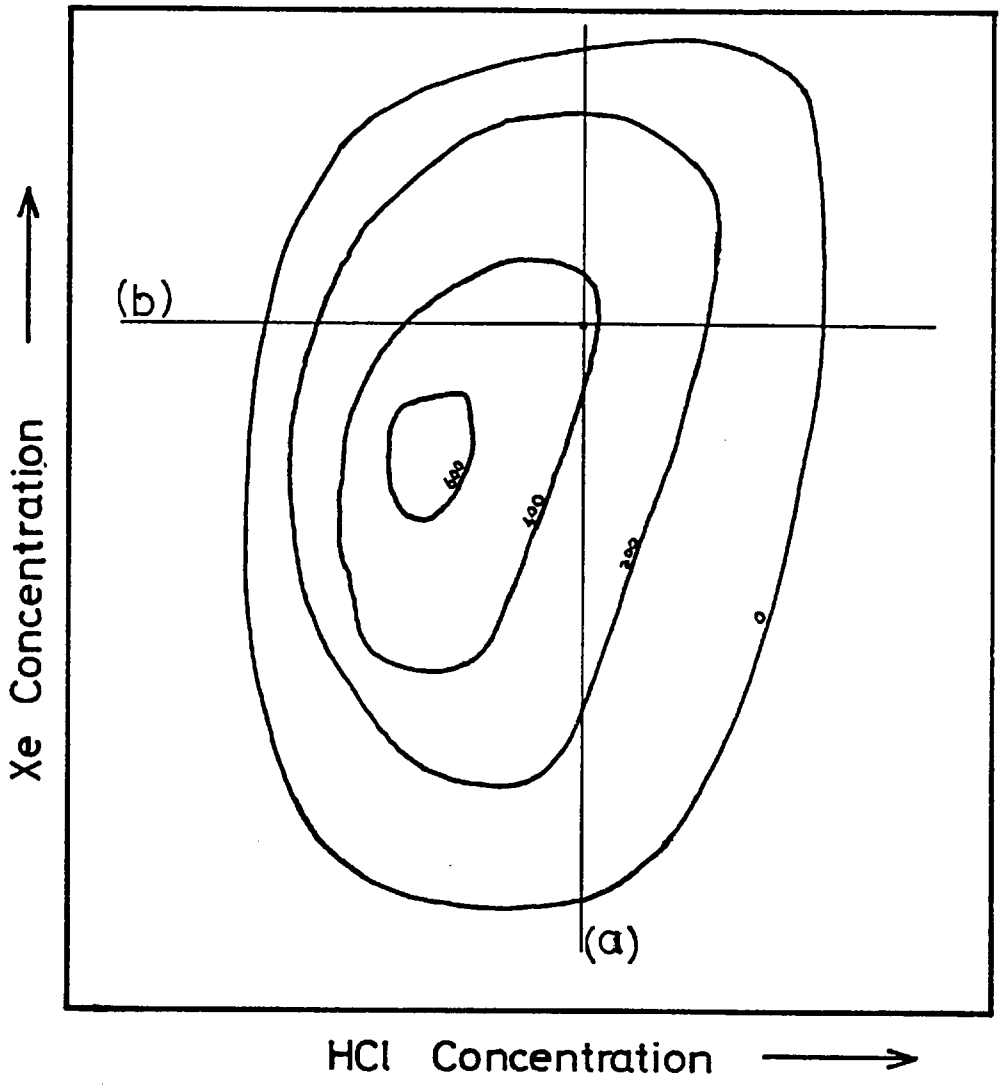


FIGURE 5.28 Hypothetical contour map of laser energy versus Xe and HCl concentrations, at constant pressure.

As one approaches the true optimum, the rate of change of laser energy with the other variables decreases, so in practice a lengthy optimization procedure is not worthwhile, especially if random variations in laser energy are considered.

The optimum working pressure is a function of the gas kinetics and the total stopping power, dependent on the cell geometry and electron energy. The optimum pressure independent of the particular cell geometry is found by optimizing the intrinsic laser efficiency (= laser energy ÷ absorbed e-beam energy). The absorbed energy can be estimated from the stopping power, accurately calculated using a computer, or directly measured with a pressure transducer[112]. Champagne[108] estimated an optimum pressure (in terms of laser efficiency) of 4 bar in a 0.5 μsec, e-beam-pumped XeCl laser operating in a Ne:Xe:HCl mixture (= 1475:15:1) with ∿ 5% laser efficiency. Very similar results were obtained by Rothe[22], using a 200 ns laser.

Other mixtures have produced comparable laser efficiency in e-beam-pumped systems. A 35 ns XeCl laser operated in $Ar:Xe:CCl_4$ (2000:50:1) at 4 bar had a specific laser energy of 10 J litre$^{-1}$ and a laser efficiency of ∿ 4%[109]. The energy of a 30 ns KrF laser was increased by 50% using a mixed argon-neon diluent in a Ne:Ar:Kr:NF (= 4180:1140:75:1) mixture at 7.1 bar[110], with a laser efficiency of ∿ 6%. It is likely that further significant improvements will be made with increased understanding of the gas kinetics.

## 5.8 Conclusion

It has been shown that short pulse, high excitation rate (∿ 15-30 MW cm$^{-3}$) KrF (10 ns) and XeCl (20 ns) lasers can operate with intrinsic efficiencies of ∿ 2%, assuming that ∿ 70 joules is absorbed by the active medium in the full aperture XeCl laser, and

$\sim$ 30 joules in the smaller diameter sapphire output coupler KrF laser, using the titanium anode (rough estimates, applying equation 2.1 and assuming that the average current density j in the XeCl active volume is half that in the smaller KrF active volume, with respective values of $\sim$ 500 amp $cm^{-2}$ and $\sim$ 1000 amp $cm^{-2}$). This is a rather low value, due to quenching of the upper laser manifold during the laser build-up time. Table 5.1 compares these results with those of Edwards *et al.*[112], who measured the intrinsic efficiency of optimized KrF and XeCl lasers in a 60 ns e-beam-pumped system, having an excitation rate of 1.5 MW $cm^{-3}$. The peak power efficiency, defined as the peak laser power divided by the peak pump power, is greater than the intrinsic efficiency because of the build-up time, and is the efficiency of a saturated amplifier under the same pumping conditions. In both cases the peak power efficiency of KrF is twice that of XeCl. It is difficult to compare absolute values of efficiency with other workers without an experimental determination of deposited energy in the gas medium in the present work. However, it is likely that the high excitation rate in this case has reduced the efficiency compared to the values of Edwards *et al.*, or to Tisone[113], the latter measuring an intrinsic efficiency of 11% in a 50 ns e-beam-pumped KrF laser at an excitation rate of 7 MW $cm^{-3}$.

In addition, the usefulness of the radial return diode has been demonstrated. The current and voltage characteristics of the co-axial diode described here place it in a regime falling between optimal use of either axial or radial current return. The radial return diode can be used to advantage wherever high currents ($\gtrsim$ 40 kA) are required in a relatively compact system, avoiding the need for diode modularization or very large diameter anode tubes and optics.

TABLE 5.1 Characteristics of KrF and XeCl lasers

| Laser | Reference | Output energy (J) | Intrinsic efficiency (%) | Pulsewidth (FWHM) (ns) | Peak excitation rate averaged over laser volume (MW $cm^{-3}$) | Peak power efficiency (%) |
|---|---|---|---|---|---|---|
| KrF | *112* | 3.6 | 11 | 37 | 1.5 | 15 |
| | *113* | 80 | 11 | 40-50 | 7 | |
| | present work | 0.6 | 2 | 10 | 30 | 6 |
| XeCl | *112* | 1.4 | 4 | 30 | 1.5 | 7 |
| | present work | 1.4 | 2 | 20 | 15 | 3 |

CHAPTER 6

# GROUND STATE DISSOCIATION OF XeCl

## 6.1 Introduction

One of the attractive features of the rare gas halide lasers is the repulsive ground state, which makes population inversion on the B-X transition automatic when the upper level is populated. Two exceptions are XeCl and XeF, which are bound in the ground state by 281 $cm^{-1}$ [37] and 1065 $cm^{-1}$ [38] respectively, the former molecule supporting an estimated[37] 20 bound vibrational levels. At room temperature and in equilibrium, most of the molecules will be dissociated into the constituent rare gas and halogen atoms[114], and in a real system the halogen atoms recombine, driving the dissociation reaction below completely to the right

$$XeCl(X) + M \rightleftharpoons Xe + Cl + M \qquad (1)$$

where M is a third body. In a XeCl laser, the finite lifetime of the lower laser level allows ground state population to build up and reduce the population inversion, in a process referred to as "bottle-necking".

Fig. 6.1 is a potential energy diagram for XeCl, showing the vibrational energy levels in the B and X states. Lasing occurs on the v'-v" (B-X) vibronic transitions 0-1 and 0-2. Laser action in XeF occurs on the 0-3, 0-2 and 1-4 transitions. In both cases, the lower laser level lifetime is dependent on the dissociation rate of the ground state as a whole. Vibrational relaxation in the ground state distributes population from the lower laser level throughout the vibrational manifold via collisions with atoms or molecules. If the rate of vibrational relaxation is fast compared to the dissociation rate, the different vibrational

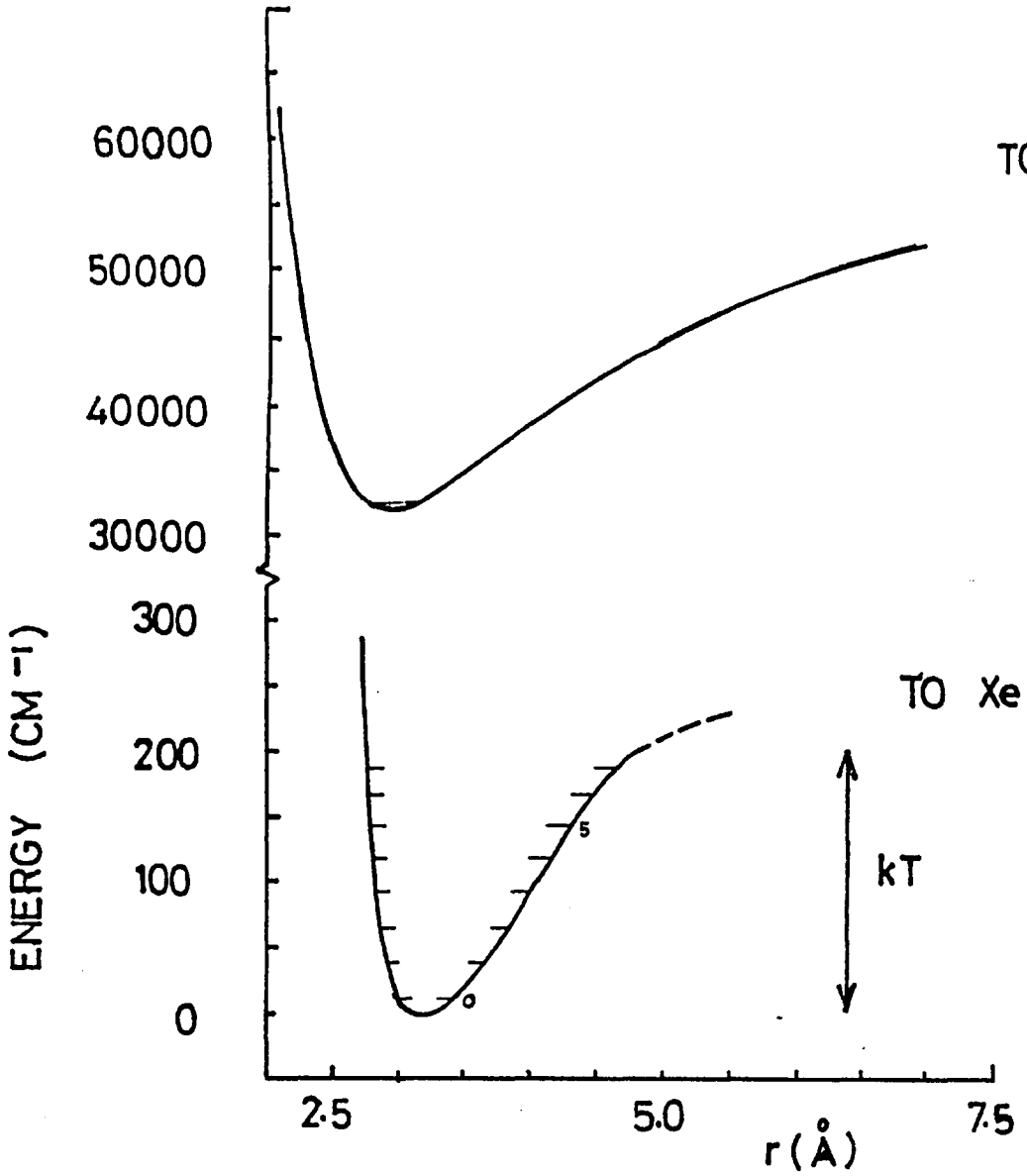


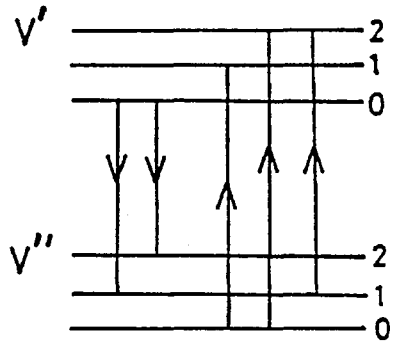


| v'-v'' | λ (Å) |
|---|---|
| 0-1 | 3079.6 |
| 0-2 | 3082.1 |
| 1-0 | 3058.7 |
| 2-0 | 3040.8 |
| 2-1 | 3043.3 |

FIGURE 6.1 Potential energy diagram of XeCl, showing vibronic transitions.

levels reach thermal equilibrium with each other. Fulgham[115,116] studied the population decay from the low-lying XeF(X) vibrational levels, and found[116] that vibrational relaxation in a He buffer was sufficiently fast to equilibrate the vibrational levels. As population was removed from the ground state by collisional dissociation, vibrational relaxation kept the vibrational level populations in quasi-equilibrium so that each level decayed at the same rate. Rokni[114] measured the rate of decay of population from the $v'' = 3$ level in XeF, operating in a Ne buffer, and calculated the loss of efficiency due to bottle-necking. The extraction efficiency of the laser, $\eta_{ext}$, is reduced by a calculated factor $\eta_L$ (see equation 3.13) equal to 0.44 at 300°K, and 0.74 at 500°K, and therefore an improvement in $\eta_{ext}$ is expected at higher temperatures. This had been observed earlier[117], but was only partly accounted for by the increased rate of dissociation of the ground state at higher temperatures. Additional factors are the improved energy extraction from higher lying vibrational levels in the B state, and improved mixing between the B and C states at higher temperatures[118].

In the present work, the decay of population from the $v'' = 0,1,2$ levels of XeCl was measured[33] in e-beam-pumped mixtures of Ne, Xe and HCl typical of the XeCl laser. The results agree well with those of Waynant[119], who has also made this measurement. In addition, the time-resolved gain in the gas cell was determined.

## 6.2 Theory

The ground state of XeCl can be represented by a simple two-level model (see Fig. 6.2). Level 2 represents the lower laser levels ($v'' = 1,2$) and level 1 represents all the other vibrational levels ($v'' = 0,3,4,\ldots 20$). The rate $\omega_{21}$ ($sec^{-1}$) is the average rate of vibrational relaxation from level 2 to level 1. By the principle of detailed balance, for a system in

thermal equilibrium the following equality must hold

$$N_1\omega_{12} = N_2\omega_{21} \qquad 6.1$$

where $N_1$, $N_2$ are the number densities of population in levels 1 and 2, respectively, and $\omega_{12}$ is the rate of vibrational relaxation from level 1 to level 2. Therefore, the rate $\omega_{12}$ is given by

$$\omega_{12} = f\omega_{21} \qquad 6.2$$

where

$$f = N_2/N_1 \qquad 6.3$$

and the number densities in 6.3 are given by the Boltzmann distribution. For the model chosen, $f \sim 0.2$, estimated using data from Tellinghuisen[122]. The rate of collisional dissociation $\omega_D$ is assumed equal for each level. Because of the shallowness of the potential well, this is a fairly good assumption, and in any case the model is insensitive to differences in $\omega_D$ between the levels.

The rate equations for the populations in levels 1 and 2 at time t are given by

$$d/dt\ N_1(t) = N_2(t)\omega_{21} - N_1(t)(\omega_{12} + \omega_D) \qquad 6.4$$

$$d/dt\ N_2(t) = N_1(t)\omega_{12} - N_2(t)(\omega_{21} + \omega_D) \qquad 6.5$$

Exact solutions to these, assuming $N_1(0) = 0$, $N_2(0) = N$, are given by

$$N_1(t) = \frac{N}{1+f}\left[e^{-\omega_D t} - e^{-(\omega_{21} + \omega_{12} + \omega_D)t}\right] \qquad 6.6$$

$$N_2(t) = \frac{N}{1+f}\left[fe^{-\omega_D t} + e^{-(\omega_{21} + \omega_{12} + \omega_D)t}\right] \qquad 6.7$$

If $\omega_{21} >> \omega_D$, $t > \omega_{21}^{-1}$, equations 6.6 and 6.7 reduce to

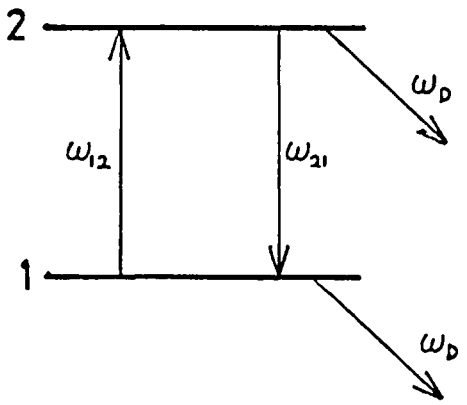


FIGURE 6.2 Two-level model of XeCl ground state.

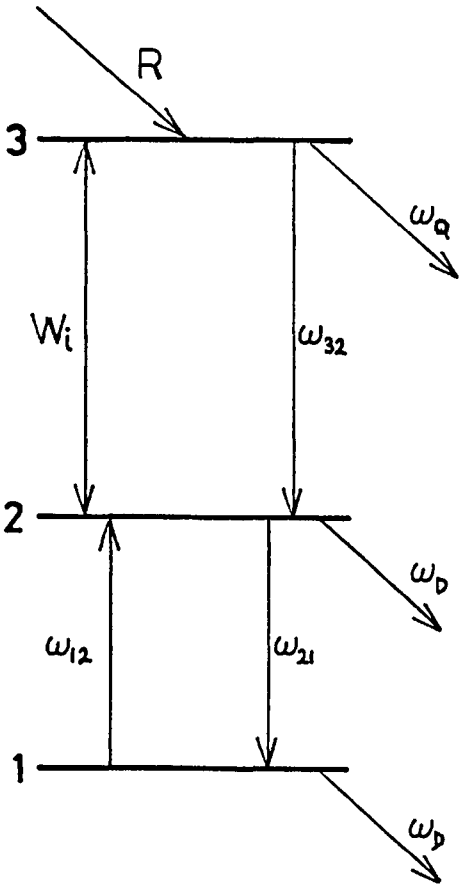


FIGURE 6.3 Three-level model of XeCl laser.

$$N_1(t) = \frac{N}{1+f} e^{-\omega_D t} \qquad 6.8$$

$$N_2(t) = \frac{fN}{1+f} e^{-\omega_D t} \qquad 6.9$$

Equations 6.8 and 6.9 imply that the population in each level follows a Boltzmann distribution, and that each decays at the same rate, $\omega_D$. The above model approximates to the situation in the present work, where a short pulse dumps population into the ground state, which then decays. $\omega_D$ was determined by following the decay of population in the ground state manifold after stimulated emission had ceased.

Next we derive the necessary condition for population inversion in a steady-state system. Fig. 6.3 illustrates the model taking the upper laser level (labelled 3) into account. R is the rate of pumping into level 3, $\omega_{32}$ is the rate of spontaneous emission, $\omega_Q$ is the rate of collisional quenching of level 3, and $W_i$ is the induced or stimulated rate of transitions between levels 3 and 2 due to the photon flux in the cavity. The rate equations describing the population in each level are given by

$$d/dt\ N_3(t) = R - [N_3(t) - N_2(t)]W_i - N_3(t)(\omega_{32} + \omega_Q) \qquad 6.10$$

$$d/dt\ N_2(t) = [N_3(t) - N_2(t)]W_i + N_3(t)\omega_{32} + N_1(t)\omega_{12} - N_2(t)(\omega_{21} + \omega_D) \qquad 6.11$$

$$d/dt\ N_1(t) = N_2(t)\omega_{21} - N_1(t)(\omega_{12} + \omega_D) \qquad 6.12$$

In the steady state $\dot{N}_3 = \dot{N}_2 = \dot{N}_1 = 0$, and solving for $N_1$, $N_2$ and $N_3$ under this condition yields the following expression for the population inversion

$$N_3 - N_2 = N_3[1 - (W_i + \omega_{32})/(W_i + \beta)] \qquad 6.13$$

where

$$\beta = \omega_{21} + \omega_D - \omega_{21}\omega_{12}/(\omega_{12} + \omega_D) \qquad 6.14$$

and

$$N_3 = R\left[\left(\frac{\beta - \omega_{32}}{W_i + \beta}\right)W_i + \omega_{32} + \omega_Q\right]^{-1} \qquad 6.15$$

Inspection of equation 6.13 shows that a necessary condition for population inversion according to this model is

$$\beta > \omega_{32} \qquad 6.16$$

$\beta$ increases monotonically with $\omega_{21}$ and $\omega_D$, and hence with pressure or temperature, whereas $\omega_{32}$ is a fixed property of the molecule. The maximum value of $\beta$ as $\omega_{21} \to \infty$ is given by

$$\beta_{max} = \omega_D(1 + 1/f) \qquad 6.17$$

The results of the work described in this chapter and of other workers[114,116] show that condition 6.16 is satisfied in XeCl and XeF (applying the same model to the latter, where $f \sim 0.04$) operating at a pressure of a few bar. Therefore there is no possibility of XeCl or XeF laser action terminating prematurely due to bottle-necking in the ground state.

Assuming that dissociation is due to two body collisions of XeCl(X) with Ne, Xe and HCl molecules (reaction (1)), $\omega_D$ can be written

$$\omega_D = k_{Ne}[Ne] + k_{Xe}[Xe] + k_{HCl}[HCl] \qquad 6.18$$

where [ ] denotes the number density ($cm^{-3}$) of the bracketed molecule. The rate $k_{Xe}$ ($cm^3$ $sec^{-1}$) was determined by varying the xenon concentration [Xe] and observing the varation in $\omega_D$, keeping [Ne] and [HCl] constant. A linear fit was made to a plot of $\omega_D$ versus [Xe], giving a slope $k_{Xe}$.

## 6.3 Experimental Method and Apparatus

The lifetime of ground state XeCl can be determined directly through time and spectrally resolved measurements of absorption on selected vibronic transitions, following e-beam excitation of Ne, Xe, HCl gas mixtures typical of XeCl lasers. If the upper state is depopulated and background absorption is small, the absorption coefficient at a wavelength corresponding to a v'-v" transition is directly proportional to the population in v". The characteristic time for the absorption to decay is a direct measure of $\omega_D^{-1}$, if vibrational relaxation is relatively fast. By varying the probe wavelength, the gain or absorption on different v'-v" transitions can be followed.

The frequency-doubled output from a tunable mode-locked dye laser was used to probe the gas medium. After double-passing through the XeCl cell, the dye laser beam was detected by a fast photodiode, and the signal compared to part of the beam which did not pass through the cell, thus allowing calculation of gain or loss in the cell at different times. Fig. 6.4 is a schematic of the experimental set-up. The following sections describe the experimental apparatus and method in detail.

### 6.3.1 Dye laser

A flash-lamp-pumped, mode-locked Rhodamine 6G dye laser, tuned by two intra-cavity Fabry-Perot etalons, was used to probe the XeCl cell. Fabry-Perot plate separations were 5 μm and 50 μm. Flashlamp output was 200 joules. The mode-locking dye was DODCI dissolved in ethanol, contained in a 3 mm thick cell in contact with the back mirror, which was a dielectric broadband maximum reflector. Output mirror reflectivity was $\sim$ 50%. Fig. 6.5 is a schematic diagram of the dye laser.

Estimated pulse width was 10 psec and pulse separation was 6.2 ns. Optimum output from Rhodamine 6G dissolved in water is obtained at 605 nm,

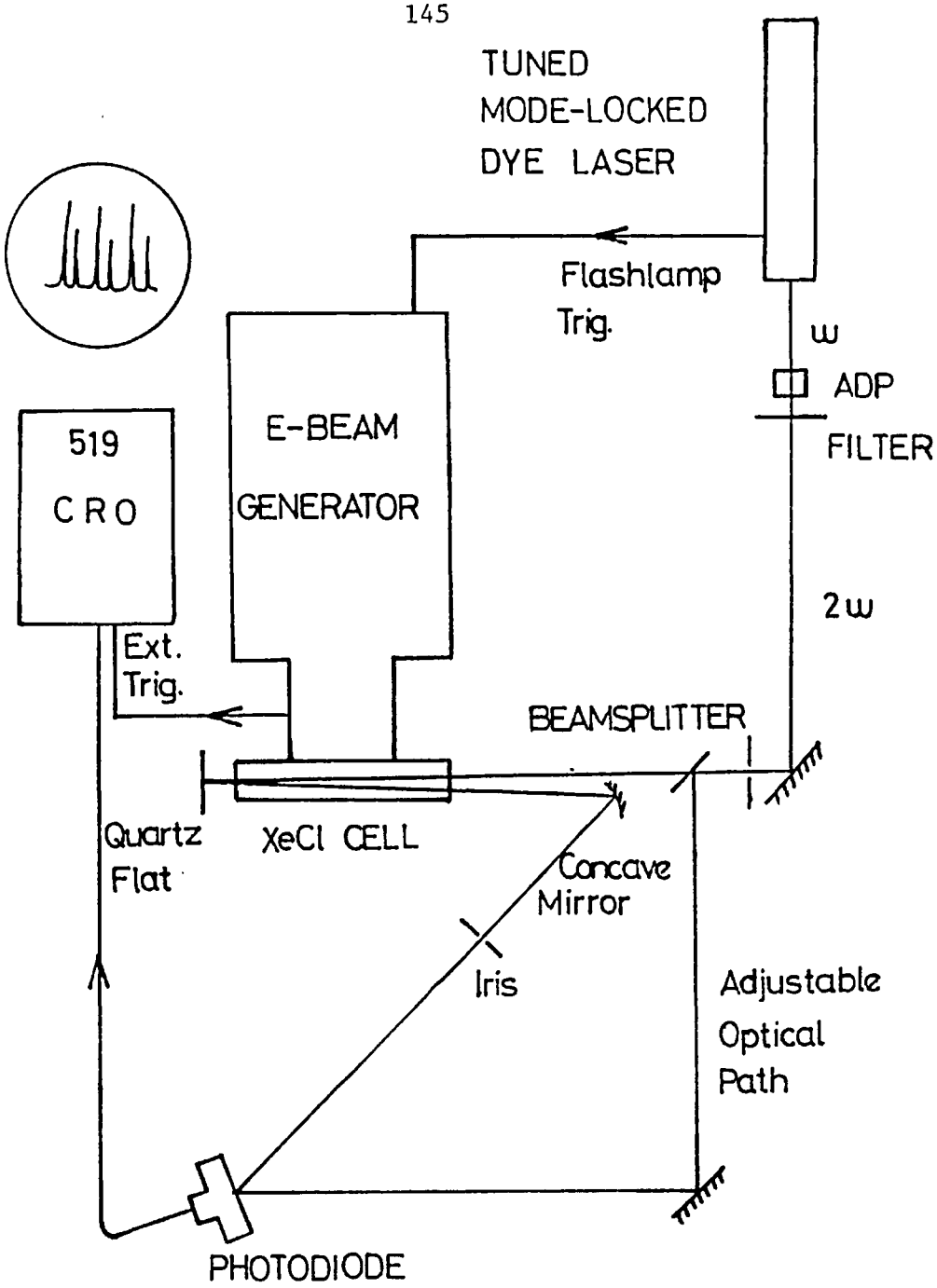


FIGURE 6.4 Schematic of XeCl probe experimental arrangement.

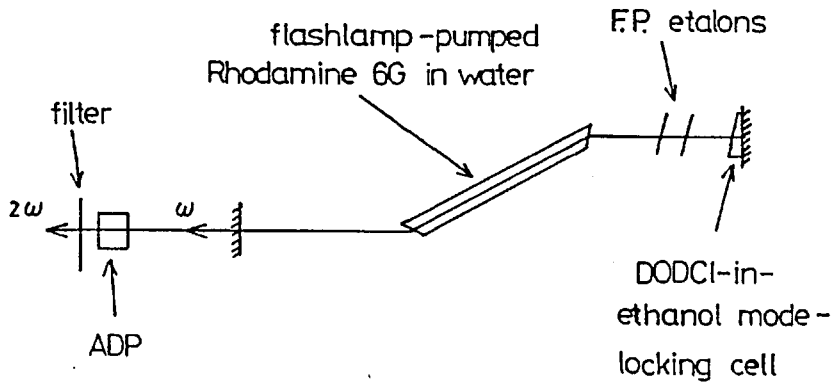


FIGURE 6.5 Schematic of dye laser.

suitable for second harmonic generation of the XeCl wavelength. At the fundamental wavelength, the tuning range was ∿ 30 nm, and typical tuned output energy was 0.5 μJ/pulse. The second harmonic of the fundamental was generated with ∿ 10% efficiency with an angle-tuned ADP crystal 1 cm thick. The ADP crystal temperature was kept constant within ± 0.1°C to prevent the tuned output from drifting in wavelength. After passing through the ADP, a filter removed the fundamental wavelength. Tuned bandwidth (FWHM) of the second harmonic was ∿ 1Å, narrow enough to resolve the different vibronic transitions in XeCl but broad enough to average over all the rotational levels. (Neighbouring v'' transitions are separated by ∿ 2.5 Å.) The second harmonic wavelength was monitored with a Hilger and Watts 0.6 metre Czerny-Turner spectrograph, calibrated with mercury lines from a low pressure lamp. Resolution of the spectrograph was 1.0 Å and reciprocal dispersion near 308 nm was 13.6 Å $mm^{-1}$ in first order. Fig. 6.6(a) shows part of the second harmonic pulse train at 3043 Å (2-1 transition). To prevent double-pulsing, the dye laser was operated close to threshold. Total pulse train width (FWHM) varied between 200 ns and 400 ns. Individual pulse heights varied in a rather irregular manner, due to the sensitivity of second harmonic conversion efficiency to power. The peak intensity of the second harmonic beam was of the order of 10 kW $cm^{-2}$, much less than the saturation intensity of XeCl which is of the order of 1 MW $cm^{-2}$. This ensured that small-signal gain and absorption were measured in the XeCl cell.

The beam was mode-locked to increase the efficiency of second harmonic generation and to improve the signal to noise ratio. Mode-locked pulses are essential for measuring gain during excitation, when the large amplified spontaneous emission signal would swamp a continuous probe signal.

### 6.3.2 XeCl cell and gas mixture

The XeCl cell was the same as that used for the co-axially pumped

FIGURE 6.6 (a) top left - second harmonic pulse train, 20 ns/div.
(b) top right - A.S.E., 20 ns/div.
(c) middle left - double-passed pulse trains, top two show probe shots, bottom trace is a calibration shot, 50 ns/div.
(d) bottom right - single-pass probe shot and calibration shown below it, 20 ns/div.
(e) bottom left - single-pass gain measurement, 20 ns/div.

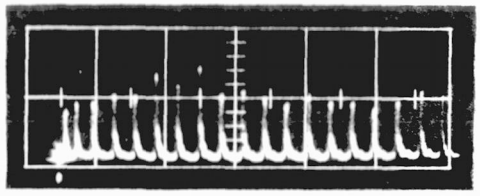

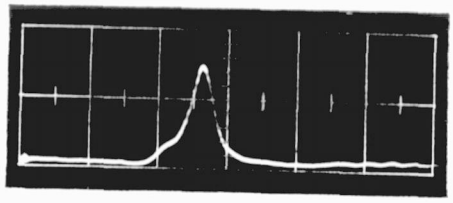

Probe

Probe

Reference

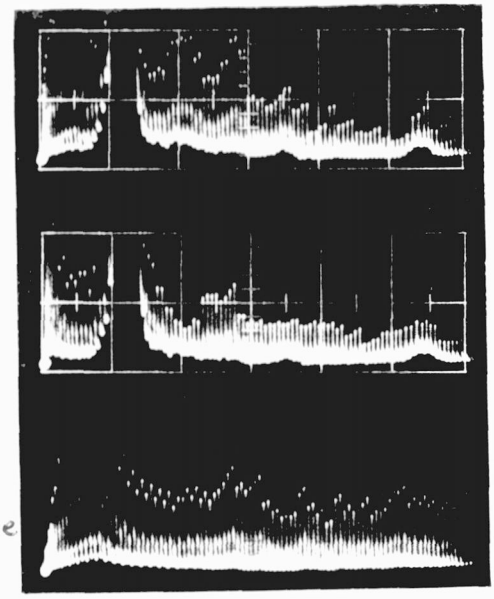

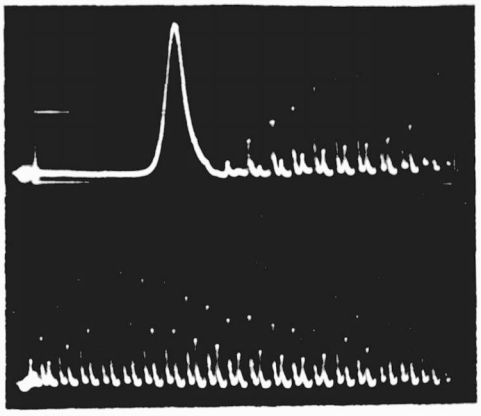

Probe

Reference

Probe

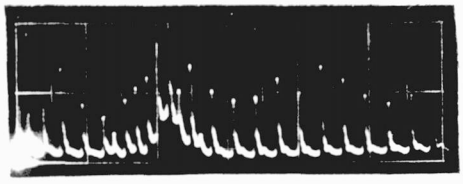

XeCl laser, slightly modified to reduce the amount of amplified spontaneous emission (A.S.E.) generated. To prevent optical feedback into the excited medium, the quartz windows were anti-reflection coated on both sides with a monolayer of magnesium fluoride, and misaligned $2^{o}$ with respect to each other. Despite this, an A.S.E. pulse of duration 6 ns (FWHM) and energy 50 mJ was emitted from both ends of the cell, under typical laser pumping conditions (35 kA, 500 keV) and mixtures (0.2% HCl, 3% Xe, 96.8% Ne) at 5 bar pressure. Fig. 6.6(b) shows a typical A.S.E. pulse, observed on the 0-2 transition only. The large amount of A.S.E. caused some difficulty in data collection, but simplified the interpretation of the results. The peak power of the A.S.E. was 1-2 MW $cm^{-2}$, sufficient to saturate the gain on the 0-1 and 0-2 transitions (see Fig. 5.25), so that the upper state population was rapidly stimulated almost entirely into the $v'' = 1,2$ levels.

Absorption measurements made after A.S.E. and e-beam pumping ceased accurately measured ground state population, because any upper state population was collisionally quenched very rapidly and could be neglected. Using rate constants for collisional quenching of the XeCl(B) state by Ne, Xe and HCl, recently measured by Finn *et al.*[123], the quenching lifetime $\tau_Q$ of the B state is calculated to be 1.7 ns in the gas mixture used in the present work, not taking electron quenching into account. Finn *et al.* found that the rate of electron quenching of the B state at 7 amp $cm^{-2}$ was about 20% of the total quenching rate, compared to an uncertainty of 20% in their measurements. Therefore it is probable that the two orders of magnitude higher current density in the present case would shorten $\tau_Q$ to less than a nanosecond.

### 6.3.3 Synchronization

The e-beam pump pulse (and subsequent reactions in the XeCl gas mixture) were synchronized with the dye laser probe. Triggered independently, the delay time for e-beam and dye laser output was 900 (± 50) ns and

1300 (± 150) ns respectively, where the figure in brackets refers to the jitter. Therefore the dye laser flashlamp signal was used to trigger the e-beam generator, resulting in a total jitter between the two systems of about ± 200 ns. Use of an optical signal to initiate the triggering sequence, detected by a fast photodiode, greatly reduced electrical interference and premature triggering. The flashlamps had a rise time of one microsecond, too slow to trigger the e-beam generator in time to synchronize with the dye laser, and also a source of extra jitter. Therefore the photodiode signal risetime was reduced to 100 ns by use of a simple transistor amplifier, producing a square pulse of amplitude 18 volts. This in turn triggered a TRW Model 46A trigger delay generator which produced a variable delay pulse suitable for direct triggering of the e-beam generator (10 ns risetime, 1 μsec decay time, 300 volt amplitude).

### 6.3.4 Optical paths and signal detection

Fig. 6.4 shows the optical paths taken by the dye laser beam, using a double-pass arrangement in the XeCl cell. The initial beam was divided by a quartz beamsplitter into a probe beam which passed through the XeCl cell, and a reference beam which did not. The probe and reference beams were re-united at a fast photodiode detector. Since each beam is actually a train of picosecond pulses, the photodiode detected two interleaved pulse trains. Fig. 6.6(c) shows oscilloscope pictures taken with such an arrangement, in the presence and absence of e-beam excitation of the XeCl cell. The very large signal is due to A.S.E. The optical delays were arranged so the individual pulses arrived at the photodiode in corresponding probe-reference pairs, i.e. both pulses in a pair derived from the same "pre-beamsplitter" pulse. To prevent interference between the pulses in the detection system, they were spaced equally in time at 3 ns intervals. The time resolution of the photodiode and Tektronix 519 oscilloscope detection system was 1.2 ns. Pulses were easily identified as either "probe" or

"reference" due to the irregularity of pulse heights. This irregularity was the motive for using one photodiode to detect both pulse trains, since optical synchronization allowed the nanosecond accuracy required to distinguish corresponding probe-reference pairs. Electronic synchronization between two different photodiodes, each detecting the "probe" or "reference" beam only, was not accurate enough to positively identify corresponding probe-reference pairs. This would not have mattered if the dye laser output had been uniform.

The probe beam was double-passed through the XeCl cell to improve the accuracy of the absorption measurements. Some single-pass experiments were also performed, mainly to measure the gain on the 0-2 transition during e-beam excitation. Use of a single pass resulted in a reduction of A.S.E. compared to the double-pass arrangement, and a reduction in the fraction of A.S.E. detected. Fig. 6.6(d) is an oscilloscope picture of the photodiode signal during e-beam excitation of a typical gas mixture, using single-pass geometry, and a corresponding calibration shot.

To prevent full laser action when double-pass geometry was used, a parallel quartz flat of low reflectivity (10%) was used as the back reflector. Even so, A.S.E. was very intense and the energy exceeded the 50 mJ measured with no external optics present. To cut down its detection, a spatial filter was used. This consisted of a concave, one metre radius of curvature KrF dielectric full reflector, which provided adequate reflectivity at 308 nm, and a one millimetre diameter aperture placed at the focus of the mirror. The mirror was placed close to the cell, at an angle about $20^{o}$ off the XeCl axis. The high off-axis alignment eliminated any possibility of optical feedback into the cell (see Fig. 6.4). The relatively high quality dye laser beam ($\sim$ 1 mrad beam divergence) was focused without loss through the aperture, whereas most of the poorly focused A.S.E. was blocked by the iris. The concave mirror was apertured to reflect as little

A.S.E. as possible, while still allowing unhindered reflection of the probe beam.

The advantages of a mirror compared to a lens are the absence of stray reflections and ease of alignment using a He-Ne laser. Furthermore, the mirror will act as a diverging element for sources of A.S.E. situated inside the focal length, if the A.S.E. beam divergence is great enough. In practice, the spatial filter was very effective in attenuating the A.S.E. under single-pass conditions (attenuation of order 1000) and less so under double-pass conditions (attenuation of order 100), due to the smaller beam divergence in the latter case. The smaller attenuation and greater absolute amount of A.S.E. in the double-pass case meant that it was not possible to measure gain or loss while A.S.E. was present.

The interleaved pulse trains were detected by a fast ITL UV photodiode which was checked for linearity over the range used, and a Tektronix 519 oscilloscope. The oscilloscope was triggered externally by the signal from the e-beam current monitor. By appropriate adjustments of cable lengths from the external trigger source and the photodiode, taken with knowledge of the optical path lengths, the gain or loss in the cell was measured at known times before and after the beginning of e-beam excitation of the medium. Oscilloscope jitter contributed ± 1 ns to the timing error. The probe pulses were used to mark time in the medium, counted when the pulse was halfway through the active medium in the single-pass case, and when it was at the quartz back reflector in the double-pass case. Consequently, the gain or loss was averaged over a time interval of $\frac{1}{2}$ ns in the single pass case, and over 2 ns in the double pass case, corresponding to the total transit time of the pulse through the medium.

### 6.3.5 Experimental procedure

Before every probe shot, defined as one taken synchronously with e-beam excitation, the system was first calibrated. This was done by

firing the dye laser only and recording the resultant signal on the photodiode. In the absence of e-beam excitation of the medium, the ratio of probe to reference pulse heights, $R_o$, will be a constant which depends on such factors as mirror reflectivities and alignment, filter attenuation, scattering in the laser cell and background absorption. Calibration shots were taken before every probe shot to allow for changing conditions, mainly in the cell (see Fig. 6.6).

In the case of a probe shot, the ratio of probe to reference pulse height, R(t), is a function of time due to the time dependent gain and loss in the excited medium. $R_o$, R(t) and the gain coefficient $\alpha(t)$ are related by the following expression:

$$R(t)/R_o = e^{\alpha(t)\ell} \qquad 6.19$$

$\ell$ = active medium length (15 cm single-pass, 30 cm double-pass)

Each probe shot, together with its calibration, therefore allows calculation of the gain or loss in the medium at 6.2 ns intervals (the time between successive probe pulses). The measurement is independent of the shape of the picosecond pulses, which are far shorter than the time resolution of the detection system.

Due to the rather poor accuracy of each gain measurement (± 1% $cm^{-1}$ double-pass, ± 2% $cm^{-1}$ single-pass) and to increase the density of time sampling, ten or more successful probe shots were taken on each vibronic transition investigated. About one in four shots were successful, due to jitter and variations in dye laser output. An exception to this was the measurement of peak gain on the main laser transition (0-2), where only a few measurements were made. In this case, because of the high amplification of the probe pulses, an optical filter of 65x attenuation at 308 nm was placed in the probe beam path between the XeCl cell and the photodiode, during a probe shot. Attenuation was by glass slides, which do not bleach

at high intensities. Calibration was done in the normal way without the high optical attenuation present. Fig. 6.6(e) shows an oscilloscope trace obtained while measuring the peak gain. Note that the probe pulses are only visible where they have been amplified by the medium.

To return to an earlier point, the low reflectivity quartz flat attenuated the probe beam as well as reducing the A.S.E., but this did not negate the advantage created by use of double-pass geometry. The reason is that the absolute intensity of the probe pulses is of no interest so long as they are conveniently detectable. It is important that the ratio between $R_o$ and R(t) is as large as possible, to minimize the effect of error in each. Since this ratio, as given in equation 6.19, depends exponentially on gain length, it is advantageous to increase the length of active medium traversed by the probe beam.

The transitions studied, chosen because of their large Franck-Condon factors and lack of overlap with other strong transitions[122], were 0-2 (3082 Å), 1-0 (3059 Å), 2-0 (3041 Å), 2-1 (3043 Å), and 2-2 (3046 Å). The rate $k_{Xe}$ was determined by the measurement of $\omega_D$ at xenon concentrations between 1% and 3%, on the 2-0 transition. As stated earlier, the peak gain on the 0-2 transition was measured using single-pass geometry. Absorption in a pure Ne-Xe mixture was also ~~looked at.~~ investigated.

## 6.4 Results

Figs. 6.7, 6.8(a) and 6.9(a) are plots of gain or loss versus time in e-beam-excited mixtures of Ne, Xe, HCl (96.8%, 3%, 0.2%) at 5 bar total pressure, observed on the 0-2, 1-0, and 2-1 transitions respectively. The origin of the time axis corresponds to the beginning of the e-beam pump pulse. The data are plotted at 5 ns intervals, and each point is the mean of roughly ten raw data measurements within the 5 ns time slot.

The 1-0 results, for example (Fig. 6.8), show an initial rapid rise

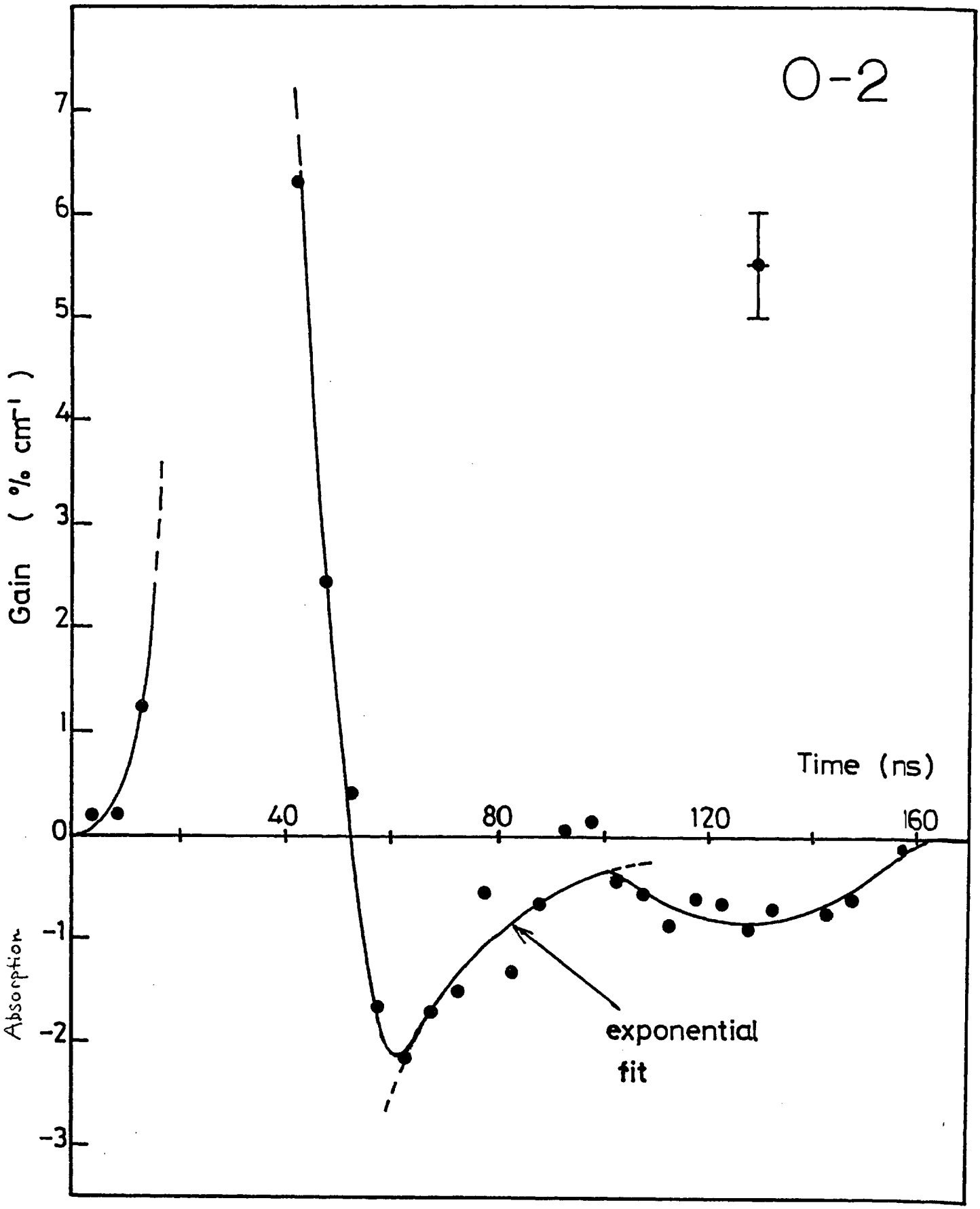


FIGURE 6.7 Gain and loss on 0-2 transition.

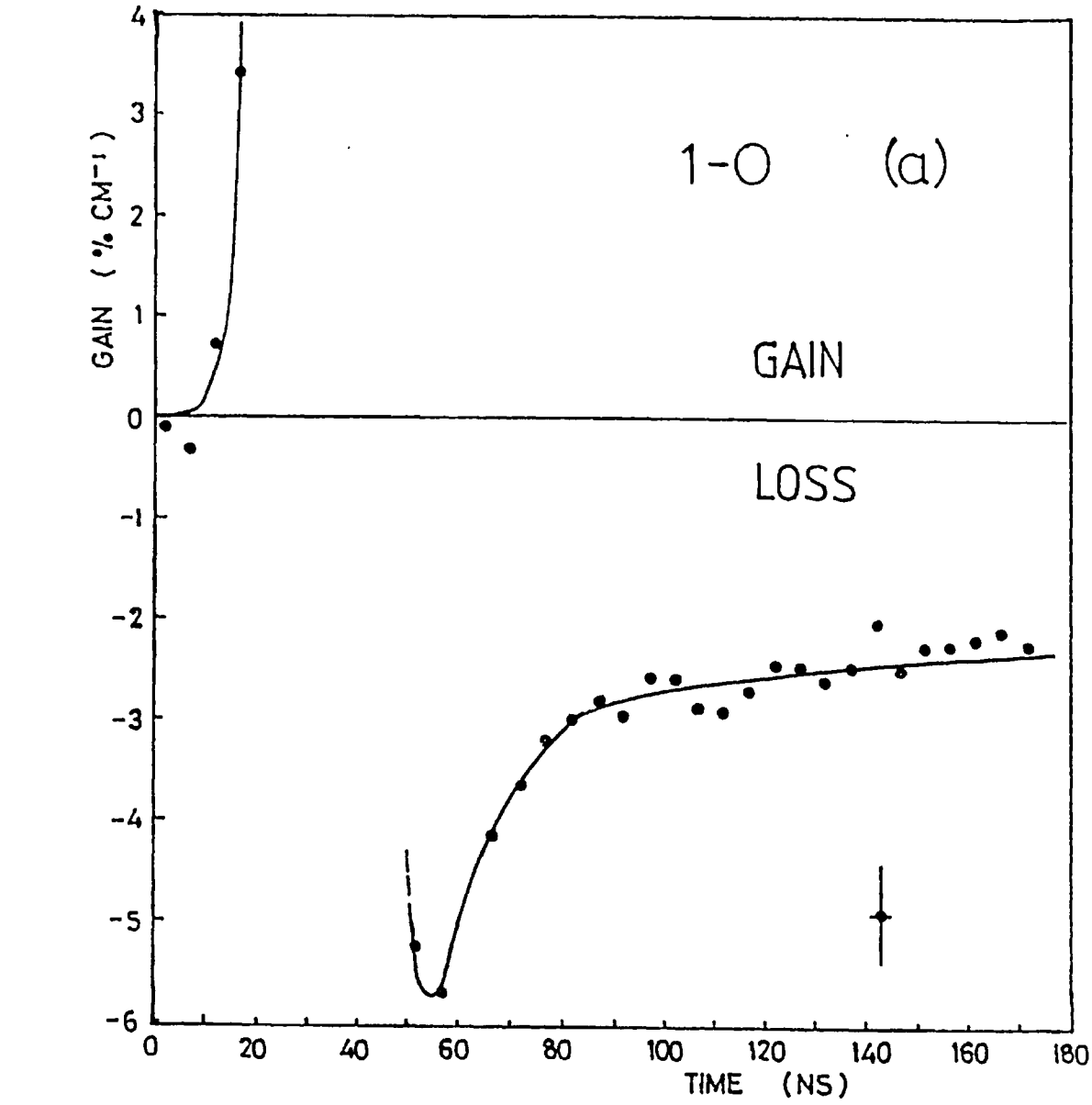


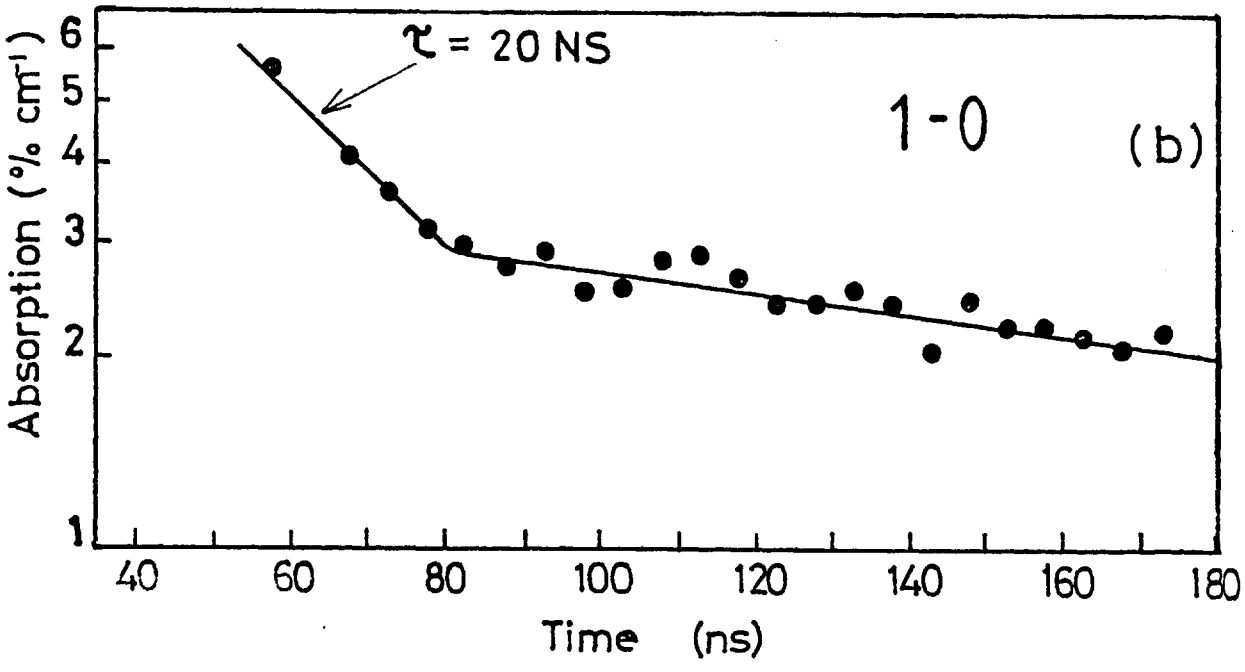


FIGURE 6.8 Gain and loss on 1-0 transition.

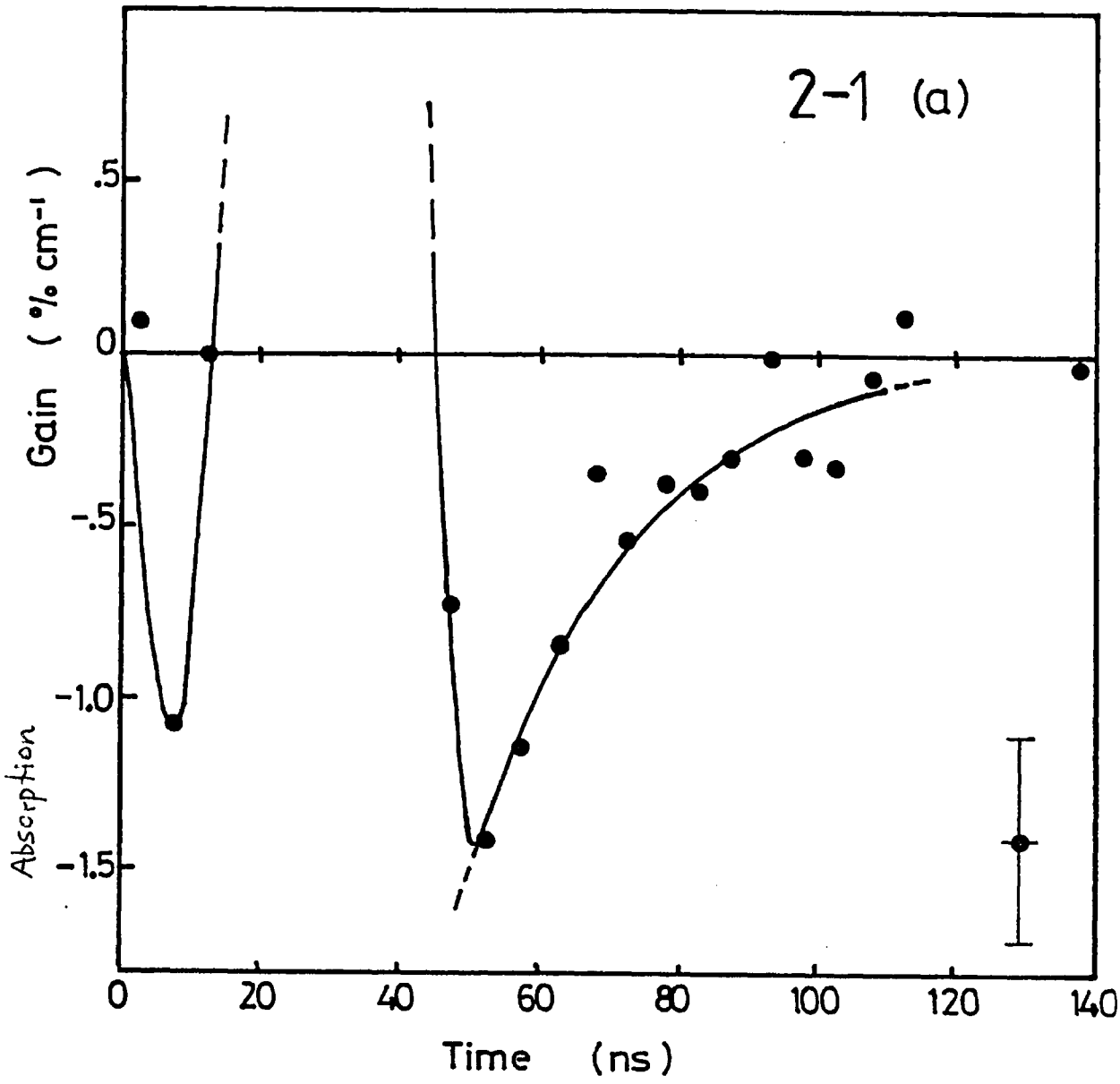


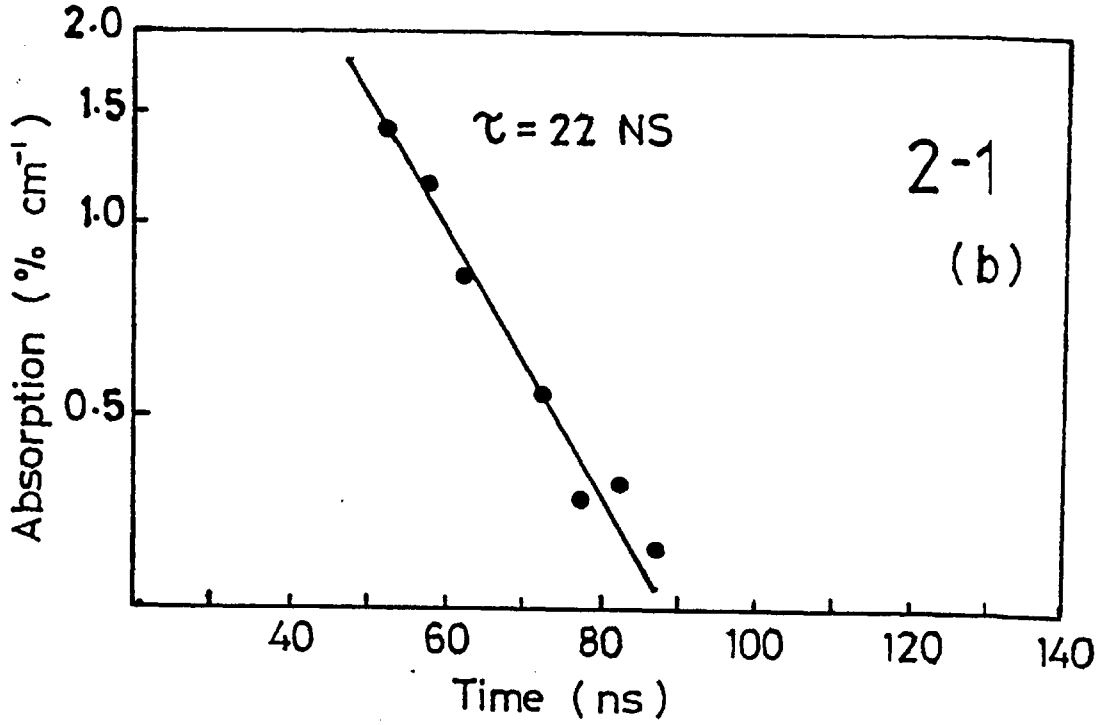


FIGURE 6.9 Absorption on 2-1 transition.

in gain followed by an absorption decay tail 55 ns from the origin (total e-beam pulse duration = 45 ns). The gap in the data is due to A.S.E. Similar results were obtained on the 0-2 and 2-1 transitions (Figs. 6.7 and 6.9), although there is not the same initial rise in gain on the 2-1 transition. The curves through the absorption decay region are least squares exponential fits to the data. Figs. 6.8(b) and 6.9(b) show the absorption on the 1-0 and 2-1 transitions semi-logarithmically.

The initial rapid decay of absorption after e-beam pumping ceases is due to ground state dissociation of XeCl. When pure Ne-Xe mixtures (97%, 3%, 5 bar total pressure) were probed at 3047 Å, no fast decay of absorption was observed after e-beam pumping ceased. Fig. 6.10 is a plot of the observed absorption in such a mixture, and a least squares fit indicates one decay lifetime of 220 (± 20) ns. Only the addition of HCl to the mixture, and consequent presence of XeCl(X), led to the rapid variations in gain and absorption observed. Further evidence that XeCl ground state decay was being observed was provided by the fact that the measured absorption decreased if the probe beam wavelength moved off resonance, i.e. absorption was not broadband.

Table 6.1 summarises the results obtained for ground state dissociation times on the different transitions. The errors are partly due to uncertainty in the beginning and end points of true exponential decay, and to background absorption which had a characteristic decay time of the order of hundreds of nanoseconds.

If vibrational relaxation is fast compared to ground state dissociation, the ground state levels decay with the same lifetime, as predicted in Section 6.2, and are populated according to the Boltzmann distribution. Within the accuracy of the experiment, there is no difference or trend in lifetimes. The large population in $v'' = 0$ is strong evidence that vibrational relaxation is sufficiently fast to equilibrate the ground state

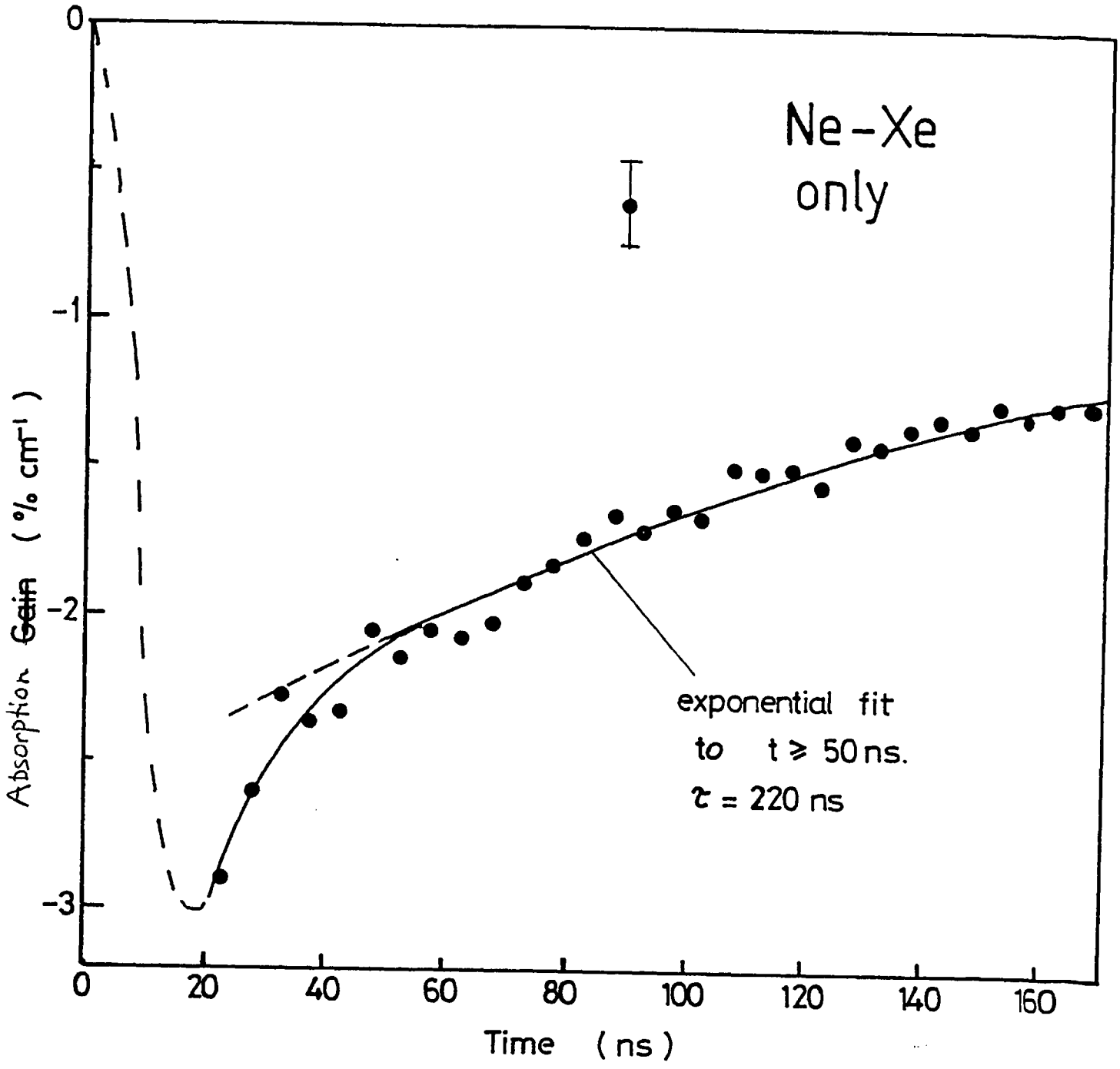


FIGURE 6.10 Absorption in Ne-Xe mixture.

TABLE 6.1 Decay times of XeCl ground state levels

| Transition (v' - v") | Initial Gain | Decay Time (ns) |
|---|---|---|
| 0-2 | Yes | 21 ± 9 |
| 1-0 | Yes | 20 ± 4 |
| 2-0 | No | ( 25 ± 7<br>(<br>( 11 ± 7 |
| 2-1 | No | 22 ± 6 |
| 2-2 | No | 15 ± 6 |
| | | Mean = 19 ± 3 |
| Ne-Xe only | No | 220 ± 20 |

manifold, since all the population is fed into v'' = 1,2 (and to a smaller degree v'' = 3) levels. On the assumption that the true lifetime, $\omega_D^{-1}$, is the same for each level, the results in Table 6.1 indicate

$$\omega_D^{-1} = 19(\pm 3) \text{ ns}$$

under typical XeCl laser conditions. The upper state manifold is also in thermal quasi-equilibrium before stimulated emission builds up, since high gain is observed on transitions originating from v' = 0,1 but not from v' = 2, despite comparable Franck-Condon factors. The upper state vibrational spacing is 195 $cm^{-1}$ [37], which implies relative room temperature thermal equilibrium populations of 1 : 0.38 : 0.15 in v' = 0,1 and 2 respectively.

Fig. 6.11 is a plot of $\omega_D$ versus xenon concentration [Xe], on the 2-0 transition. The collisional dissociation rate with xenon, $k_{Xe}$, given by the slope of a least squares straight line fit to the measured points, is

$$k_{Xe} = 4(\pm 3) \times 10^{-12} \text{ cm}^3 \text{ s}^{-1}$$

This value, and the value for $\omega_D = 5.3(\pm 0.8) \times 10^7 \text{ s}^{-1}$, are in reasonable agreement with respective values $k_{Xe} = 5.6(\pm 0.8) \times 10^{-12} \text{ cm}^3 \text{ s}^{-1}$ and $\omega_D = 3.9(\pm 0.4) \times 10^7 \text{ s}^{-1}$ measured by Waynant and Eden[119].

Fig. 6.12 shows single-pass peak gain measurements made in a 93.8% Ne, 6% Xe, 0.2% HCl mixture at 5.0 bar, on the main lasing transition 0-2. The lower part of the gain curve is a fit to measurements made in a separate double-pass experiment using the same gas mixture. The peak gain of 0.28 $cm^{-1}$ corresponds to a single pass amplification of 67. The e-beam power is plotted on the same time-scale, showing how the gain follows the pump pulse with a delay of $\sim$ 5 ns.

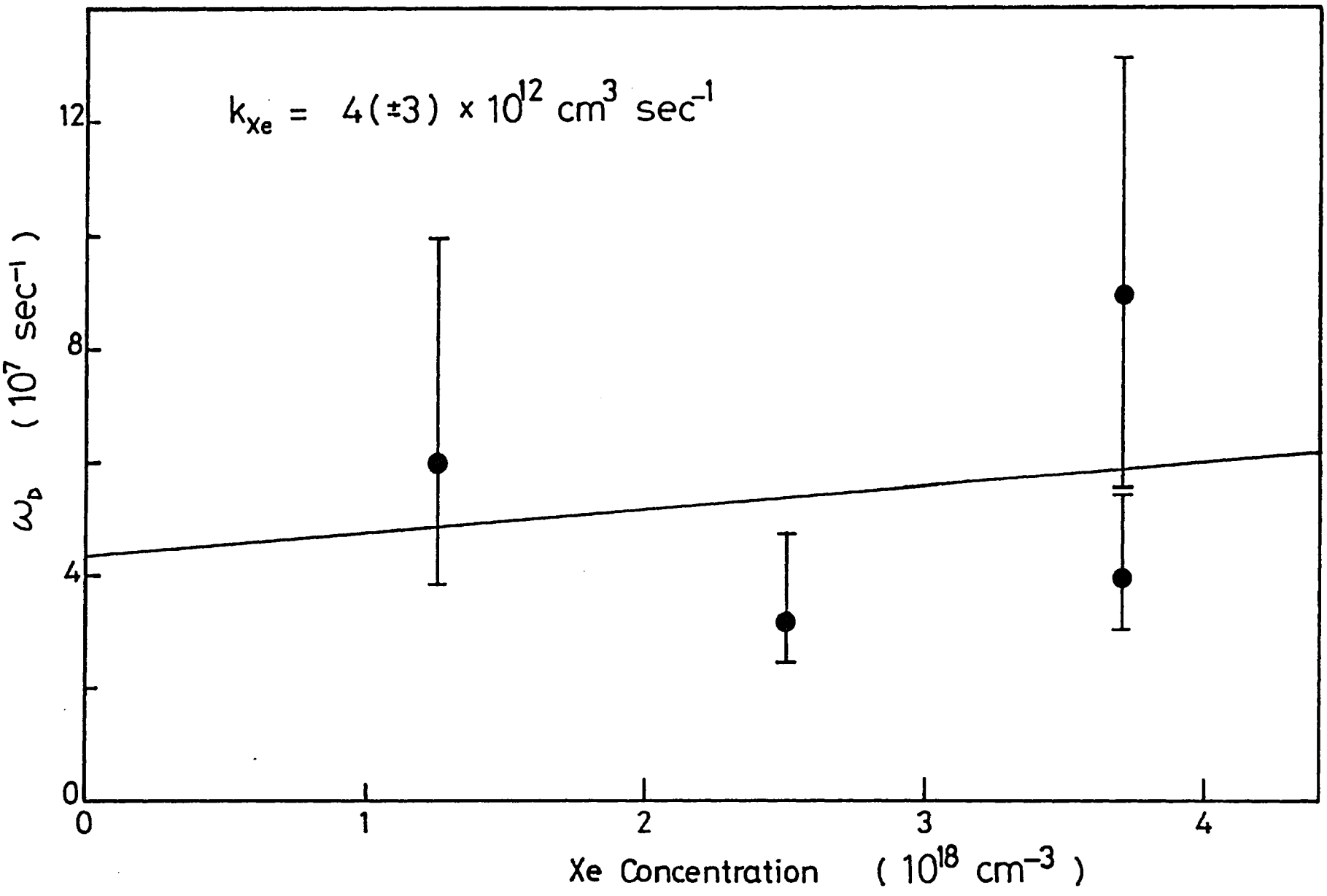


FIGURE 6.11 $\omega_D$ versus Xe concentration, 2-0 transition.

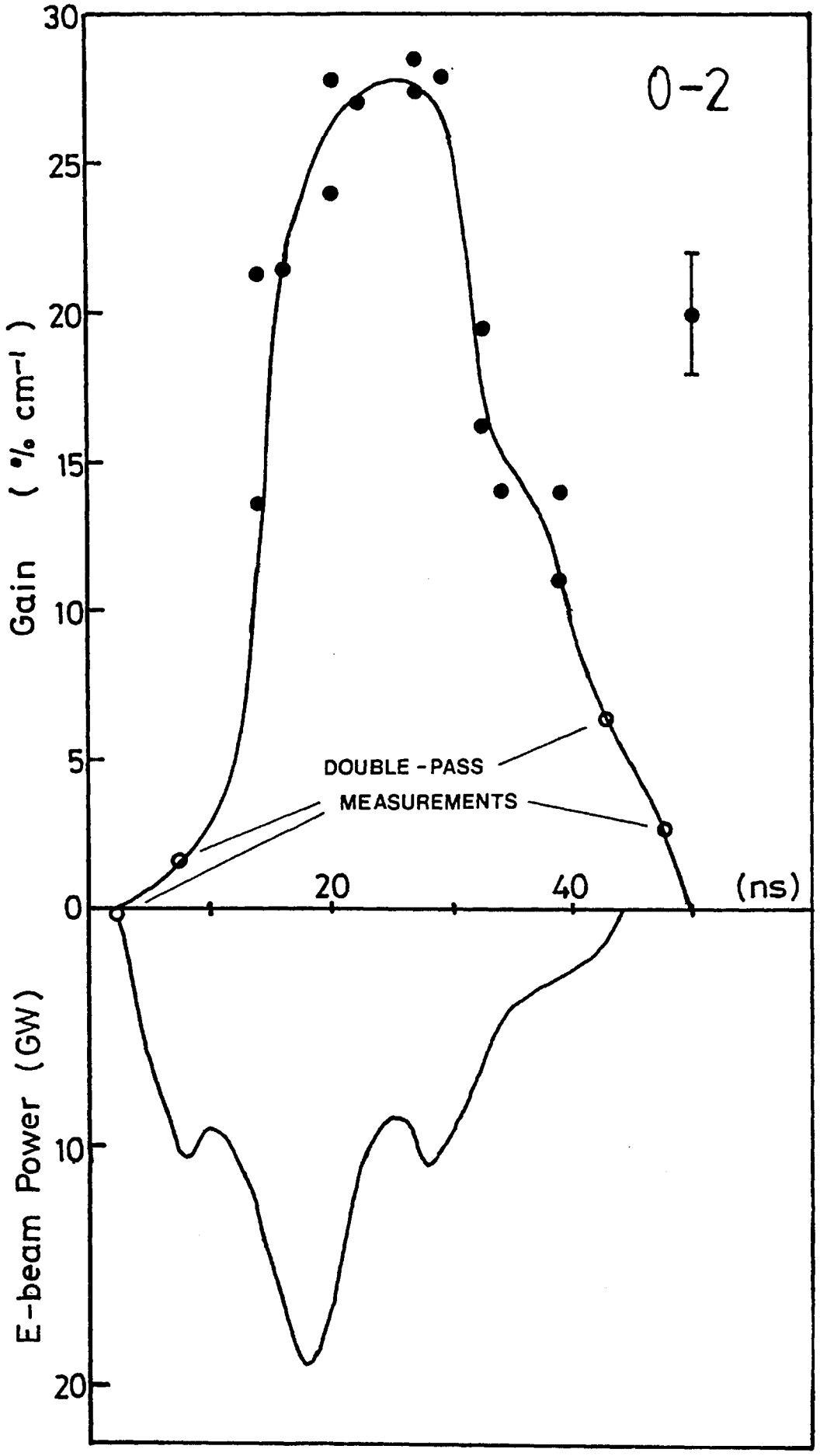


FIGURE 6.12 Peak gain on O-2 laser transition.

## 6.5 Conclusion

We have shown that the ground state of XeCl has a dissociation time longer than the spontaneous decay time $\omega_{32}^{-1}$ of 11 ns[36], under typical laser conditions. Despite this, continuous laser operation is possible, as shown by the simple analysis of steady-state conditions in Section 6.2. Fig. 6.13 is a plot of $\beta$ against $\omega_{21}$ (see inequality 6.16), where $\beta$ is calculated using the value of $\omega_D$ measured in the present work. This shows that condition 6.16 is satisfied down to a vibrational relaxation rate $\omega_{21}$ as low as $4.5 \times 10^7$ $s^{-1}$, corresponding to a vibrational relaxation time of 22 ns. This is an order of magnitude or more slower than the actual rate, so that $\beta$ is a factor of 2-3 greater than $\omega_{32}$ in the present case. In the same way as has been demonstrated with XeF[114,117,118,125], laser efficiency should be increased by operating the gas mixture at higher temperatures, so as to increase $\omega_D$ and $\omega_{21}$.

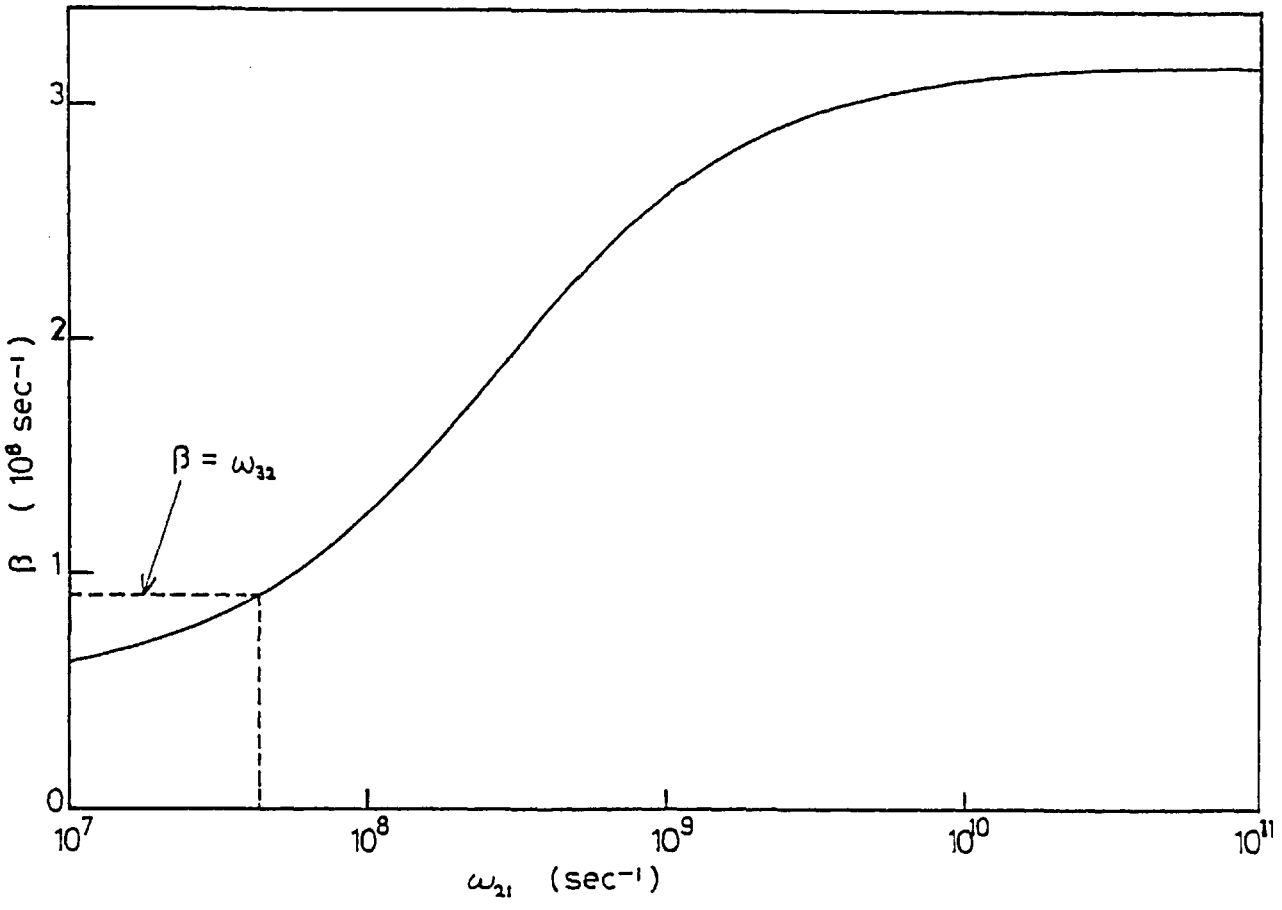


FIGURE 6.13 $\beta$ versus $\omega_{21}$.

CHAPTER 7

# CONCLUSION

It has been shown that short pulse (10-20 ns) e-beam-pumped KrF and XeCl lasers can be operated with $\sim$ 2% intrinsic efficiency at an excitation rate of 15-30 MW $cm^{-3}$, and using a co-axial pumping scheme, specific laser energy densities of 17 and 8 J $litre^{-1}$ were attained in KrF and XeCl, respectively. From the discussion of quenching losses in Chapter 3, it is clear that collisional quenching of the upper laser level during the laser build-uptime significantly reduces the intrinsic efficiency, and if this time could be reduced there would be a corresponding increase in efficiency. This has been demonstrated by Edwards *et al.*[112], who injected a 1 MW $cm^{-2}$, 20 ns KrF laser pulse into an e-beam-pumped 10 MW $cm^{-2}$ laser cavity at the beginning of the e-beam pump pulse, increasing the e-beam-pumped laser pulse duration from 37 ns to the full 60 ns (FWHM) duration of the pump pulse, with a resultant increase in the efficiency. The implication is that in a high power, short pulse system consisting of a master oscillator and a chain of amplifiers (such as would be used for laser fusion studies), the low intrinsic efficiency of the master oscillator is not of primary importance, since the efficiency of the amplifiers would not be limited by any build-up time to oscillation, and pulses as short as 10 ns could be employed. This would simplify the optical pulse-compression scheme required to shorten the pulse further to < 1 ns.

The effect of the very high excitation rates in the present work is to increase the rate of electron quenching of the upper laser level and hence reduce the peak power efficiency as well as the intrinsic

efficiency, compared to lower excitation rates[112,113]. However, Tisone *et al.*[113] achieved intrinsic efficiencies of 11% in KrF pumped at 7 MW $cm^{-3}$, with a laser output power of 30 MW $cm^{-2}$, and similar efficiency at the higher excitation rates of the present work may be possible if the laser intensity were greater than the 26 MW $cm^{-2}$ maximum attained here in KrF, thus allowing stimulated emission to dominate collisional quenching. However, the reason for the improved efficiency at the excitation rates employed by Tisone compared to previous work[11,126,127] at similar excitation rates is not completely clear, and the effects of high excitation rates on all aspects of rare gas halide kinetics require further study.

The rationale for using high pump rates is the resultant reduction in total laser or amplifier volume. The radial return diode has been demonstrated to be a simple means of practically realizing a compact high power system, whose performance improves with increasing e-beam current, instead of leading to catastrophic beam pinch such as would be experienced in an axial return co-axial diode of similar dimensions. The problems encountered here with anode tube buckling could be overcome by using an Hibachi to support the thin foil anode.

The ground state dissociation time in XeCl is an important parameter, and its measurement is useful in improving our understanding of the kinetics of the XeCl laser. A thorough understanding of the kinetics will require extensive computer modelling, considering all significant reactions using the best available rate constants (as has been done for KrF) and consideration of a multi-level ground state. The simple two level model of the ground state used here is sufficient to explain the observed population decay in XeCl, as well as the steady-state lasing observed[128] in the bound ground state rare gas halides.

REFERENCES

1. Stevens, B., Hutton, E. (1960). Nature 186, 1045.

2. Houtermans, F.G. (1960). Helv. Phys. Acta 33, 933.

3. Basov, N.G., Danilychev, V.A., Popov, Y.M. (1971). Soviet J. Quant. Elect. 1, 18.

4. Koehler, H.A., Ferderber, L.J., Redhead, D.L., Ebert, P.J. (1972). Appl. Phys. Lett. 21, 198.

5. Hoff, P.W., Swingle, J.C., Rhodes, C.K. (1973). Appl. Phys. Lett. 23, 245.

6. Hughes, W.M., Shannon, J., Hunter, R. (1974). Appl. Phys. Lett. 24, 488.

7. Golde, M.F., Thrush, B.A. (1974). Chem. Phys. Lett. 29, 486.

8. Velazco, J.E., Setser, D.W. (1975). J. Chem. Phys. 62, 1990.

9. Searles, S.K., Hart, G.A. (1975). Appl. Phys. Lett. 27, 243.

10. Brau, C.A., Ewing, J.J. (1975). Appl. Phys. Lett. 27, 435.

11. Ewing, J.J., Brau, C.A. (1975). Appl. Phys. Lett. 27, 350.

12. Hoffman, J.M., Hays, A.K., Tisone, G.C. (1976). Appl. Phys. Lett. 28, 538.

13. Murray, J.R., Powell, H.T. (1976). Appl. Phys. Lett. 29, 252.

14. Waynant, R.W. (1977). Appl. Phys. Lett. 30, 234.

15. Rice, J. 7th Winter Colloquium on High Power Visible Lasers, Park City, Utah, 1977. (Unpublished)

16. Waynant, R.W. (1978). Soviet J. Quant. Elect. 8, 1002.

17. Ewing, J.J., Brau, C.A. (1975). Phys. Rev. A12, 129.

18. Hunter, R. 7th Winter Colloquium on High Power Visible Lasers, Park City, Utah, 1977. (Unpublished)

19. Bhaumik, M.L., Bradford Jr., R.S., Ault, E.R. (1976). Appl. Phys. Lett. 28, 23.

20. Berger, M.J., Seltzer, S.M. (1964). Tables of energy-losses and ranges of electrons and positions. NAS-NRC Publication 1133, p 205.

21. Daugherty, J.D. (1976). In: Principles of Laser Plasmas (Ed. G. Bekefi). Wiley : New York, London, Sydney, Toronto.

22. Rothe, D.E., West, J.B., Bhaumik, M.L. (1979). IEEE J. Quant. Electron. QE-15, 314.

23. Platzman, R.L. (1961). Int. J. Appl. Rad. Isotopes 10, 116.

24. Peterson, L.R., Allen, J.E. (1972). J. Chem. Phys. 56, 6068.

25. Bugaev, S.P., Mesyats, G.A., Proskurovskii, D.I. (1969). Sov. Phys. - Dokl. 14, 605.

26. Slade, P.D. (1979). PhD thesis, Imperial College, University of London.

27. Bradley, L.P. (1976). In: High Power Gas Lasers (Ed. E.R. Pike). Inst. Phys. Conf. Series No.29 : Bristol and London.

28. Bradley, D.J., Hull, D.R., Hutchinson, M.H.R., McGeogh, M.W. (1974). Opt. Commun. 11. 335.

29. Ramirez, J.J., Prestwich, K.R. (1979). J. Appl. Phys. 50, 4988.

30. Langmuir, I., Compton, K.T. (1931). Rev. Mod. Phys. 3, 191.

31. Schlitt, L.G., Bradley, L.P. (1975). Lawrence Livermore Laboratory Report UCRL-77203.

32. Hutchinson, M.H.R., Bradley, D.J. U.K. Patent Application No.16769/78.

33. Hutchinson, M.H.R., Levy, C.D.P., Reksten, R.M. In: Proc. 4th. Nat. Quant. Electron. Conf., Edinburgh, Sept. 1979. Wiley (to be published)

34. Glasoe, G.N., Lebacqz, J.V. (1948). Pulse Generators. M.I.T., Cambridge, Mass.

35. Brau, C.A., Ewing, J.J. (1975). J. Chem. Phys. 63, 4640.

36. Hay, P.J., Dunning Jr., T.H. (1978). J. Chem. Phys. 69, 2209.

37. Sur, A., Hui, A.K., Tellinghuisen, J. (1979). J. Mol. Spectrosc. 74. 465.

38. Tellinghuisen, P.C., Tellinghuisen, J., Coxon, J.A., Velazco, J.E., Setser, D.W. (1978). J. Chem. Phys. 68, 5187.

39. Kligler, D., Nakano, H.H., Huestis, D.L., Bischel, W.K., Hill, R.M., Rhodes, C.K. (1978). Appl. Phys. Lett. 33, 39.

40. Brashears Jr., H.C., Setser, D.W. (1978). Appl. Phys. Lett. 33, 821.

41. Rokni, M., Jacob, J.H., Mangano, J.A. (1977). Phys. Rev. A16, 2216.

42. Rokni, M., Mangano, J.A., Jacob, J.H., Hsia, J.C. (1978). IEEE J. Quant. Electron. QE-14, 464.

43. Velazco, J.E., Kolts, J.H., Setser, D.W. (1976). J. Chem. Phys. 65, 3468.

44. Hill, R.M., Trevor, P.L., Huestis, D.L., Lorents, D.C. (1979). Appl. Phys. Lett. 34, 137.

45. Bischel, W.K., Nakano, H.H., Eckstrom, D.J., Hill, R.M., Huestis, D.L., Lorents, D.C. (1979). Appl. Phys. Lett. 34, 565.

46. Ernst, W.E., Tittel, F.K. (1979). Appl. Phys. Lett. 35, 36.

47. Yariv, A. (1976). Introduction to Optical Electronics. Holt, Rinehart & Winston.

48. Lorents, D.C., Huestis, D.L., McCusker, M.V., Nakano, H.H., Hill, R.M. (1978). J. Chem. Phys. 68, 4657.

49. Tang, K.Y., Lorents, D.C., Huestis, D.L. (1980). Appl. Phys. Lett. 36, 347.

50. Tittel, F.K., Wilson, W.L., Stickel, R.E. (1980). Appl. Phys. Lett. 36, 405.

51. Gundel, L.A., Setser, D.W., Clyne, M.A.A., Coxon, J.A., Nip, W. (1976). J. Chem. Phys. 64, 4390.

52. Shaw, M.J. (1979). Prog. Quant. Electron. 6, 3.

53. Ewing, J.J., Brau, C.A. (1976). In: Tunable Lasers and Applications (Ed. A. Mooradian, J. Jaeger, P. Stokseth). Springer Series in Optical Sciences 3. Springer-Verlag : Berlin, Heidelberg, New York.

54. Judd, O.P. (1976). J. Appl. Phys. 47, 5297.

55. Flannery, M.R., Yang, T.P. (1978). Appl. Phys. Lett. 32, 327.

56. Flannery, M.R., Yang, T.P. (1978). Appl. Phys. Lett. 32, 356.

57. Flannery, M.R., Yang, T.P. (1978). Appl. Phys. Lett. 33, 574.

58. Brau, C.A. (1979). In: Excimer Lasers (Ed. C.K. Rhodes). Springer-Verlag : Berlin, Heidelberg, New York.

59. Chen, H.L., Center, R.E., Trainor, D.W., Fyfe, W.I. (1977). Appl. Phys. Lett. 30, 99.

60. Schneider, B.I., Brau, C.A. (1978). Appl. Phys. Lett. 33, 569.

61. Nygaard, K.J., Hunter, S.R., Fletcher, J., Foltyn, S.R. (1978). Appl. Phys. Lett. 32, 351.

62. Trainor, D.W., Jacob, J.H. (1979). Appl. Phys. Lett. 35, 920.

63. Nygaard, K.J., Brooks, H.L., Hunter, S.R. (1979). IEEE J. Quant. Electron. QE-15, 1216.

64. Rokni, M., Jacob, J.H., Mangano, J.A. (1979). Appl. Phys. Lett. 34, 187.

65. Liu, W.-C.F., Conway, D.C. (1975). J. Chem. Phys. 62, 3070.

66. Rokni, M., Jacob, J.H., Mangano, J.A., Brochu, R. (1977). Appl. Phys. Lett. 31, 79.

67. Bohme, D.K., Adams, N.G., Mosesman, M., Dunkin, D.B., Ferguson, E.E. (1970). J. Chem. Phys. 52, 5094.

68. Bardsley, J.N., Biondi, M.A. (1970). Adv. At. Mol. Phys. 6, 2.

69. Gedanken, A., Jortner, J., Ray, B., Szoke, A. (1972). J. Chem. Phys. 57, 3456.

70. Quigley, G.P., Hughes, W.M. (1978). Appl. Phys. Lett. 32, 649.

71. Mangano, J.A., Jacob, J.H., Rokni, M., Hawryluk, A. (1977). Appl. Phys. Lett. 31, 26.

72. Tellinghuisen, J., Hays, A.K., Hoffman, J.M., Tisone, G.C. (1976). J. Chem. Phys. 65, 4473.

73. Pummer, H., Hohla, K., Rebentrost, F. (1979). Appl. Phys. 20, 129.

74. Jacob, J.H., Hsia, J.C., Mangano, J.A., Rokni, M. (1979). J. Appl. Phys. 50, 5130.

75. Goldhar, J., Dickie, J., Bradley, L.P., Pleasance, L.D. (1977). Appl. Phys. Lett. 31, 677.

76. Rigrod, W.W. (1965). J. Appl. Phys. 36, 2487.

77. Steunenberg, R.K., Vogel, R.C. (1956). J. Am. Chem. Soc. 78, 901.

78. Wadt, W.R., Cartwright, D.C., Cohen, J.S. (1977). Appl. Phys. Lett. 31, 672.

79. Stevens, W.J., Gardner, M., Karo, A. (1977). J. Chem. Phys. 67, 2860.

80. Mandl, A. (1971). Phys. Rev. A3, 251.

81. Hyman, H.A. (1977). Appl. Phys. Lett. 31, 14.

82. Hawryluk, A.M., Mangano, J.A., Jacob, J.H. (1977). Appl. Phys. Lett. 31, 164.

83. Seery, D.J., Britton, D. (1964). J. Chem. Phys. 68, 2263.

84. Champagne, L.F. (1978). Appl. Phys. Lett. 33, 523.

85. Rokni, M., Jacob, J.H., Mangano, J.A. (1978). Appl. Phys. Lett. 32, 622.

86. Shaw, M.J., Jones, J.D.C. (1977). Appl. Phys. 14, 393.

87. Golde, M.F. (1975). J. Mol. Spectrosc. 58, 261.

88. Burnham, R., Harris, N.W. (1977). J. Chem. Phys. 66, 2742.

89. Poliakoff, E.D., Southworth, S.H., White, M.G., Thornton, G., Rosenberg, R.A., Shirley, D.A. (1980). J. Chem. Phys. 72, 1786.

90. Burnham, R., Searles, S.K. (1977). J. Chem. Phys. 67, 5967.

91. Quigley, G.P., Hughes, W.M. (1978). Appl. Phys. Lett. 32, 627.

92. Eden, J.G., Waynant, R.W., Searles, S.K., Burnham, R. (1978). Appl. Phys. Lett. 32, 733.

93. Wadt, W.R., Hay, P.J. (1978). J. Chem. Phys. 68, 3850.

94. Wadt, W.R., Hay, P.J. (1977). Appl. Phys. Lett. 30, 573.

95. Waynant, R.W., Eden, J.G. (1979). IEEE J. Quant. Electron. QE-15, 61.

96. Rokni, M., Jacob, J.H., Mangano, J.A., Brochu, R. (1977). Appl. Phys. Lett. 30, 458.

97. Kudryavtsev, Y.A., Kuzmina, N.P. (1977). Appl. Phys. 13, 107.

98. Dunning Jr., T.H., Hay, P.J. (1976). Appl. Phys. Lett. 28, 649.

99. Chen, C.H., Payne, M.G. (1978). Appl. Phys. Lett. 32, 358.

100. Shui, V.H. (1977). Appl. Phys. Lett. 31, 50.

101. Sala, K. (private communication)

102. Jacob, J.H. (1974). J. Appl. Phys. 45, 467.

103. Edwards, C.B., Hutchinson, M.H.R., Bradley, D.J., Hutchinson, M.D. (1979). Rev. Sci. Instrum. 50, 1201.

104. Bradley, D.J., Hull, D.R., Hutchinson, M.H.R., McGeoch, M.W. (1975). Opt. Commun. 14, 1.

105. Jones, M.R.O. (private communication)

106. Heath, D.F., Sacher, P.A. (1966). Appl. Opt. 5, 937.

107. Gower, M.C., Kearsley, A.J., Webb, C.E. (1980). IEEE J. Quant. Electron. QE-16, 231.

108. Champagne, L.F. (1978). Appl. Phys. Lett. 33, 523.

109. Losev, V.F., Tarasenko, V.F., Bychkov, Y.I. (1979). Sov. J. Quant. Electron. 9, 918.

110. Oomen, G.L. (1978). Appl. Phys. Lett. 33, 878.

111. Nighan, W.L., Brown, R.T. (1980). Appl. Phys. Lett. 36, 498.

112. Edwards, C.B., O'Neill, F., Shaw, M.J. (To be published in Appl. Phys. Lett.)

113. Tisone, G.C., Patterson, E.L., Rice, J.K. (1979). Appl. Phys. Lett. 35, 437.

114. Rokni, M., Jacob, J.H., Hsia, J.C., Trainor, D.W. (1980). Appl. Phys. Lett. 36, 243.

115. Fulgham, S.F., Herman, I.P., Feld, M.S., Javan, A. (1978). Appl. Phys. Lett. 33, 926.

116. Fulgham, S.F., Feld, M.S., Javan, A. (1979). Appl. Phys. Lett. 35, 247.

117. Hsia, J.C., Mangano, J.A., Jacob, J.H., Rokni, M. (1979). Appl. Phys. Lett. 34, 208.

118. Ernst, W.E., Tittel, F.K. (1980). J. Appl. Phys. 51, 2432.

119. Waynant, R.W., Eden, J.G. (1980). Appl. Phys. Lett. 36, 262.

120. Oomen, G.L., Witteman, W.J. (1980). Opt. Commun. 32, 461.

121. Hemmati, H., Collins, G.J. (1980). J. Appl. Phys. 51, 2961.

122. Tellinghuisen, J., Hoffman, J.M., Tisone, G.C., Hays, A.K. (1976). J. Chem. Phys. 64, 2484.

123. Finn, T.G., Chang, R.S.F., Palumbo, L.J., Champagne, L.F. (1980). Appl. Phys. Lett. 36, 789.

124. Johnson, T.H., Hunter II, A.M. (1980). J. Appl. Phys. 51, 2406.

125. Finn, T.G., Palumbo, L.J., Champagne, L.F. (1978). Appl. Phys. Lett. 33, 148.

126. Tisone, G.C., Hays, A.K., Hoffman, J.M. (1975). Opt. Commun. 15, 188.

127. Tisone, G.C., Hays, A.K., Hoffman, J.M. (1976). Opt. Commun. 18, 117.

128. Champagne, L.F. (1977). Appl. Phys. Lett. 30, 160.